NUREG/CR-2437 Vol. IV
ANL-81-77 Vol. IV

NUREG/CR-2437 Vol. IV
ANL-81-77 Vol. IV

MATERIALS SCIENCE DIVISION LIGHT-WATER-REACTOR SAFETY RESEARCH PROGRAM: QUARTERLY PROGRESS REPORT

October—December 1981

ARGONNE NATIONAL LABORATORY, ARGONNE, ILLINOIS

Prepared for the Office of Nuclear Regulatory Research
U. S. NUCLEAR REGULATORY COMMISSION
under Interagency Agreement DOE 40-550-75

The facilities of Argonne National Laboratory are owned by the United States Government. Under the terms of a contract (W-31-109-Eng-38) among the U. S. Department of Energy, Argonne Universities Association and The University of Chicago, the University employs the staff and operates the Laboratory in accordance with policies and programs formulated, approved and reviewed by the Association.

MEMBERS OF ARGONNE UNIVERSITIES ASSOCIATION

The University of Arizona
Carnegie-Mellon University
Case Western Reserve University
The University of Chicago
University of Cincinnati
Illinois Institute of Technology
University of Illinois
Indiana University
The University of Iowa
Iowa State University
The University of Kansas
Kansas State University
Loyola University of Chicago
Marquette University
The University of Michigan
Michigan State University
University of Minnesota
University of Missouri
Northwestern University
University of Notre Dame
The Ohio State University
Ohio University
The Pennsylvania State University
Purdue University
Saint Louis University
Southern Illinois University
The University of Texas at Austin
Washington University
Wayne State University
The University of Wisconsin-Madison

Available from

GPO Sales Program
Division of Technical Information and Document Control
U. S. Nuclear Regulatory Commission
Washington, D.C. 20555

and

National Technical Information Service
Springfield, Virginia 22161

NUREG/CR-2437 Vol. IV
ANL-81-77 Vol. IV

(Distribution Codes:
R3 and R5)

ARGONNE NATIONAL LABORATORY
9700 South Cass Avenue
Argonne, Illinois 60439

MATERIALS SCIENCE DIVISION LIGHT-WATER-REACTOR SAFETY RESEARCH PROGRAM: QUARTERLY PROGRESS REPORT

October—December 1981

Walter E. Massey, Laboratory Director
Charles E. Till, Associate Laboratory Director

Date Published: May 1982

Previous reports in this series

ANL-81-42	October—December 1980
ANL-81-77 Vol. I	January—March 1981
ANL-81-77 Vol. II	April—June 1981
ANL-81-77 Vol. III	July—September 1981

Prepared for the Division of Reactor Safety Research
Office of Nuclear Regulatory Research
U. S. Nuclear Regulatory Commission
Washington, D. C. 20555
Under Interagency Agreement DOE 40-550-75

NRC FIN Nos. A2016, A2017, A2212

MATERIALS SCIENCE DIVISION
LIGHT-WATER-REACTOR SAFETY
RESEARCH PROGRAM:
QUARTERLY PROGRESS REPORT

October—December 1981

ABSTRACT

This progress report summarizes the Argonne National Laboratory work performed during October, November, and December 1981 on water-reactor-safety problems. The research and development areas covered are Environmentally Assisted Cracking in Light Water Reactors, Transient Fuel Response and Fission-product Release, and Clad Properties for Code Verification.

NRC FIN No.	
A2016	Transient Fuel Response and Fission-product Release
A2017	Clad Properties for Code Verification
A2212	Environmentally Assisted Cracking in Light Water Reactors

TABLE OF CONTENTS

TABLE OF CONTENTS (CONTD.)

MATERIALS SCIENCE DIVISION
LIGHT-WATER-REACTOR SAFETY RESEARCH PROGRAM: QUARTERLY PROGRESS REPORT

October—December 1981

EXECUTIVE SUMMARY

I. ENVIRONMENTALLY ASSISTED CRACKING IN LIGHT-WATER REACTORS[a]

The experimental facility for acoustic-emission leak detection is now completely operational. Tests have been run on steam and water leaks through circular orifices and slits and through field-induced intergranular stress-corrosion cracks (IGSCCs). Preliminary results on frequency spectra and minimum detectable leakage rates have been obtained.

Characterization of the sensitization behavior as a function of heat-treating time and temperature is continuing for the three heats of Type 304 and the one heat of Type 316NG stainless steel currently being used in the program. Measurements are also being carried out on the ASTM round-robin EPR test specimens.

A baseline test for IGSCC growth rate under constant load has been completed. The test was carried out at a stress intensity of $K \simeq 18.7$ MPa $m^{\frac{1}{2}}$, which is lower than that for most of the currently available data.

Work on the experimental facilities is continuing. A second MTS/autoclave system for simultaneous crack-growth measurements on three 1T compact-tension specimens is now operational. Baseline constant extension rate tests on two heats of Type 304 stainless steel are continuing. Stress/strain/strain-rate characterization tests of sensitized stainless steel are under way.

---

[a] RSR FIN Budget No. A2212; RSR Contact: J. Muscara.

Residual stress measurements on the mock-up weldments prepared by Battelle Pacific Northwest Laboratories have been completed. The automatic welding procedure seems to yield more consistent results from weld to weld than conventional manual welding techniques, yet the average residual stresses for the two procedures are quite comparable. Thus the procedure seems satisfactory for preparing weldment and pipe-test specimens.

II. TRANSIENT FUEL RESPONSE AND FISSION-PRODUCT RELEASE[b]

As the noble gases play a major role in establishing the interconnection of escape routes from the interior to the exterior of the fuel, a realistic description of volatile fission-product (VFP) release must a priori include a realistic description of fission-gas release and swelling. The steady-state and transient gas release and swelling subroutine, FASTGRASS, has been modified to include a mechanistic description of VFP (I, Cs, CsI, Cs_2MoO_4, and Cs_2UO_4) behavior. Phenomena modeled are the chemical reactions between the VFPs, VFP migration through the fuel, and VFP interaction with the noble gases.

The initial response of nuclear reactor fuel undergoing a thermal transient is very critical in determining the final outcome of the accident. Transient fission-gas behavior can be a key factor in determining the severity of the accident. Grain-boundary separation (or microcracking) can often short-circuit normal, slower processes of gas release from within the fuel grains to the fuel exterior. The Chen-Argon creep cavitation model is coupled to the FASTGRASS computer code for the prediction of gas release and fuel microcracking. Model predictions for total gas release and radial profiles of separated grain-boundary area per unit volume are compared with results of out-of-reactor transient tests on irradiated LWR fuel.

---

[b] RSR FIN Budget No. A2016; RSR Contact: G. P. Marino.

III. CLAD PROPERTIES FOR CODE VERIFICATION[c]

Zircaloy fuel cladding is susceptible to local breach-type failures during power transients in LWRs because of stresses imposed by differential thermal expansion of the fuel and cladding. In this program, the effect of strain rate and temperature on the deformation characteristics of irradiated Zircaloy fuel cladding is being investigated to provide mechanical-property information and a failure criterion for the cladding under loading conditions conducive to pellet-cladding interaction (PCI). The information will be used in the development of codes to analyze PCI in fuel rods from power-ramp experiments in test reactors, and to evaluate the susceptibility of extended-burnup fuel elements and new fuel-element designs in commercial reactors to PCI failures during power transients.

The fracture characteristics of several irradiated Zircaloy cladding specimens from stress-rupture tests under internal-gas pressurization loading at 325°C have been evaluated by SEM and TEM. Although the diametral strain at failure for all specimens was small ($\lesssim 1.0\%$), differences were noted in the macroscopic failure mode; both ductile failures (rupture) and brittle failures (a pinhole or tight crack opening) were observed. Scanning and transmission electron micrographs of the specimens that failed in a ductile manner revealed a moderate extent of microvoid coalescence on the fracture surface and numerous dislocation tangles, cell structures, and preferential slip. In contrast, the specimens that failed in a brittle manner in the absence of fission-product species in the test environment exhibited pseudocleavage plus fluting over a large part of the fracture surface, which was similar in appearance to the surfaces produced by in-reactor PCI-type failures. A TEM evaluation of the cladding in the vicinity of the through-wall defect revealed numerous locations that contained an agglomeration of extremely fine precipitates, primarily in the cell-wall regions of the stress-relieved material. The brittle failure appears to be strongly associated with the fine precipitate, which has not been identified at this time.

---

[c] RSR FIN Budget No. A2017; RSR Contact: H. H. Scott.

The apparatus for investigating the deformation and fracture characteristics of irradiated Zircaloy cladding at low strain rates under mandrel-loading conditions has been assembled and initial calibration tests have been performed. Several mandrel-loading experiments were conducted at 25°C on unirradiated cladding segments that were oxidized in steam at high temperature to simulate the relatively low ductility and high yield strength of irradiated Zircaloy. These tests provided information on the linearity, accuracy, and reproducibility of the loading system, the magnitude of the arbor load required to produce an axial crack in the high-strength material, the optimum specimen length, and procedures for remote handling of the irradiated specimens in the hot cell. The results indicate that the mandrel design and testing procedures are capable of producing reliable deformation data at low diametral strains that are of interest in PCI situations. Based on these results, segments of spent fuel cladding that was irradiated in the H. B. Robinson reactor are being prepared for an initial series of in-cell tests.

I. ENVIRONMENTALLY ASSISTED CRACKING IN LIGHT WATER REACTORS

Principal Investigators:
W. J. Shack, T. F. Kassner, D. S. Kupperman, J. Y. Park,
P. S. Maiya, W. Ruther, F. A. Nichols,
T. Claytor, and R. W. Weeks

The objective of this program is to develop an independent capability for prediction, detection, and control of intergranular stress-corrosion cracking (IGSCC) in light-water reactor (LWR) systems. The program is primarily directed at IGSCC problems in existing plants, but also includes the development of recommendations for plants under construction and future plants. The scope includes the following: (1) development of the means to objectively and quantitatively evaluate acoustic leak detection systems; (2) evaluation of the influence of metallurgical variables, stress, and the environment on IGSCC susceptibility, including the influence of plant operations on these variables; and (3) examination of practical limits for these variables to effectively control IGSCC in LWR systems. The experimental work during the first year of the program will concentrate primarily on problems related to pipe cracking in LWR systems. However, ongoing research work on other environmentally assisted cracking problems involving pressure vessels, nozzles, and turbines will be monitored and assessed, and where unanswered technical questions are identified, experimental programs to obtain the necessary information will be developed to the extent that available resources permit.

The effort is divided into six subtasks: (A) Leak Detection and Nondestructive Evaluation; (B) Analysis of Sensitization; (C) Crack Growth Rate Studies; (D) Evaluation of Nonenvironmental Corrective Actions; (E) Evaluation of Environmental Corrective Actions; and (F) Mechanistic Studies. These subtasks reflect major technical concerns associated with IGSCC in LWR systems, namely: leak and crack detection, the role of materials susceptibility, the role of stress in crack initiation and propagation, and the role of the environment. The program seeks to evaluate potential solutions to IGSCC problems in LWRs, both by direct experimentation (including full-scale welded pipe tests) and through the development of a better basic understanding of the various phenomena.

A. Leak Detection and Nondestructive Evaluation (D. S. Kupperman and T. Claytor)

1. Introduction

a. Leak Detection

Early detection of leaks in nuclear reactors is necessary in order to detect deteriorating or failed components and minimize the release of radioactive materials. Before a nuclear power facility can be placed into operation, the NRC requires that operational leak-detection systems of various kinds be installed. However, it is assumed that the equipment cannot be perfectly leak-tight, and some allowance is therefore made for leakage from packing, shaft seals, and other equipment. These leaks are called identified leaks, and their flow is monitored during plant operation. Thus, even with the system operating normally, there may be some accumulation of water in the sumps, with a concomitant increase in the level of radioactivity. However, it is expected that these levels of radioactivity and leakage will be reasonably constant with time.

No currently available single leak-detection method combines optimal leakage detection sensitivity, leak-locating ability, and leakage measurement accuracy. For example, while quantitative leakage determination is possible with condensate flow monitors, sump monitors, and primary coolant inventory balance, these methods are not adequate for locating leaks and are not necessarily sensitive enough to meet code requirements. Acoustic methods represent the most promising area for improvement in leak detection. They have the best chance of success when specific welds are monitored, and the least when a few probes are used to monitor many welds. However, the ability to locate leaks and quantify leak rates using acoustic techniques is not well established, especially since virtually no data are available on acoustic signals from field-induced IGSCC.

b. Nondestructive Evaluation

In recent years numerous cracks have been discovered in coolant systems of LWRs. Although the main problems have been in BWR primary coolant lines, cracking has occurred in PWR feedwater piping and low-temperature, low-pressure lines near the spent-fuel storage pool. It is desirable to detect any cracks in the primary and secondary coolant boundary and fix them within a reasonable length of time for safety-related as well as practical reasons; the NRC "defense-in-depth" philosophy requires that all possible efforts be considered which may prevent a nuclear accident.

Many of these cracks were missed during ultrasonic ISI and detected only because of leakage, thereby raising doubts concerning the capability of ultrasonic ISI to detect cracks. The present ASME Code Section V and XI ultrasonic testing procedures for ferritic weldments do not appear to be adequate for the detection and evaluation of IGSCC in austenitic stainless steel (SS) piping. The detection of IGSCC before the cracks have grown large enough to cause a leak, and the detection, location, and sizing of leaks once they occur, are very difficult technical goals to achieve. IGSCC that can be detected by conventional ultrasonic testing under laboratory conditions may be missed during a field examination by even the most skilled operator.

c. Objectives

The objective of this subtask is to (1) develop an independent capability to assess the effectiveness of current and proposed techniques for acoustic leak detection (ALD) in reactor coolant systems, (2) develop a strategy for hardware realization, and (3) examine potential improvements in ultrasonic methods for detection of IGSCC and inspection of cast SS. The program will establish whether meaningful quantitative data on leak rates and location can be obtained from acoustic signatures of leaks due to cracks (IGSCC and fatigue) in low- and high-pressure lines, and whether these can be distinguished from other types of leaks. It will also establish calibration procedures for acoustic data acquisition and show whether advanced signal processing can be employed to enhance the adequacy of ALD schemes.

2. Technical Progress

a. Facility Development

The ALD facility was described in the previous report in this series.[1] During the past quarter, a larger preheater was installed in the leak generating system, and the tubing was redirected so that both the high- and low-flow meters could be used during the same test. The computer data acquisition system was completed. Temperature, pressure, water flow rate, and acoustic signal strength can now be recorded simultaneously and continuously during a test. In addition, the Tektronix computer was successfully interfaced to the Spectral Dynamics signal processor. A photograph of the ALD system is shown in Fig. 1.

b. Acoustic Spectra of Steam Leaks

Six plugs, three each with slit-type and hole-type artificial leaks, were fabricated during the past quarter for use in the test pipe. Figure 2 schematically illustrates the two types of plugs. The length of the leak channel from entrance to exit was 1.27 cm in all cases. The holes were 0.343, 0.520, and 0.787 mm in diameter; the EDM channels were 25.4, 50.8, and 76.2 μm ±5 μm deep, with entrance and exit widths of 5.08 and 1.27 mm, respectively. Individual parts of the slit-type leak assembly were silver plated, cryogenically slip-fit together, and finally diffusion bonded.

Three natural IGSCC cracks were obtained from a defective LWR core spray line of Type 304 SS. An ∿100-mm-square specimen, containing one throughwall crack confined to a nonweld area, was machined from the core spray line and welded into the test pipe. This crack was 10-20 μm wide, with entrance and exit lengths of 19 and 2 mm, respectively. Figure 3 shows a leak from this crack at a pressure of ∿1000 psi (7 MPa), a water temperature of ∿500°F (260°C), and a flow rate of ∿0.002 gal/min (8 cm^3/min). The plume appears to be almost all steam. As the temperature is lowered to ∿250°F (120°C), the liquid phase becomes more evident and the flow rate increases as the fluid density increases and the flow resistance in the crack decreases.

Two transducers, a Dunegan Endevco (DE) model S9204 (S/N 1432) and an Acoustic Emission Co. FAC-500 (S/N 35130), were used to measure and characterize the acoustic leak spectra produced by the artificial leaks and natural crack described above. The FAC-500 transducer has a very uniform response over the frequency range of 100 kHz to 2 MHz; however, it is not very sensitive. It was mounted on the pipe via a thin steel wedge (Fig. 4a) coated with vacuum grease as a couplant. The DE transducer was attached to a waveguide (Fig. 4b), and holes were drilled and tapped in the test pipe at various locations to accept the waveguide. Transducer-waveguide combinations of this type offer several advantages (i.e., low cost, high sensitivity, and ease of replacement) for application to leak detection in reactor piping. However, the end of the waveguide would have to be held in contact with the pipe by means other than drilled and tapped holes, and the best technique for in-situ calibration of the acoustic emission transducers would have to be determined.

Acoustic spectra of the natural IGSCC crack were measured at frequencies up to 2 MHz at a distance of 112 cm from the leak with the DE transducer, and at a distance of 109 cm with the FAC-500. A preliminary set of spectral data extending to 1 MHz, obtained with the DE transducer, is shown in Fig. 5. No significant spectral power was observed at frequencies above 500 kHz in any of the tests. In the series of tests shown in Fig. 5, as the temperature was reduced from 470°F (243°C) to 60°F (16°C), the water flow remained essentially constant but the sound level decreased. (More typically, both flow and sound level increase with decreasing temperature.) However, even with cold water seeping through the crack, a measurable amount of noise was produced. The structure evident in the spectra is probably due to the waveguide and transducer resonances rather than to an intrinsic characteristic of the leak. At 950 psi (6.7 MPa), the drop in signal strength at 200 kHz was about 10 dB for a decrease in temperature from 470 to 260°F (243 to 127°C) and a decrease in flow rate from 0.004 to 0.003 gal/min (16 to 12 cm^3/min).

A test to determine the relative intensities of the signals generated by gas and multiphase water flow through the same orifice was performed on the 76.2-μm slit leak. The acoustic spectra for high-pressure hot water and hot nitrogen gas were measured with the FAC-500 transducer. The results are shown in Fig. 6. Single-phase gas leaks produced stronger signals than steam/water leaks under similar conditions: At 200 kHz, the difference in signal strength was ∿6 dB. As the temperature of the water is increased, and more liquid changes to steam, the spectrum for the steam/water leak shown in Fig. 6 should approach that for nitrogen gas.

Theories are available that describe the generation of acoustic and ultrasonic noise by turbulent flow of a gas or liquid through a pipe. A description of the noise generated by a crack such as that of Fig. 5 is approximated qualitatively by turbulent fluid flow through a very thick-walled pipe with a small ID. This is possible since the noise is generated at the turbulent boundary layer at the solid/fluid interface. The interface areas should be equivalent for this approximation to be valid. The pressure fluctuations on the pipe wall obey the relationship[2]

$$P_f \propto \rho_f v_f^4 \quad , \tag{1}$$

where ρ_f is the fluid density and v_f is the fluid velocity. From Eq. (1), it is obvious that both liquid (ℓ) and gas (g) flow will generate noise. However, for a pipe with cross-sectional area A,

$$Q_m = \rho_g v_g A = \rho_\ell v_\ell A \quad , \tag{2}$$

where Q_m is mass flow rate; since $\rho_g << \rho_\ell$, $v_g >> v_\ell$ and the noise due to gas flow will greatly dominate the noise generated by liquid flow. This suggests that high-pressure steam leaks will generate more acoustic noise than fluid leaks and hence should be more readily detected. However, the differences in the noise levels from liquid and gas flows will be smaller when small orifices are considered and friction and choking effects are taken into account.

We are evaluating cross-correlation as a means of achieving improved detection sensitivity for location of leaks even in the presence of background noise. The cross-correlation for time τ is defined to be

$$R_{xy}(\tau) = \lim_{T\to\infty} \frac{1}{T} \int_o^T x(t)y(t+\tau)dt \quad , \qquad (3)$$

where x(t) and y(t) are the input time domain signals over record length T. Incoherent background noise (such as flow noise) will average approximately to zero as the inverse of the number of data records averaged.

An initial cross-correlation test was performed, using the experimental arrangement shown in Fig. 7. The transducers were positioned near the ends of the test pipe, a total of 10 m (∿30 ft) apart. An electromagnetic driver, situated 2.13 m from accelerometer 1, was excited with white noise (1-50 kHz). Noise signals were received at the two accelerometer positions and were amplified and filtered to yield signals with frequencies between 25 and 30 kHz. The filtered signals were then either cross-correlated directly or sent to an rms detector and then correlated. Results of these two analyses are shown in Fig. 8. The time delay $\Delta\tau$ (given by the digital readout), sound velocity c, and transducer locations d_1 and d_2 are related by the formula

$$\Delta\tau = \tau_1 - \tau_2 = \frac{d_1 - d_2}{c} \quad . \qquad (4)$$

From the time delay of 3.2 ± 0.1 ms, a value of $1.78 \pm 0.05 \times 10^3$ m/s was deduced for the sound velocity. For a frequency of 25 kHz, a velocity of 1.79×10^3 m/s was expected for symmetric flexural waves in the test pipe. This traveling wave is the wave that is most strongly excited by the leak. The theoretical velocity for this traveling wave can be computed from the formula[3]

$$\frac{1}{3}\,\delta^2(2N - S^2)(1 - m^2/12)[F_1] + (2N - S^2)[F_2] - \left(\frac{2N\sigma Km}{\pi}\right)^2 = 0 \qquad (5)$$

where

$\delta = hf/c$ where h is the pipe wall thickness, f the frequency, and c the flexural wave velocity,

$N = \frac{1}{(1 - \sigma)}$ where σ is the Poisson ratio,

$S = C/C_S$ where C_S is the velocity of shear waves (see below),

$m = h/R$ where R is the pipe radius,

$$F_1 = (2\pi K\delta)^2 - (2\pi S\delta)^2 + 2Nm^2(1 + m^2/12) \text{ where } K = (\pi^3/12)^{1/2},$$

and

$$F_2 = \left(\frac{2}{\pi}\right)N(Km)^2(1 + m^2/12) - (2KS\delta)^2 - \frac{4}{3}\,\sigma N(\delta mK)^2 - \frac{4}{3}\,(\sigma N\delta m)^2 \;.$$

In the above formulation, $C_S = G/\rho$, where G is the shear modulus and ρ is the pipe material density. Equation (5) was solved numerically to yield C as a function of f. As frequency increases, C increases. For example, at 100 kHz, the velocity would be 2515 m/s. In the limit of very high frequencies, C approaches the Rayleigh wave velocity (above 3100 m/s for steel).

During the next quarter we will attempt to correlate leak signals from an IGSCC crack and slits or holes. Also, the correlation technique will be investigated at frequencies higher than 30 kHz. This is important because the best signal-to-noise ratio in a reactor system will probably occur at frequencies greater than 50 kHz.

A sample of Type 304 SS containing a laboratory-induced IGSCC crack grown by the graphite wool technique was received from the Electric Power Research Institute. This small crack will be used to generate acoustic leak signals by replacing the slits presently used in the nonradioactive end of the ALD system with the cracked piece, cut to fit the existing plate. Such tests will enable an effective quantitative comparison of acoustic signals generated by fluid flowing at comparable rates through cracks and through artificial leaks of simple geometry.

c. Ultrasonic Nondestructive Testing

Cast SS pipe specimens, obtained from Battelle Pacific Northwest Laboratories (PNL), are being prepared for sound-velocity measurements to establish the anisotropy variations in cast SS and the effect on flaw detection using conventional and unconventional techniques.

Shear waves of varying polarization were used to examine 304 SS flat-plate samples with various degrees of roughness simulated by a grating-type surface. The analysis results suggest that information about such a surface can be generated by varying the polarization of the shear waves. Similar efforts will be carried out using a field-induced crack from a 10-in. core spray line, to explore possible means to distinguish cracks from other reflectors.

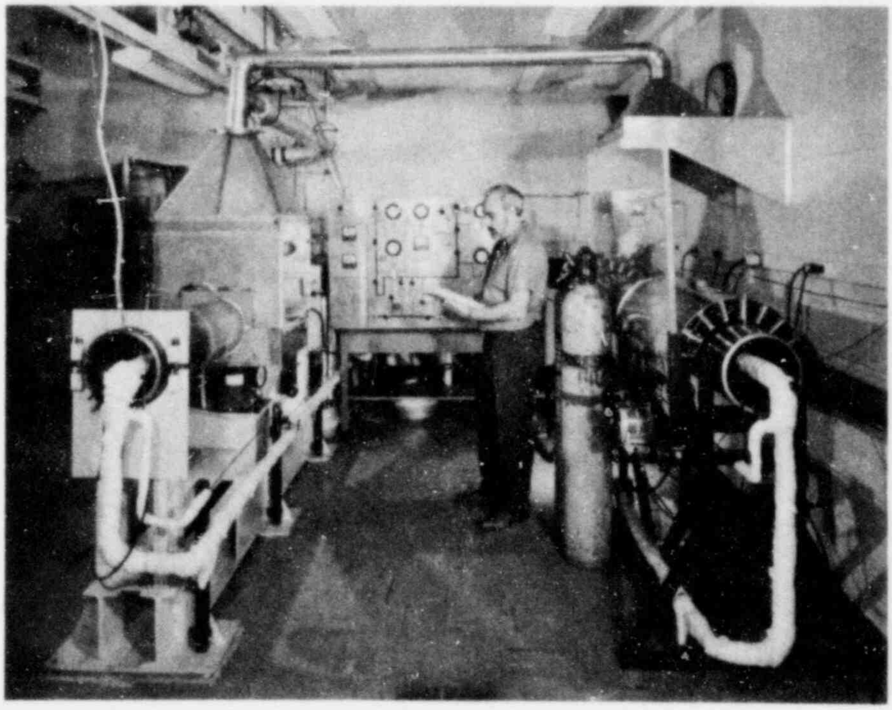

Fig. 1. Photograph of the Acoustic Leak Detection System.

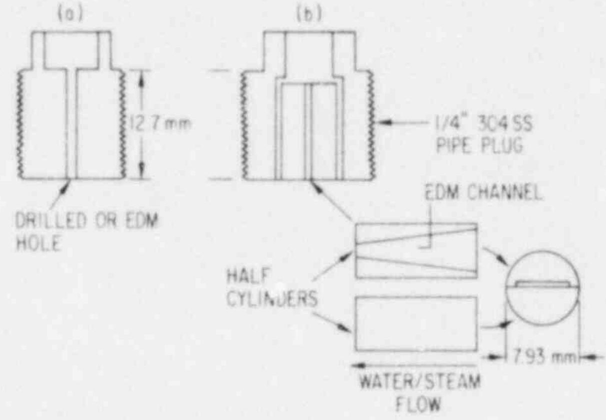

Fig. 2. Schematic of Pipe Plugs Containing (a) Hole-type and (b) Slit-type Artificial Leaks.

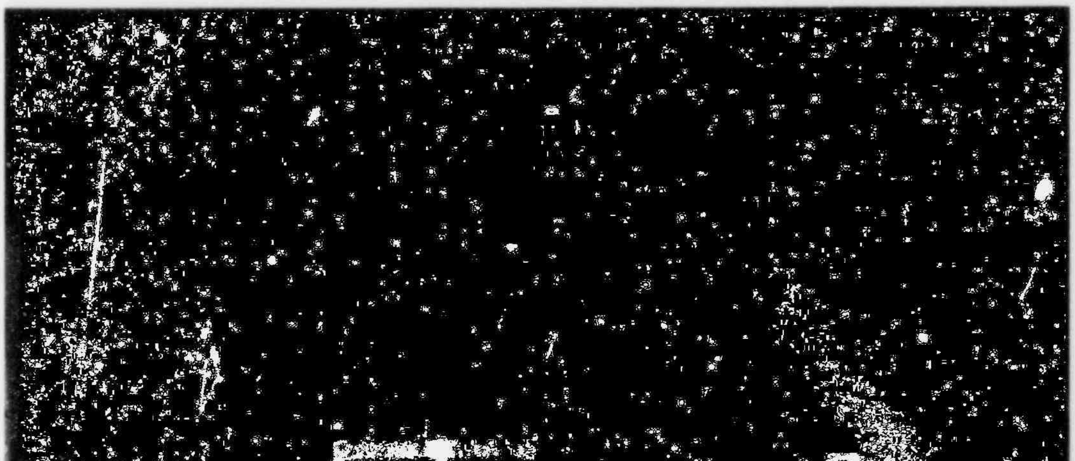

Fig. 3. Photograph of a Leak from the Field-induced Axial IGSCC. The plume appears to be almost all steam.

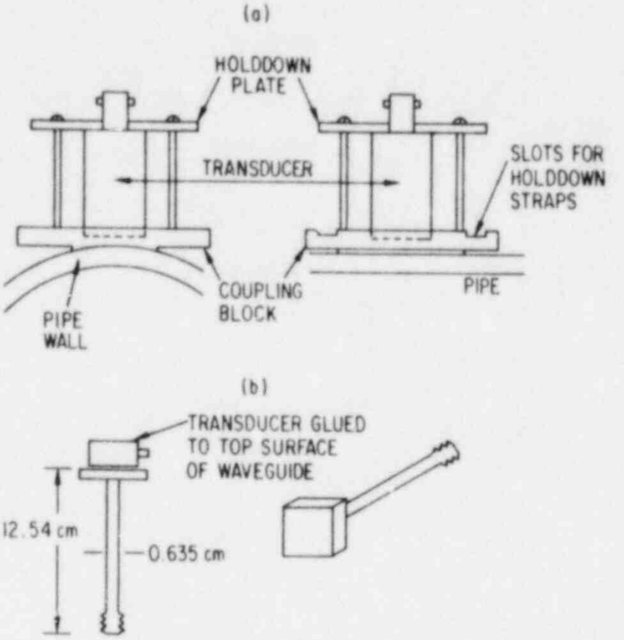

Fig. 4. Schematics of Methods Used to Attach (a) Acoustic Emission Co. FAC-500 and (b) Dunegan Endevco Model S9204 Transducers to Test Pipe.

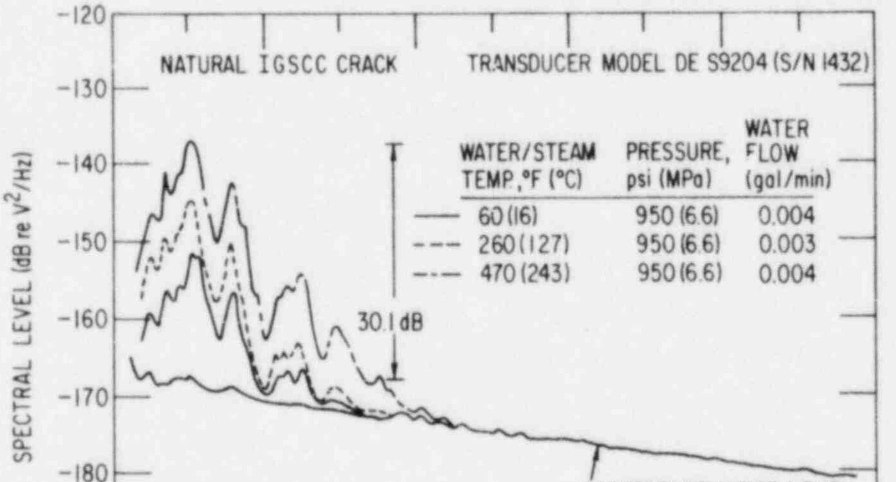

Fig. 5. Acoustic Spectra of Steam and Water Leaks from a Field-induced IGSCC Crack.

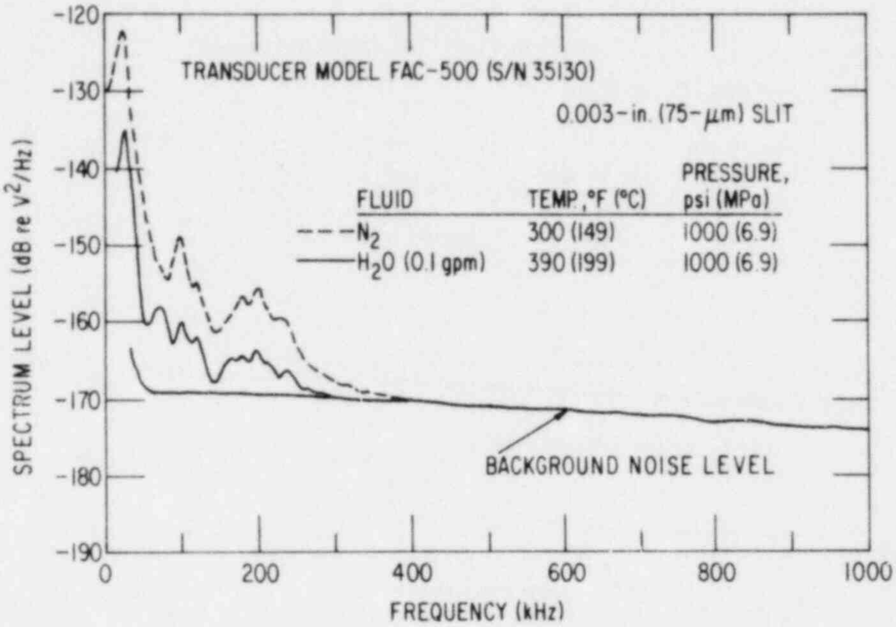

Fig. 6. Comparison of Spectra Obtained with Gas and Steam/Water Flow through a 75-μm Slit-type Artificial Leak.

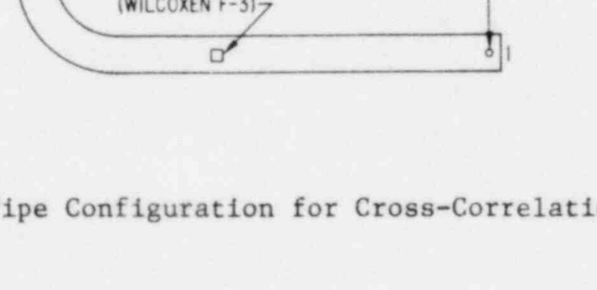

Fig. 7. Pipe Configuration for Cross-Correlation Test.

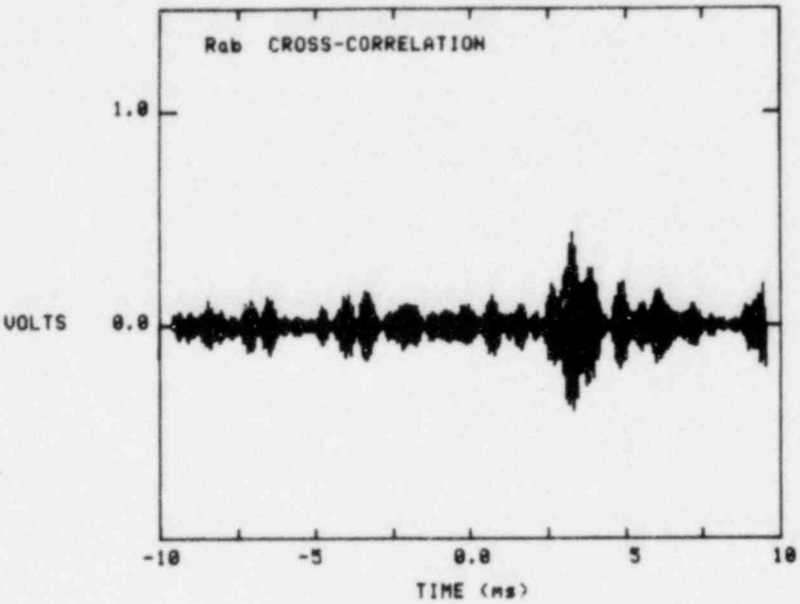

(a)

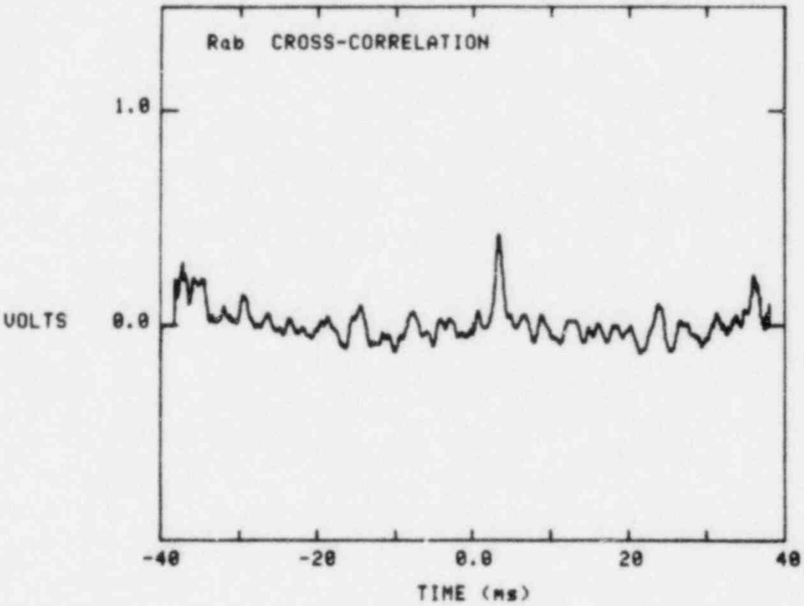

(b)

Fig. 8. Results of Cross-Correlation Analyses with Electronic Noise Source. (a) Raw correlation data; (b) cross-correlation with demodulated signal.

B. Analysis of Sensitization (J. Y. Park)

1. Introduction

The microstructural changes resulting from thermal exposure, which produce susceptibility to intergranular corrosion (IGC), are collectively known as sensitization. Sensitization is one of the major causative factors in the IGSCC of austenitic stainless steels in LWR environments. It is believed that chromium carbide precipitation and concomitant depletion of chromium concentration in regions adjacent to grain boundaries are responsible for sensitization.[4]

Sensitization of austenitic stainless steels such as Types 304 and 316 occurs in the temperature range of about 500 to 850°C under normal isothermal heat treatment. However, Type 304 SS may be sensitized at temperatures below this range if carbide nuclei are present at grain boundaries.[5] This phenomenon is referred to as low-temperature sensitization (LTS). The LTS phenomenon in Type 304 SS in the temperature range of 350 to 500°C has been demonstrated in laboratory experiments. Various laboratory measurements show large differences in the apparent activation energy for different heats of material and types of specimen; values ranging from ~40 to 65 kcal/mol have been reported.[6] The value of the activation energy is extremely important in assessing the possibility of LTS in operating reactors, since extrapolation predicts that at 300°C, LTS would occur within 10 years at 40 kcal/mol and about 1000 years at 65 kcal/mol. These variations have been attributed to differences in the amounts of strain, dislocation densities, and/or impurity element contents of the materials, but with the current level of understanding, the susceptibility to LTS of arbitrary heats of material cannot be assessed.

One way to detect and measure sensitization is by assessing susceptibility to IGC. Various chemical and electrochemical tests of IGC have been discussed in the literature (e.g., Ref. 7). Five standard tests for detecting susceptibility of stainless steels to IGC, designated ASTM A262 Practices A through E,[8] have been adopted by the ASTM. Although not yet established as an ASTM practice, electrochemical tests for sensitization appear promising. They seem to be much more sensitive at low degrees of sensitization. The most widely studied test of this type is the electrochemical potentiokinetic reactivation (EPR) technique, the use of which is relatively well established for Types 304 and 316 SS.

The objectives of subtask B are to establish the importance of LTS of materials under long-term reactor operating conditions, and to evaluate the quantitative capability of the EPR technique to identify the susceptibility of piping material to IGSCC. The investigations to be conducted include the following: (a) studies on the effect of thermomechanical history on LTS, (b) assessment of predictive methods for LTS, (c) examination of possible adverse effects of stress-improvement remedies and LTS possibility in alternate materials, (d) studies on the effect of LTS on IGSCC susceptibility, and (e) evaluation of the EPR technique and other types of sensitization measurements for applicability to alternate materials.

2. Technical Progress

EPR measurements have been performed on furnace-sensitized Type 304 (Heat Nos. 10285 and 30956) and Type 316NG (Heat No. P91576) SS specimens. The results are summarized in Table I. In the mill-annealed condition, grain-boundary etching was not apparent in any of the heats of material. A solution heat treatment (1050°C, 0.5 h) did not appreciably influence the EPR value of the Type 304 SS (Heat No. 30956) specimens that were subsequently sensitized at 700°C for 2 or 4 h. An LTS treatment at 450°C for 257 h resulted in EPR values of 10 and 15 C/cm^2 for specimens of Heat Nos. 30956 and 10285, respectively. The same LTS treatment produced no measurable sensitization of the Type 316NG SS. Heat treatments at 700°C for 4 h and at 650°C for 24 and 70 h also failed to sensitize the Type 316NG SS material. It appears from the results of the LTS treatment at 450°C that Heat No. 30956 is less susceptible to sensitization than Heat No. 10285, although the carbon contents of both heats are the same (0.06%). Figure 9 shows EPR values for Heat No. 30956 versus square root of heat treatment time at 650 and 700°C. Assuming Arrhenius behavior of time-temperature-sensitization,[4] an activation energy of 54 kcal/mol for EPR values of 13 to 15 C/cm^2 is obtained from Fig. 9.

The repetitive EPR measurement procedure was discussed in an earlier report.[9] Preliminary results from highly sensitized (>15 C/cm^2) Type 304 SS specimens showed that the effect of repetitive polarization on the EPR value was so small that this procedure could be used for multiple data generation. In contrast, the EPR value for lightly sensitized specimens decreases significantly with repetitive polarizations, as shown in Fig. 10. The decrease in the EPR value may have been caused by dissolution and removal of a discontinuous network of chromium-depleted grain-boundary regions at the specimen surface, or by the formation of a surface film during the preceding polarization. Thus, the repetitive polarization procedure does not appear to be useful for lightly sensitized specimens.

Eight ASTM round-robin EPR test specimens (second series) were received from ASTM Committee G-1 08. The specimen holder of the Princeton Applied Research Model 350 unit was modified to be compatible with these specimens. The specimens are being ground and polished.

The stability of applied load in the constant-load SCC test facility has been examined. A load fluctuation of up to ±3% was observed over a 12-hour period. Pressure accumulators will be installed to reduce the load fluctuations.

Table I. EPR Measurements on Types 304 and 316NG SS Subjected to Various Heat Treatments

Alloy	Heat No.	Heat Treatment	EPR, C/cm^2
304	30956	Mill-annealed	NGA[a]
		650°C/4 h	9
		650°C/24 h	16
		700°C/2 h	13
		700°C/4 h	14
		SHT[b] plus 700°C/2 h	13
		SHT plus 700°C/4 h	14
		SHT plus 700°C/10 h	18
		SHT plus 700°C/15 h	22
		SHT plus 700°C/16 h	23
		SHT plus 700°C/15 min plus 500°C/24 h	2
		700°C/15 min plus 500°C/24 h	9
		700°C/10 min plus 450°C/257 h	10
	10285	Mill-annealed	NGA
		700°C/15 min plus 452°C/120 h	8
		700°C/10 min plus 450°C/257 h	15
316NG	P91576	Mill-annealed	NGA
		650°C/24 h	
		650°C/70 h	
		700°C/4 h	
		700°C/10 min plus 450°C/257 h	

[a] NGA: No grain-boundary attack.

[b] SHT: Solution heat treatment, 1050°C/0.5 h.

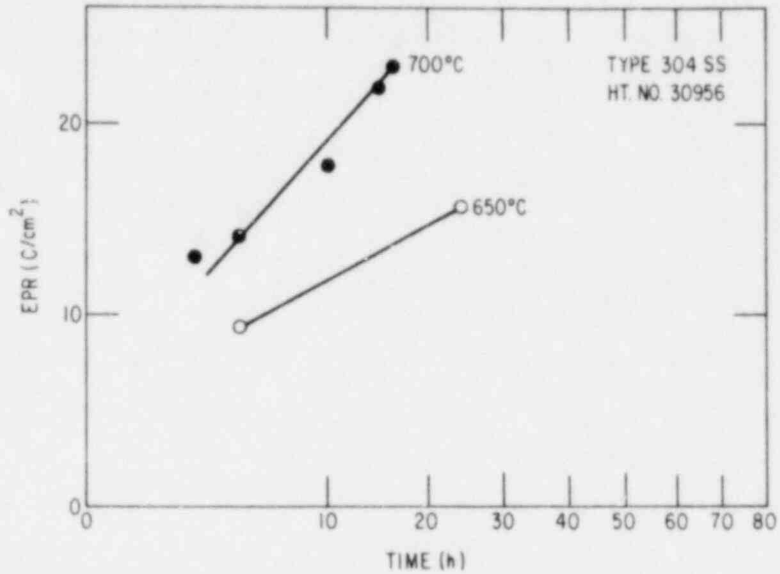

Fig. 9. EPR vs Heat Treatment Time for Type 304 SS (Heat No. 30956) at 650 and 700°C.

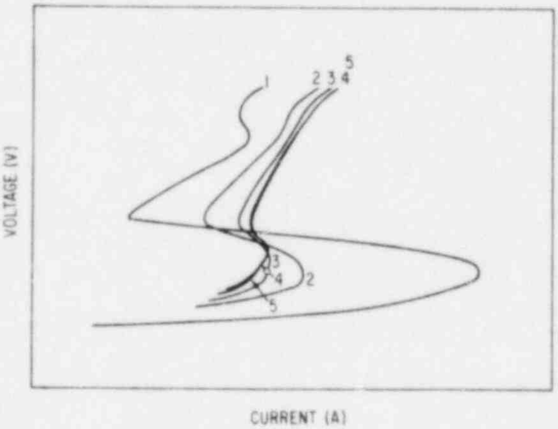

Fig. 10. Repetitive EPR Measurements of Lightly Sensitized Type 304 SS. Numbers on curves represent the sequence of the measurements.

C. Crack Growth Rate Studies (J. Y. Park and W. J. Shack)

1. Introduction

The early instances of IGSCC in operating BWRs generally occurred in smaller pipes, and the response to the detection of IGSCC was generally to repair or replace the cracked piping immediately. It is now clear that for reactors with standard Type 304 SS piping material, cracking can occur anywhere in the recirculation system, including the main recirculation line. Because of the severe economic consequences of long forced outages for repair or replacement, the utilities will consider other approaches for dealing with cracked pipe.

Understanding crack growth behavior is, of course, important for other reasons besides assessing the safety implications of flawed piping. A better understanding would permit a more rational extrapolation of laboratory test results to the prediction of operating-plant behavior. Current work on the measurement of crack growth rates seeks to characterize these rates in terms of the linear elastic fracture mechanics (LEFM) stress intensity as well as the level of sensitization and the amount of oxygen present in the coolant. However, both current mechanistic studies of crack growth and some experimental data indicate that contrary to the LEFM model, in which the crack velocity depends only on the current value of the crack-tip stress intensity K, the crack velocity depends strongly on the geometry of loading and on the nature of the remote external loading (constant extension rate, constant applied force, and constant displacement).

The work under subtask C is aimed at a systematic evaluation of the validity of the use of LEFM to predict IGSCC growth. The capability of data obtained under one type of loading history to predict crack growth under a different loading history will be investigated. The effect of specimen geometry on crack propagation rates will also be considered.

2. Technical Progress

A crack growth rate test on a compact tension (1TCT) specimen with an applied stress intensity of $K = 18.7\ \mathrm{MPa\ m^{\frac{1}{2}}}$ in a BWR-type environment with 8 ppm oxygenated water at 289°C has been performed. The specimen was fabricated from Type 304 SS (Heat No. 10285) and was furnace-sensitized to an EPR level of $8\ \mathrm{C/cm^2}$. The specimen was cycled under a sawtooth waveform with a slow rise (∿495 s) and a rapid unloading (∿5 s) with a peak stress intensity $K = 18.7\ \mathrm{MPa\ m^{\frac{1}{2}}}$ and $R = 0.1$ to initiate the crack. Previous experience has shown that cyclic loading at these low frequencies produces intergranular cracking; this will be checked in the post-test examination. Compliance measurements indicated that a crack had initiated after ∿1100 cycles. The test was then continued under constant load ($K \simeq 18.7\ \mathrm{MPa\ m^{\frac{1}{2}}}$). In-situ compliance measurements during the latter part of the test indicated crack growth at a rate $\dot{a} = 2.5$ mm/yr. After incremental crack growth of ∿0.3 mm, the test was interrupted because of a pump failure and resulting oil contamination. After the pump was repaired, the test was resumed under the same cyclic load used before to restart crack growth. The specimen has accumulated over 5000 load cycles since resumption of the test, but no evidence of additional crack growth has been obtained from the in-situ compliance method. Testing on this specimen will be terminated if crack growth is not reinitiated within an additional 3000 load cycles, and new 1TCT specimens will be tested.

Efforts have continued to set up an ac potential measurement system as an alternative to the present compliance technique. Potential measurements permit continuous monitoring without the need to interrupt the loading cycle. This method has now been used to measure crack length in mock-up 1TCT specimens containing EDM notches. A sensitivity of 0.85 volts/in. for crack-length increment and a temperature dependence of 0.07 volts/°C were observed. In order to obtain calibration for real cracks, fatigue cracking of mock-up 1TCT specimens will be studied.

D. Evaluation of Nonenvironmental Corrective Actions (P. S. Maiya and W. J. Shack)

1. Introduction

The fundamental premise of the current efforts to prevent IGSCC in BWR piping is that IGSCC involves a complex interaction between material susceptibility (sensitization), the stresses acting on the material, and the environment, and that by suitably altering or varying these parameters immunity from IGSCC can be produced. Nonenvironmental corrective actions seek to mitigate either the material susceptibility or the state of stress on the inside surface of the weldment. They include techniques for improving the margin against IGSCC of a susceptible material like Type 304 SS and the identification of alternate materials that are inherently more resistant to IGSCC.

In the initial development and discussion of proposed remedies and alternate materials, the focus was on reducing the severity of the stress levels or the sensitization. However, since a quantitative understanding of the role of stress or sensitization in IGSCC does not exist, the actual benefits of each remedy must be assessed through actual SCC susceptibility tests. The objective of the current work is an independent assessment of the proposed remedies developed by the utilities and the vendors. Additional testing and research will be carried out to eliminate gaps in the existing data base on alternative materials and fabrication and to develop a better understanding of the relation between the existing laboratory results and satisfactory in-reactor operating performance. Current efforts in this task include additional screening tests for alternate materials, environmental pipe tests under alternate loading conditions, and the study of stress redistribution near weldments to determine the effect of in-service loading conditions on residual stress improvement techniques.

2. Technical Progress

a. CERT Experiments

Some preliminary tests have been conducted on Type 304 SS (Heat No. 0590019) welded with Type E308L SS to investigate the IGSCC resistance of the welded material as well as to develop a consistent surface preparation technique.

The chemical composition of the weld metal and the geometry of the specimens have been described in a previous quarterly report.[10] The chemical composition (wt %) of the base metal is as follows: 0.06 C, 0.57 Si, 0.96 Mn, 0.026 P, 0.012 S, 8.53 Ni, 18.25 Cr, and balance Fe. All the CERT test specimens taken from weldments were cut so that the weld fusion line (WFL) was close to the center of the uniform-gauge section, and the specimen axis was parallel to the rolling direction. All the test results reported here were obtained at a strain rate of $2 \times 10^{-6}\ s^{-1}$. The experiments were performed at 289°C in water with 8 ppm oxygen at a pressure of 1300 psi (9.0 MPa). The flow rate in the system was 8.1 cm^3/min.

The initial diameter and the diameter of the fracture surface (at the junction created by bringing the two surfaces back into contact) were measured with a contour projector at a magnification of 50X. These were used to calculate the reduction in area $\Delta A/A_o$, defined as $(A_o - A_f)/A_o$ where A_o is the initial cross-sectional area and A_f is the area of the fracture surface. The maximum stress σ_{max} is defined in the engineering sense as the maximum load divided by the initial area A_o; the elongation to failure ε_f was calculated by measuring the specimen gauge length before and after the test. These values are consistent with those obtained from the time to failure and the (calibrated) strain rate, i.e., the total elongation ε_t is $\dot{\varepsilon} \times t_f$ where $\dot{\varepsilon}$ is the strain rate and t_f is the time to failure. The slight discrepancies between the two can be attributed to difficulties in measuring the length of the failed specimens. Following the tests, the fracture surfaces were examined by scanning electron microscopy.

The CERT test results for the three specimens are shown in Table II. Fracture in all cases is observed to be ductile, and etching of the gauge section revealed that failure had occurred in the weld metal. A typical fracture surface is shown in Fig. 11. This material, in spite of its relatively high carbon level, seems resistant to IGSCC at a strain rate of $2 \times 10^{-6}\ s^{-1}$ even after relatively severe heat treatments. We are now investigating further the behavior of furnace-sensitized specimens, which are easier to characterize than weldments. These studies should help us to better understand the behavior of this heat of material.

Specimens 03 and 04 had different degrees of surface finish: The gauge sections were polished with 3-μm diamond paste and ground with 600-grit silicon carbide paper, respectively. As expected, the CERT results appeared to be insensitive to surface finish; however, as failure did not occur by IGSCC, these findings are hardly conclusive.

b. Stress/Strain/Strain-Rate Relations for Sensitized Materials

For a proper understanding of IGSCC under a variety of loading histories, an understanding of the influence of stress, strain, and strain rate on the plastic deformation of Type 304 SS and other alternate materials under different heat-treatment (sensitization) conditions is required. Currently, only limited information is available on the stress/strain/strain-rate behavior of sensitized Type 304 SS at the temperatures of interest. Therefore, experiments on load relaxation are being initiated on Type 304 SS (Heat No. 0590019) in both the solution-annealed and sensitized conditions at 28 and 289°C.

The purpose of the initial experiment (at 28°C) reported here was to check out the procedure for obtaining stress/strain/strain-rate data from load-relaxation experiments. A uniaxial round specimen with a diameter of 2.47 mm and a gauge length of 25.59 mm, fabricated from pipe material, was tested in the as-received condition. The experimental procedures were similar to those originally developed by Hart and Solomon.[11] An initial load corresponding to 1.4 σ_y, where σ_y is the yield stress [σ_y = 37 ksi (254 MPa)], was attained with a nominal crosshead speed of 2 mm/min. The relaxation run lasted slightly more than 10^6 s, with an initial plastic strain of 1.22% (this value increases during relaxation). As can be seen from a log-log plot of stress versus (inelastic) strain rate (Fig. 12), the relaxation covered more than 5 decades of strain rate ($\sim 2 \times 10^{-4}$ to 5×10^{-10} s^{-1}). A systematic study has begun on this heat of material in the solution-annealed and sensitized conditions.

c. Residual Stress Measurements and Analysis

Residual stress measurements have been completed on a third pipe weldment, designated NRC3, which was prepared at PNL by use of an automatic welding procedure. This procedure will be used to prepare specimens for the pipe tests that will be performed at PNL and is expected to give more consistent and reproducible welds than manual welding procedures. The joint geometry, weld parameters, and details of the strain measurements were described in an earlier report.[12]

The distribution of axial and hoop stresses on the inner surface is shown in Fig. 13. As in the case of the first two weldments, the distribution of stress is somewhat closer to axisymmetric than is typically found for the manually welded case, and the peak stresses are generally smaller. The results for the two types of weld procedures are summarized in Tables III and IV. At a given distance from the weld, the peak stresses (both axial and hoop) tend to be somewhat lower for the weldments prepared by automatic welding. The variation of stresses both with azimuthal position and between weldments is smaller for the automatically welded specimens. However, the average values obtained by considering all the weldments of each type are similar.

These experimental measurements have been supplemented by finite-element calculations of the residual stresses associated with each welding procedure. These calculations were carried out by E. F. Rybicki of the University of Tulsa. The manual welds were seven-pass welds. However, the pipe was modeled as being welded in four layers. The finite-element mesh, which includes both weld crown and drop-through regions, is shown in Fig. 14. The heat inputs used in the analysis are shown in Table V. The heat inputs are calculated from the actual current and voltage used, assuming that 75% of the electrical power supplied is actually transferred to the pipe. This efficiency is consistent with estimates by other workers. The temperature-dependent material properties for Type 304 SS that were used in the analysis are shown in Fig. 15.*

The residual stresses along the inner pipe surface after manual welding are shown in Figs. 16 and 17 for axial and circumferential stresses, respectively. Also included in the figures for comparison are the experimental values summarized in Table IV. The experimental values are plotted in terms of the average values obtained for all the manually welded pipes and the range indicated is plus or minus three times the rms variation. The trends of the computed and measured stresses are in rough agreement. However, in general, the computed stresses are lower than the range of experimental data. This is because the heat inputs used in modeling the manual weld were lower than those associated with the data (this was due to a mixup in the description of the welding conditions). Other analyses[13] have shown that increasing the weld heat input will increase the weld residual stresses.

The finite-element mesh and material properties for the automatically welded pipe are identical with those used for the manually welded pipe. However, the heat inputs (Table V) are different for the two processes: The automatic welding process uses lower heat inputs for the first two layers and higher heat inputs for the last two. The computed stresses on the inner surface of the automatically welded pipe are shown in Figs. 18 and 19 for the axial and hoop components, respectively. The experimental values are again shown in terms of the average value obtained from all the

---

*It appears that the high-temperature values of the elastic modulus shown in Fig. 15 are in error. More reasonable values can be obtained by linear extrapolation of the data for T < 1400°F to higher temperatures. This will probably not affect the results significantly, but some numerical checks will be made.

automatically welded pipes and a range equal to plus or minus three times the rms variation. The agreement is quite good for the axial stresses (Fig. 18); however, the model overestimates the hoop stresses near the weld (Fig. 19). The calculations also predict a greater difference between the residual stresses associated with the two welding processes than is shown by the experimental results. These discrepancies may decrease when the calculations for the manual welds are redone using the correct heat inputs.

Table II. CERT Test Results on Type 304/E308L Weld

Specimen No.	Heat Treatment	σ_{max}, MPa	$\frac{\Delta A}{A}$, %	Total Elongation, %	
				From Chart	From Specimen
02	As Welded	390.2	57.3	23.6	27.3
03	As Welded + 500°C/24 h	405.1	49.7	25.2	25.5
04	As Welded + 500°C/24 h	443.9	54.0	28.4	31.7

Table III. Residual Stresses on Inner Surfaces of Automatically Welded Pipes

	Distance from Weld Fusion Line (mm)			
	2	7	12	
Weldment NRC1				
Average Axial Stress	131	117	14	MPa
	19	17	2	ksi
Average Hoop Stress	179	96	14	MPa
	26	14	2	ksi
Peak Axial Stress	219	252	106	MPa
	31	35	15	ksi
Peak Hoop Stress	270	179	43	MPa
	38	25	6	ksi
Root-Mean-Square Variation in Axial Stress	41	69	55	MPa
	6	10	8	ksi
Root-Mean-Square Variation in Hoop Stress	90	55	34	MPa
	13	8	5	ksi
Weldment NRC2				
Average Axial Stress	136	117	41	MPa
	20	17	6	ksi
Average Hoop Stress	172	96	0	MPa
	25	14	0	ksi
Peak Axial Stress	212	233	94	MPa
	30	33	13	ksi
Peak Hoop Stress	246	173	151	MPa
	34	24	21	ksi
Root-Mean-Square Variation in Axial Stress	28	41	28	MPa
	4	6	4	ksi
Root-Mean-Square Variation in Hoop Stress	41	28	48	MPa
	6	4	7	ksi
Weldment NRC3				
Average Axial Stress	193	69	-7	MPa
	28	10	-1	ksi
Average Hoop Stress	179	69	-41	MPa
	26	10	-6	ksi
Peak Axial Stress	284	154	124	MPa
	40	22	17	ksi
Peak Hoop Stress	244	151	120	MPa
	34	21	17	ksi
Root-Mean-Square Variation in Axial Stress	48	34	41	MPa
	7	5	6	ksi
Root-Mean-Square Variation in Hoop Stress	41	34	34	MPa
	6	5	5	ksi
All Automatic Weldments				
Average Axial Stress	152	103	14	MPa
	22	15	2	ksi
Average Hoop Stress	179	90	-7	MPa
	26	13	-1	ksi
Root-Mean-Square Variation in Axial Stress	21	28	28	MPa
	3	4	4	ksi
Root-Mean-Square Variation in Hoop Stress	34	21	21	MPa
	5	3	3	ksi

Table IV. Residual Stresses on Inner Surfaces of Manually Welded Pipes

	Distance from Weld Fusion Line (mm)			
	∿2	∿8	∿16	
W27A				
Average Axial Stress	158	96	-76	MPa
	23	14	-11	ksi
Average Hoop Stress	186	7	-145	MPa
	27	1	-21	ksi
Peak Axial Stress	249	234	64	MPa
	35	33	9	ksi
Peak Hoop Stress	246	137	-51	MPa
	41	19	-7	ksi
Root-Mean-Square Variation in Axial Stress	28	41	28	MPa
	4	6	4	ksi
Root-Mean-Square Variation in Hoop Stress	34	28	34	MPa
	5	4	5	ksi
W27B				
Average Axial Stress	110	-	14	MPa
	16	-	2	ksi
Average Hoop Stress	158	-	-55	MPa
	23	-	-8	ksi
Peak Axial Stress	367	-	159	MPa
	51	-	22	ksi
Peak Hoop Stress	413	-	59	MPa
	58	-	8	ksi
Root-Mean-Square Variation in Axial Stress	117	-	158	MPa
	17	-	23	ksi
Root-Mean-Square Variation in Hoop Stress	110	-	96	MPa
	16	-	14	ksi
W27C				
Average Axial Stress	214	186	-	MPa
	31	34	-	ksi
Average Hoop Stress	214	234	-	MPa
	31	34	-	ksi
Peak Axial Stress	315	326	-	MPa
	44	46	-	ksi
Peak Hoop Stress	401	346	-	MPa
	56	48	-	ksi
Root-Mean-Square Variation in Axial Stress	41	28	83	MPa
	6	4	12	ksi
Root-Mean-Square Variation in Hoop Stress	41	28	48	MPa
	6	4	7	ksi

Table V. Parameters for Welding of a 4-inch Schedule 80 Pipe by Two Different Procedures

Layer	Manual Welding		Automatic Welding	
	Arc Speed, cm/s	Heat Input*, kJ/cm	Arc Speed, cm/s	Heat Input*, kJ/cm
1	0.14	12.5	0.14	7.6
2	1.10	11.6	0.14	6.3
3	0.30	5.1	0.17	5.3
4	0.30	3.5	0.13	5.3

*At 75% efficiency.

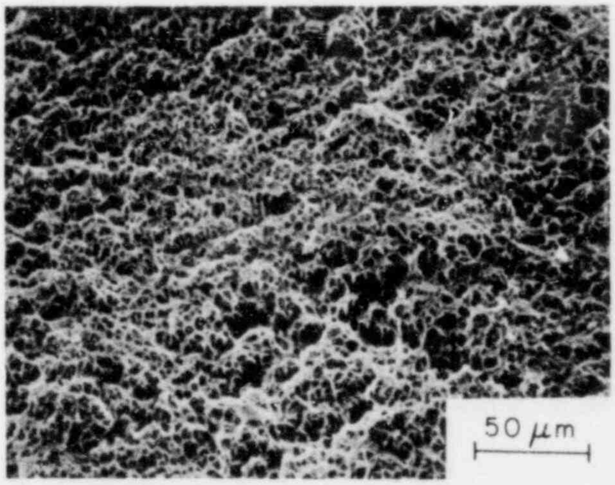

Fig. 11. Scanning Electron Micrograph of the Fracture Surface of Specimen 03.

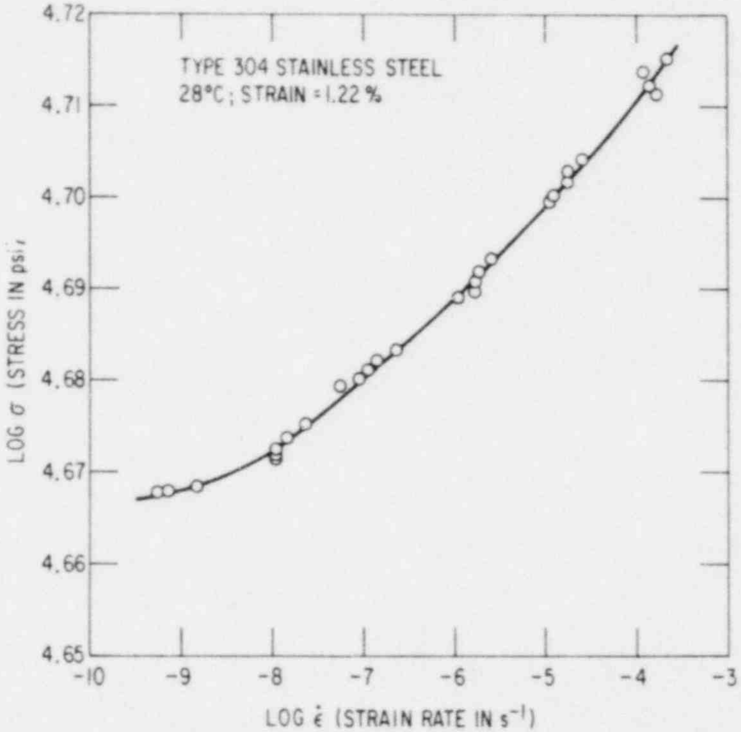

Fig. 12. Log Stress Versus Log Strain Rate for Type 304 SS at 28°C. Conversion factor: 1 psi = 6.895×10^3 Pa.

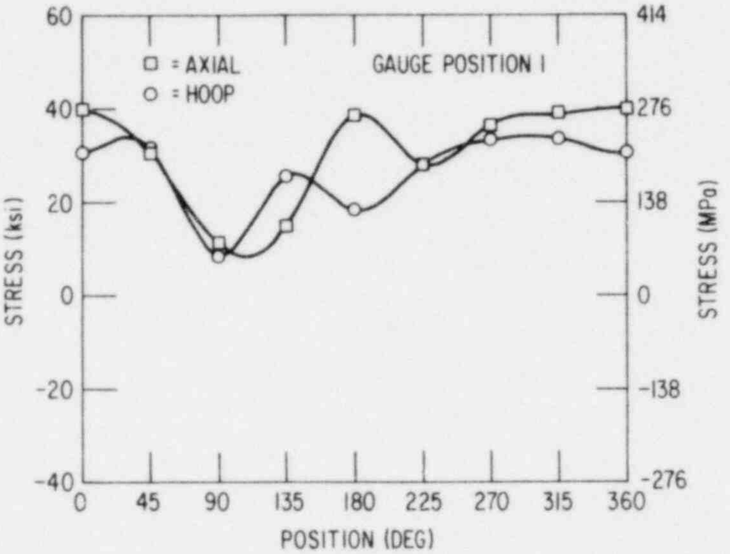

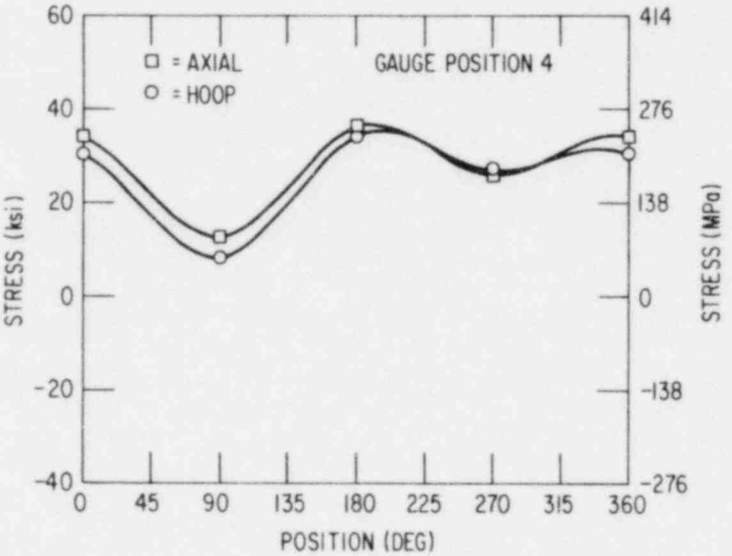

Fig. 13. Residual Stress Distributions on the Inner Surface of Weldment NRC3. Gauge positions 1 and 4 are ∿2 mm from the weld fusion lines (WFLs) on either side of the weld; gauge positions 2 and 5 are ∿7 mm from the WFLs; gauge positions 3 and 6 are ∿12 mm from the WFLs.

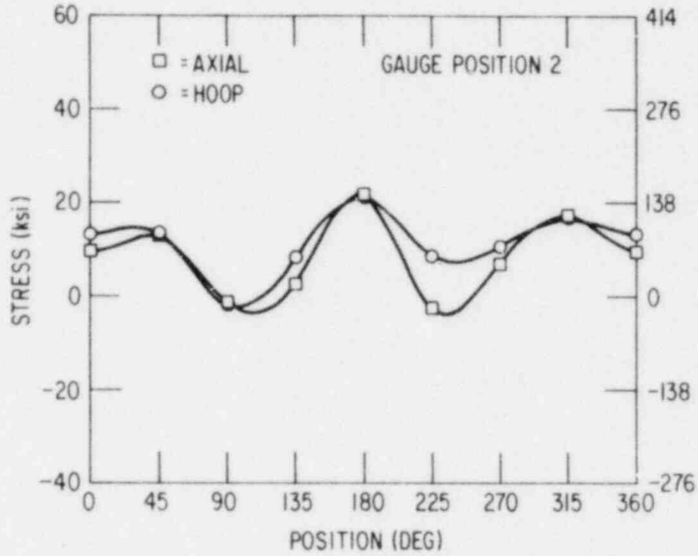

60
40
20
0
-20
-40
414
276
138
0
-138
-276
STRESS (ksi)
STRESS (MPa)
□ = AXIAL
○ = HOOP
GAUGE POSITION 2
0
45
90
135
180
225
270
315
360
POSITION (DEG)

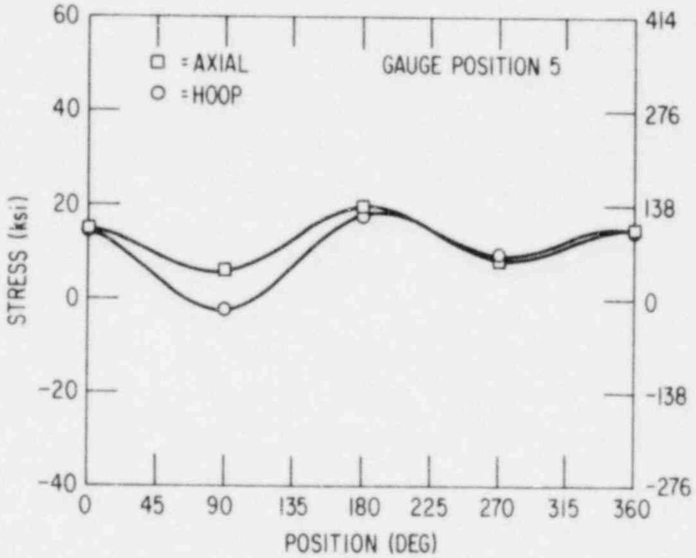

60
40
20
0
-20
-40
414
276
138
0
-138
-276
STRESS (ksi)
STRESS (MPa)
□ = AXIAL
○ = HOOP
GAUGE POSITION 5
0
45
90
135
180
225
270
315
360
POSITION (DEG)

Fig. 13. (Contd.)

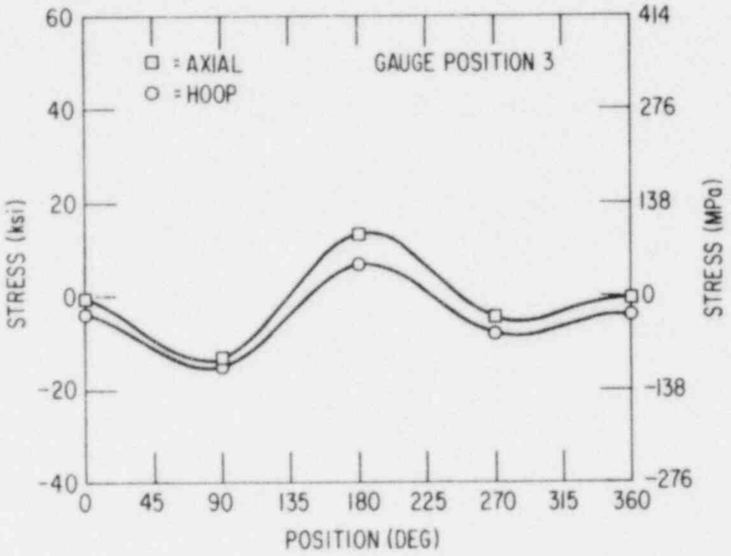
□ = AXIAL
○ = HOOP
GAUGE POSITION 3
STRESS (ksi)
STRESS (MPa)
POSITION (DEG)
60
40
20
0
-20
-40
414
276
138
0
-138
-276
0
45
90
135
180
225
270
315
360

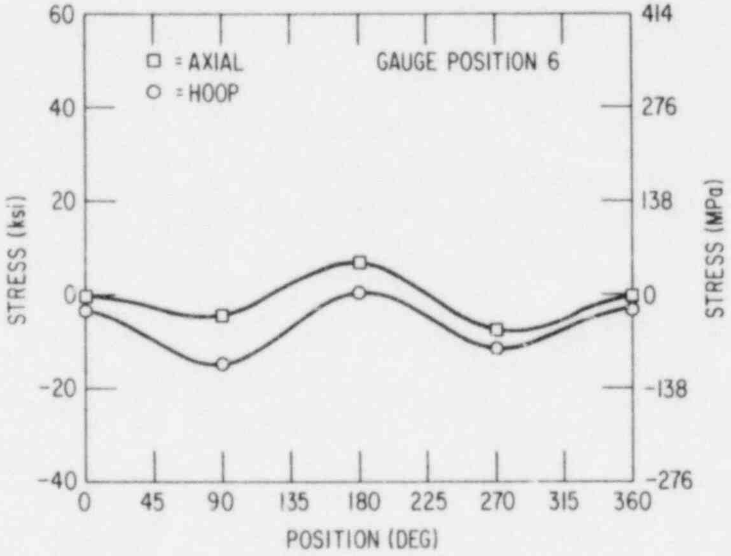
□ = AXIAL
○ = HOOP
GAUGE POSITION 6
STRESS (ksi)
STRESS (MPa)
POSITION (DEG)
60
40
20
0
-20
-40
414
276
138
0
-138
-276
0
45
90
135
180
225
270
315
360

Fig. 13. (Contd.)

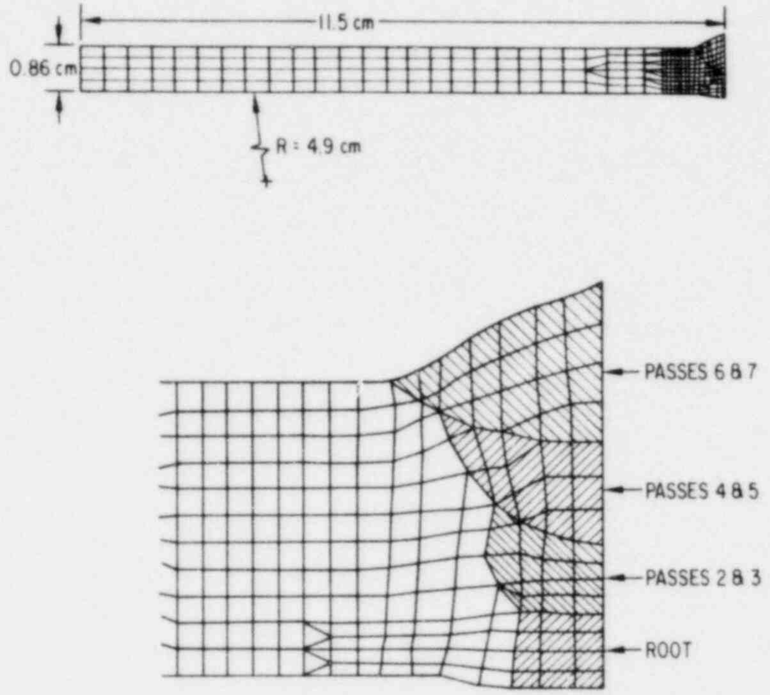

Fig. 14. Finite-Element Mesh for Residual Stress Calculations.

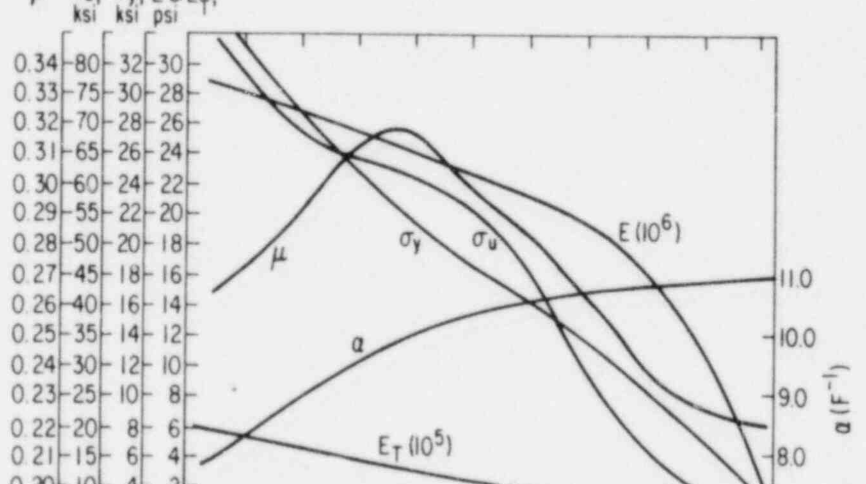

Fig. 15. Temperature-dependent Mechanical Properties of Type 304 SS Used for Finite-Element Stress Analysis.

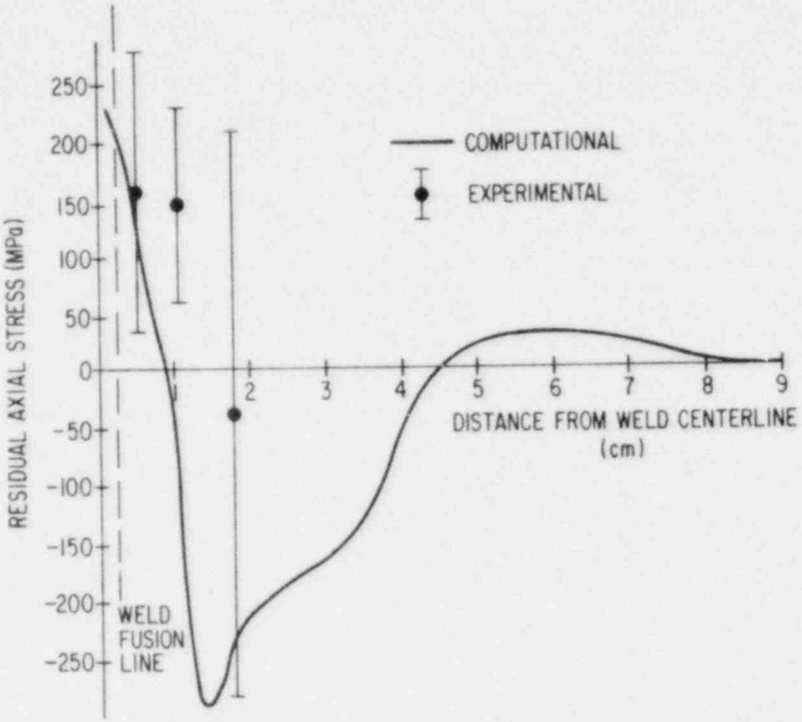

Fig. 16. Computed and Measured Residual Axial Stresses along the Inner Surface of a 4-inch Schedule 80 Manually Welded Pipe.

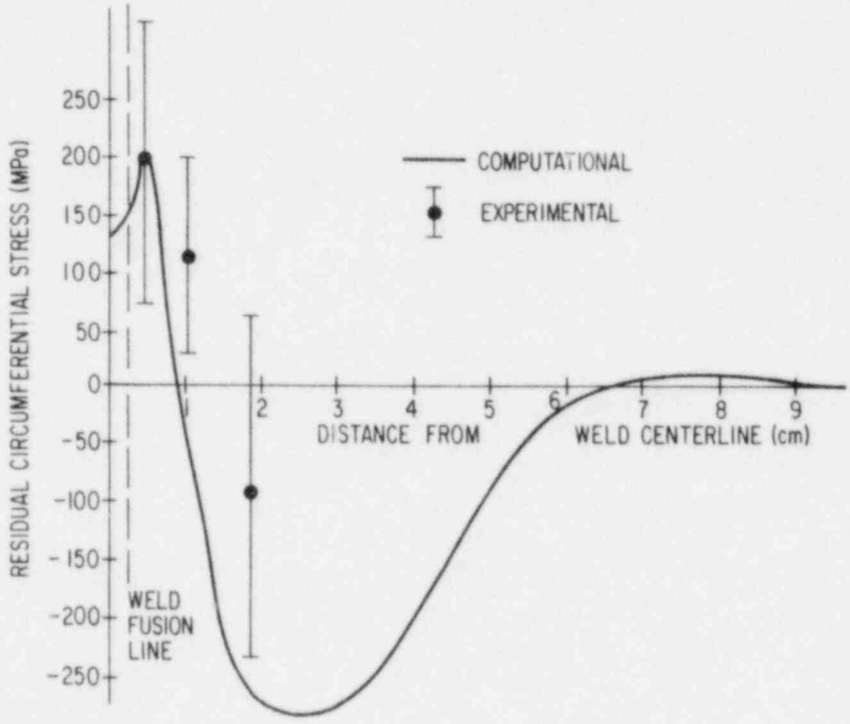

Fig. 17. Computed and Measured Residual Circumferential Stresses along the Inner Surface of a 4-inch Schedule 80 Manually Welded Pipe.

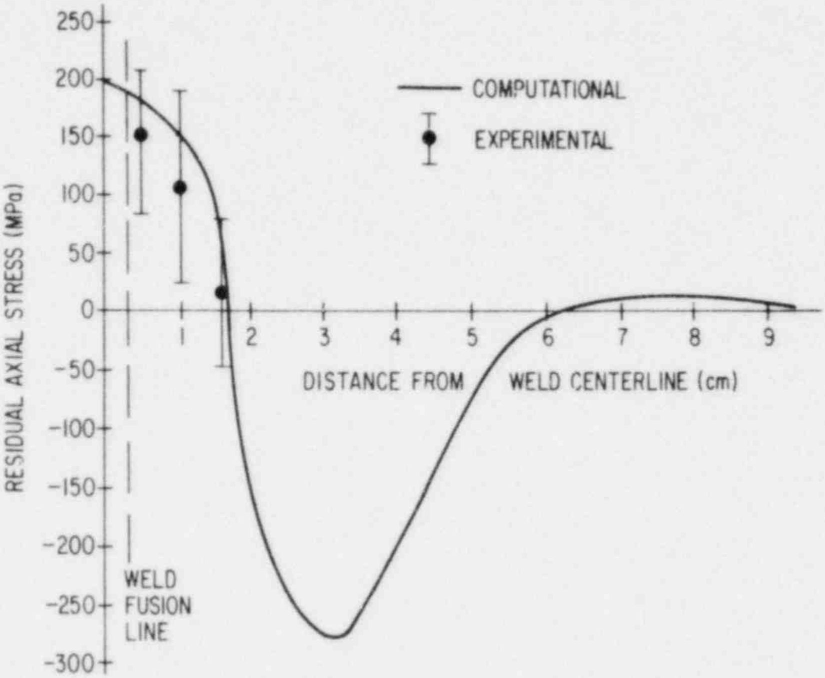

Fig. 18. Computed and Measured Residual Axial Stresses along the Inner Surface of a 4-inch Schedule 80 Automatically Welded Pipe.

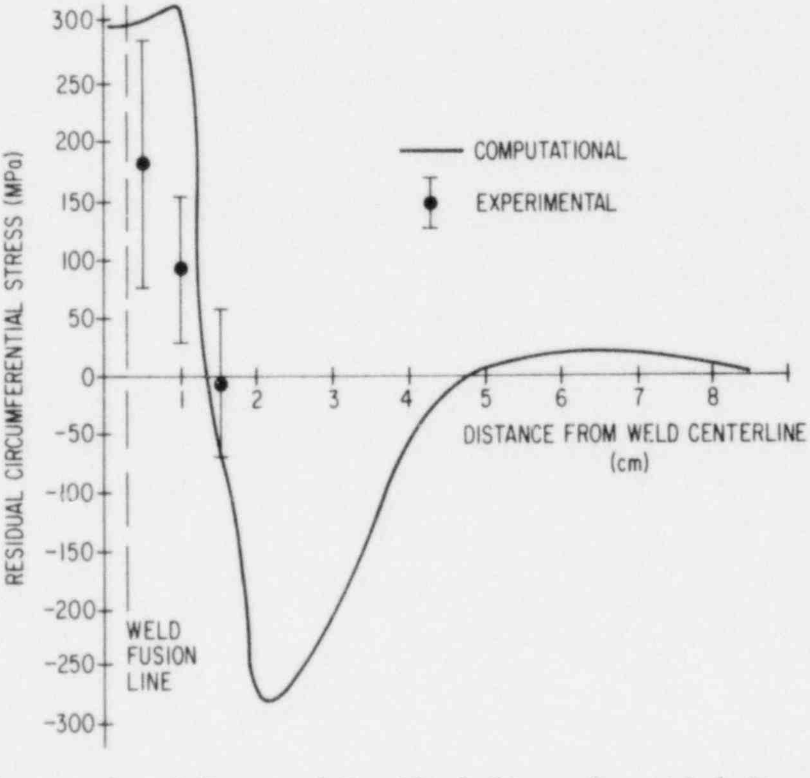

Fig. 19. Computed and Measured Residual Circumferential Stresses along the Inner Surface of a 4-inch Schedule 80 Automatically Welded Pipe.

E. Evaluation of Environmental Corrective Actions (W. E. Ruther and T. F. Kassner)

1. Introduction

The reactor coolant environment under both normal and off-normal water-chemistry conditions has a profound influence on the performance and reliability of nuclear power-plant components. The problems of IGSCC of weld-sensitized Type 304 SS piping in BWRs, the accelerated corrosion of carbon steel support plates with the concomitant cracking of Inconel tubes in PWR steam generators, and the environmentally assisted cracking of turbine disk materials are being evaluated by the NRC, reactor vendors, and electrical utilities relative to plant safety and reliability issues. Furthermore, the economic incentive to maintain plant availability, due to the high cost of replacement power from fossil-fired units, has resulted in extensive research programs sponsored by EPRI and Reactor Owners Groups to develop technical solutions to these problems and methods for implementation of the technology.

The objective of Subtask E is to evaluate the potential effectiveness of proposed actions to solve or mitigate the problems primarily from the standpoint of water-chemistry modifications. The possibility of defining practical limits on temperature and water chemistry (pH and sulfate and chloride concentrations) during off-normal transients will also be explored. As in the other tasks, the initial emphasis of the program will be on SCC problems with austenitic SS in BWRs.

2. Technical Progress

a. Experimental Facilities

A second MTS/autoclave system for simultaneous crack-growth measurements on three 1TCT specimens has been assembled and tested at 289°C. Three MTS clip gauges were calibrated at this temperature and mounted on specimens of the reference heat of Type 304 SS (Heat No. 30956) in the solution annealed and sensitized conditions (EPR values of 0, 2, and 20). The crack-growth experiment, which will provide baseline information for tests under different water-chemistry conditions, will be conducted in high-purity water containing 8 ppm oxygen at 289°C with an R value of 0.95, $K_{max} = 28$ $MPa \cdot m^{1/2}$, and frequencies between 10^{-1} and 10^{-5} Hz.

Major components for a third MTS/autoclave system with high flow-rate capability have been ordered. An 8-liter SS autoclave system with a water circulation loop has been assembled for calibration of high-temperature pH electrodes and for use in mechanistic studies described in Subtask F.

b. Experimental Results

CERT tests are being performed on specimens of the reference heat of Type 304 SS with various degrees of sensitization in high-purity water with a range of oxygen concentrations to establish the SCC susceptibility and appropriate heat-treatment conditions for the 1TCT specimens in the crack-growth experiments. The relationship between the degree of sensitization of the steel (determined by the EPR technique) and the aging time at 700°C is shown in Fig. 20. Based on this curve, an aging time of 12 h at 700°C will be used to achieve an EPR value of 20 for the crack-growth specimens.

The experimental conditions and results from the CERT tests in high-purity water at 289°C are given in Table VI. In the last two experiments, some difficulty was encountered in maintaining the oxygen level at 0.2 ppm. This is evident from the relatively low corrosion potential (<-500 mV_{SHE}) of a stainless steel specimen located at the outlet of the autoclave. The influence of the startup method for the CERT tests was investigated in runs 6 and 7. In run 6, straining of the specimen was delayed until the potential of an electrically insulated specimen, identical with the tensile specimen in composition and heat treatment, attained the corrosion potential of the well-corroded autoclave system (i.e., ~124 h). However, in run 7, straining of the specimen commenced as soon as the temperature reached 289°C (~2 h after filling the system with water). The higher oxygen concentration in the water due to air contamination during filling of the system, coupled with the relatively high initial corrosion rate of the specimens, resulted in greater susceptibility as indicated by the decrease in time to failure, the reduction in area, and the granulated appearance of the fracture surface. The results of the two tests tend to confirm observations of Fujita et al.[14] that preoxidation of CERT specimens inhibits IGSCC even in water containing 8 ppm oxygen at 250°C.

The influence of sulfate and other impurity ions at low concentrations on the SCC susceptibility of sensitized Type 304 SS under chemical-control conditions will be established in the next series of CERT experiments.

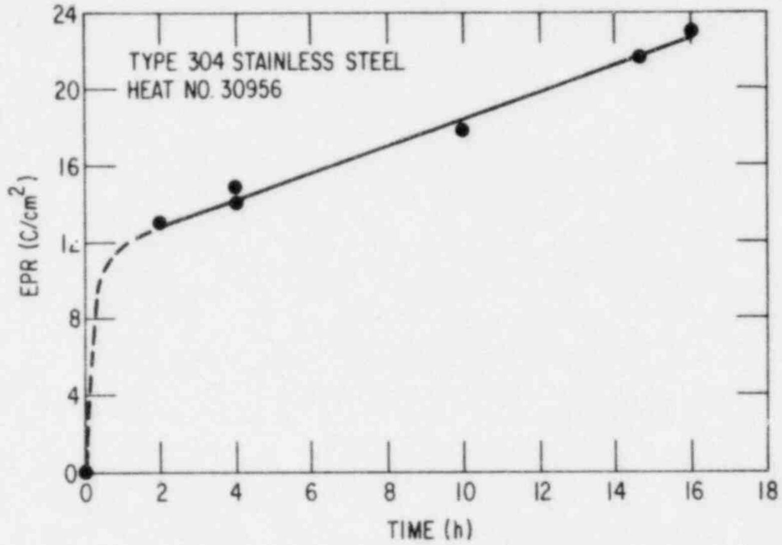

Fig. 20. Degree of Sensitization of the Reference Heat of Type 304 SS (Determined by the EPR Technique) as a Function of Aging Time at 700°C.

TABLE VI. CERT Tests on Type 304 Stainless Steel (Heat 3096)[a] in High-Purity Water at 289°C

Test No.	Strain Rate, s^{-1}	Material EPR Value, C/cm^2	Feedwater Chemistry			Open Circuit Potential,[b] mV (SHE)	Failure Time, h	Maximum Stress, MPa	Total Elong., %	Reduction in Area, %	Fracture Morphology[c]	Specimen Surface Characteristics
			Oxygen, ppm	pH at 25°C	Cond., μS/cm							
1	1×10^{-6}	2	7.3	6.8	0.3	+150	117	472	36	34	0.37I, 0.63D	-
2	↓	2	0.25	↓	0.2	-270	143	492	50	52	0.31T, 0.69D	Secondary cracking
3	↓	8.8	0.25	↓	0.2	-	149	500	52	55	0.63T, 0.37D	↓
4	↓	2	0.05	↓	0.1	-580	141	492	50	54	0.51T, 0.49D	↓
5	↓	14	0.06	↓	0.1	-610	140	491	50	48	0.46T, 0.56D	↓
6	↓	14	0.22	↓	0.2	-590	145	513	50	52	0.69T, 0.31D	↓
7	↓	15	0.21	↓	0.3	-500 (start) -590 (end)	124	521	43	35	0.34 (T + G), 0.66D	↓

[a] For the solution-annealed material in helium at 289°C and a strain rate of 2.6×10^{-6} s^{-1}, the maximum stress is 552 MPa. The uniform and total elongations are 46.8 and 54.7%, respectively, and the reduction in area was 75%. The corresponding values for sensitized material (700°C for 12 h, EPR ~20) are 525 MPa and 43.1 and 51.5% for the uniform and total elongations, respectively, and a reduction in area of 67%.

[b] Average EMF value (±30 mV) during the test for an unstressed specimen of the steel with the same heat treatment as the smooth 6.35-mm-dia. by 25.4-mm gauge-length CERT specimen.

[c] Ductile (D), Intergranular (I), Transgranular (T), Granulated (G), in terms of the fraction of the reduced cross-sectional area. (Characterization of the fracture surface morphologies is in accordance with the illustrations and definitions provided in Alternate Alloys for BWR Pipe Applications: Sixth Semiannual Progress Report, April-September 1980, NEDC-23750-8, pp. 5-70 to 5-81.)

F. Mechanistic Studies (F. A. Nichols and T. F. Kassner)

The objective of Subtask F is to develop a mechanistic understanding of SCC of reactor structural alloys in nuclear reactor environments which can aid in the evaluation of proposed environmental and metallurgical corrective actions and modified reactor operating procedures. A better mechanistic understanding of SCC processes would also provide a more rational basis for application of laboratory test results to material performance in reactor coolant circuits. Relevant SCC mechanisms are being reviewed and quantitative experimental data for materials of interest in simulated reactor coolant environments will be developed for use in predictive models of crack initiation and growth.

In this regard, Tyzack[15] has published a theory for stress corrosion based on a seemingly quantitative treatment of the slip-dissolution model, favored by many researchers. The formalism accounts for film rupture by dislocation motion and anodic dissolution and subsequent repassivation. The model incorporates a critical range for the ratio of repassivation to the film rupture rates and quantitatively relates the macroscopic strain rate to the strain rate near the crack tip. Thus, it appears to contain all of the essential elements for a mechanistically based analytical model; however, the assumptions must be carefully reviewed. Tyzack gives no data comparisons, and the dearth of appropriate experimental data severely limits an assessment of the applicability of the model.

Based upon the review of pertinent literature discussed in previous reports,[16] the feasibility of performing mechanistically oriented experiments under LWR coolant conditions is being evaluated. Where appropriate, available techniques will be used at low temperatures and pressures or adapted as necessary for autoclave conditions. The following research areas are of particular interest:

1. Straining-electrode tests (or other types of "bare-metal" electrochemical tests) of sensitized Type 304 SS under simulated LWR water-chemistry conditions.

2. Experiments to determine variations in pH and potential along an intergranular crack or crevice, and correlations with bulk-chemistry conditions.

3. Hydrogen absorption and/or permeation experiments on sensitized Type 304 SS under LWR water conditions.

4. Mode I and III straining experiments with precracked specimens under normal and off-normal LWR water-purity conditions.

5. Transmission electron microscopy of dislocation structure in the vicinity of stress-corrosion cracks.

6. Crack-growth experiments at very low frequencies and high R-values on sensitized Type 304 SS under LWR water-purity conditions at temperatures from ~120 to 290°C.

In view of the long time periods that have been encountered for initiation of stress-corrosion cracks in 1TCT specimens of sensitized Type 304 SS in oxygenated high-purity water, the initial work in this subtask will involve an investigation of the onset of crevice corrosion in sensitized SS in high-temperature simulated BWR-quality water. Mechanical stress coupled with crevice acidification and local breakdown of the passivity of the oxide film are important factors in the initiation and propagation of stress-corrosion cracks. The onset of crevice corrosion in stainless steels for different flaw geometries (including a crack-growth specimen) could be predicted from the Oldfield-Sutton[17] model if the parameters were evaluated as a function of temperature and bulk water chemistry. Evaluation of the necessary parameters involves the following: During the induction period preceding the breakdown of passivity, the flow of metal ions across the metal/liquid interface causes changes in the crevice solution composition. The flow of metal ions is characterized by the passive current, I_{pass}, although it may have two components, viz., healing of flaws by oxide growth as well as actual metal dissolution into the crevice. Once the crevice becomes deoxygenated, the crevice solution acidifies by dissolution and hydrolysis reactions. Thus, the magnitude of I_{pass} is important in determining the rate of acidification and is an essential parameter for prediction of the time for breakdown of the film.

The necessary information will be obtained by (1) determining the composition of the solution at the tip of an artificial crevice in SS (several alloy compositions and heat treatments) for different bulk water chemistries (within the range of BWR operating experience), using the methods of Taylor and Silverman,[18] and (2) potentiostatically measuring I_{pass} on specimens of steel (which were exposed to the bulk solutions for various times) in deaerated, simulated crack-tip solutions at different temperatures. When the composition of the crevice solution achieves a critical pH and Cl^- or SO_4^{-2} concentration, permanent breakdown of passivity occurs. In natural crevices or cracks, a sharp fall in the corrosion potential, E_{corr}, to the active region takes place.

To determine the critical solution composition for passivity breakdown, a series of potentiokinetic polarization curves will be obtained in deaerated solutions with the appropriate crack-tip chemistry in which the pH is varied over a wide range. The values of the current density at the active peak will be plotted versus the pH (determined at the system temperature), and the solution with the pH value at which the current rises abruptly will be taken as the critical crevice solution. The current density, typically greater than ~10 μA/cm^2 or ~0.1 mm/y, is indicative of a significant crevice corrosion rate and the pH associated with this peak current is the critical pH for passivity breakdown. Thus, the measurement of I_{pass}, E_{corr}, and the composition of the critical crevice solution for different alloys provides a quantitative method of comparison for performance under crevice conditions, and allows a prediction of passivity breakdown as a function of flaw geometry and bulk water chemistry, which is of direct interest in SCC crack initiation.

II. TRANSIENT FUEL RESPONSE AND FISSION-PRODUCT RELEASE

Principal Investigator:
J. Rest

A. Introduction

A physically realistic description of fuel swelling and fission-gas release is needed to aid the prediction of the behavior of fuel rods and fission gases under certain hypothetical LWR accident conditions. To satisfy this need, a comprehensive computer-based model (the Steady-State and Transient Gas-Release and Swelling Subroutine, or GRASS-SST), its faster-running version (FASTGRASS), and correlations based on analyses performed with FASTGRASS (PARAGRASS) are being developed at ANL. This model is being incorporated into the Fuel-Rod Analysis Program (FRAP) code being developed by EG&G Idaho, Inc., at the Idaho National Engineering Laboratory.

The analytical effort is supported by a data base and correlations developed from characterization of irradiated LWR fuel and from out-of-reactor transient heating tests of irradiated commercial and experimental LWR fuel under a range of thermal conditions.

B. Modeling of Fuel/Fission-Product Behavior (J. Rest, S. R. Rajan, and F. A. Nichols)

1. Volatile Fission-Product Source Term Evaluation with the FASTGRASS Computer Code (J. Rest)

The accident that occurred at TMI-2 in March 1979 has underscored the necessity of understanding the behavior of volatile fission products (VFPs) in order to predict the radiological consequences of various nuclear reactor accident scenarios. In addition, fission-product (e.g., iodine) source term evaluation is required for the analysis and understanding of the so-called "stress-corrosion cracking" of nuclear reactor fuel cladding.

To date, the analysis of VFPs has utilized simple Booth-type diffusion models and has concentrated on conditions present in nuclear fuel rods during normal or steady-state irradiations. The relative success of this technique[19] (at low temperatures) can be attributed to the employment of "effective diffusion coefficients" that have been determined and utilized over a relatively small range of operating conditions, and the choice of an appropriate fuel surface-to-volume ratio for the determination of the surface area from which the fission products are released. Although the use of diffusion-type models to describe VFP release during normal, low-temperature fuel rod irradiations may be justified, the successful extension of such models to higher-temperature regimes and/or transient conditions is questionable in that these models ignore the chemical interactions between the various fission products, and the interaction between the VFPs and the noble fission-gas bubbles. In turn, the inappropriateness of describing the behavior of fission gases during transient conditions with models developed for steady-state operation has been demonstrated.[20]

As the noble gases play a major role in establishing the interconnection of escape routes from the interior to the exterior of the fuel, a realistic description of VFP release must a priori include a realistic description of fission-gas release and swelling. The steady-state and transient gas release and swelling subroutine, FASTGRASS, has been modified to include a mechanistic description of VFP (I, Cs, CsI, Cs_2MoO_4, and Cs_2UO_4) behavior. Phenomena modeled are the chemical reactions between the VFPs, VFP migration through the fuel, and VFP interaction with the noble gases. The initial phase of this work was supported by the Nuclear Safety Analysis Center. Work completed this quarter has focused on the completion of the initial phase of VFP modifications to FASTGRASS, the initiation of FASTGRASS VFP analysis verification (steady-state conditions), and calculations performed with FASTGRASS for the release of I, Cs and CsI from LWR fuel during severe core accident conditions.

The steady-state and transient mechanistic FASTGRASS computer code, for the prediction of the behavior of the noble fission gases, has been described previously.[20] Modifications for the inclusion of a mechanistic description of VFP behavior consisted of incorporating in the FASTGRASS fission-gas analysis the effective production rates of the relevant VFPs, the chemical interactions between the various VFPs, the interaction of the VFPs with the fission-gas bubbles, and the migration of the VFPs through the solid

UO_2 fuel. In the present treatment, only the VFPs I, Cs, and their major reaction products (CsI, Cs_2MoO_4 and Cs_2UO_4) have been included. The formation of Cs_2MoO_4 and Cs_2UO_4 can have a crucial effect on the reaction involving CsI, which is of major concern for deducing the form of iodine release in LWR power plant accident scenarios.[21]

Assuming local equilibrium and utilizing the law of mass action, the chemical reactions model, based on the work of S. W. Tam and C. E. Johnson,[22] leads to the following set of coupled nonlinear equations:

$$C_{Cs}^{T} = C_{Cs} + 2C_{Cs_2UO_4} + C_{CsI} + 2C_{Cs_2MoO_4} \ , \tag{6a}$$

$$C_{Cs}^{2}(1 - \beta - C_{Cs_2UO_4})\, P_{O_2} = \frac{1}{K_1}\, C_{Cs_2UO_4} \ , \tag{6b}$$

$$C_{Cs}(C_{I}^{T} - C_{CsI}) = \frac{1}{K_2}\, C_{CsI} \ , \tag{6c}$$

$$C_{Cs}^{2}(C_{Mo}^{T} - C_{Cs_2MoO_4})\, P_{O_2}^{2} = \frac{1}{K_3}\, C_{Cs_2MoO_4} \ , \tag{6d}$$

$$C_{Cs}^{T} = 0.1882\ \beta \ , \tag{6e}$$

$$C_{I}^{T} = 0.011\ \beta \ , \tag{6f}$$

$$C_{Mo}^{T} = 0.2348\ \beta , \tag{6g}$$

where

$$\beta = \dot{F}t/N_f^o, \tag{6h}$$

$$p_{O_2} = p_{O_2}(x, \beta, C_{Cs_2UO_4}, C_{Cs_2MoO_4}) \ . \tag{6i}$$

Here, C_i is the concentration of chemical species i; C_i^T is the total concentration of chemical species i that has been generated by fission at time t; p_{O_2} is the oxygen pressure; x is the initial stoichiometry; K_1, K_2, and K_3 are equilibrium constants for the reactions leading to the formation of Cs_2UO_4, CsI, and Cs_2MoO_4, respectively; β is the fractional burnup, related to the fissioning rate $\dot{F}$ per unit volume; N_f^o is the initial density of heavy-metal atoms in the fuel; and t is the irradiation time.

The chemical reactions model described by Eqs. (6a-i) is coupled to the FASTGRASS models for the migration of the VFPs through the fuel and for the interaction of the VFPs with the fission-gas bubbles. Elemental iodine is assumed to have the same diffusion coefficient as atomic xenon; the diffusion coefficient of atomic cesium is given by[23]

$$D_{Cs} = 8.53 \times 10^{-9} \exp(-6100/RT) \ cm^2/s, \tag{7}$$

where T is the absolute temperature and R is the gas constant. In addition, it is assumed that CsI is formed mainly near fission-gas bubbles and migrates through the fuel primarily within these gas bubbles. Cs_2UO_4 and Cs_2MoO_4 are assumed to be immobile.

The VFPs and the fission gases are generated via the fissioning of uranium within the UO_2 grains. The gases and VFPs then migrate to the grain faces and subsequently to the grain edges where they can be released to the exterior of the fuel if a network of long-range interconnected grain-edge porosity exists, and/or if grain boundary separation (microcracking) has occurred.[20]

Figure 21 shows FASTGRASS-predicted fractional release of iodine (^{131}I + ^{133}I) as a function of irradiation time, and compares these results with the data of Turnbull and Friskney.[24] To reflect the experimental uncertainty in temperature reported in Ref. 24, three predicted curves are given, corresponding to irradiation temperatures of 1733 ± 40 K . The circles ("I_{eff}") in Fig. 21 represent the fractional release of iodine (^{131}I + ^{133}I) calculated from the data by taking into account the respective fission yields of ^{131}I and ^{133}I. The FASTGRASS predictions of iodine release are in good agreement with the data. (It is interesting to note that FASTGRASS predicts that the majority of the iodine release occurred as CsI.)

Figure 22 shows FASTGRASS-predicted fractional release of stable xenon as a function of time, and compares it with the data for ^{133}Xe from Ref. 24. Again, the three predicted curves reflect the ±40 K uncertainty in irradiation temperature. The agreement between prediction and data is reasonable for the entire 27 weeks of irradiation. However, it should be noted that FASTGRASS currently calculates only the behavior of the stable fission gases, and the comparison between the predicted fractional release of total stable gases and the data for ^{133}Xe (5.25-day half-life) as shown in Fig. 22 may reflect the qualitative and quantitative differences in behavior between the total stable gases and ^{133}Xe. A comparison of Figs. 21 and 22 shows that the predicted fractional release of iodine (^{131}I + ^{133}I) qualitatively follows that of the stable fission gases. However, the fractional release behavior of ^{131}I, in contrast to the behavior of ^{133}I (and the sum of ^{131}I and ^{133}I), differs qualitatively from that of the noble gases, in agreement with the conclusions of Turnbull and Friskney reported in Ref. 24. Presumably, this effect is due to enhancement of ^{131}I release through grain-boundary diffusion.

Figure 23 and 24 show FASTGRASS predictions for Xe, I, Cs, and CsI (irradiated at 1400 K to 0.1 and 1.0 at. % burnup, respectively) during a transient heatup to ~2700 K at 0.1 K/s. The end-of-life results at 1400 K are in qualitative agreement with the observations reported by Appelhans and Turnbull[19] (i.e., the iodine release is similar to the noble gas release at relatively low temperatures).

The transient release predictions are also in qualitative agreement with the present authors' intuition: The cesium release is similar to the noble gas release, whereas the iodine release is substantially lower, with a greater percentage transient release of CsI than of elemental iodine from the higher-burnup fuel (Fig. 24). For the lower-burnup fuel, CsI and elemental iodine are predicted to show comparable transient release behavior (Fig. 23). It is interesting to note that if the temperature is subsequently increased to 3123 K and held there (e.g., for several hours), the fractional release of elemental iodine climbs dramatically while the CsI release fraction stays relatively constant (at the values shown at 2700 K in Figs. 23 and 24). This is presumably due, in part, to the dissociation of CsI at these temperatures.

2. Modeling of Grain-Boundary Separation during Thermal Transients

(S. R. Rajan, F. A. Nichols, and J. Rest)

A number of experiments have been performed to simulate accident transients in both thermal and fast reactors.[25-28] A wide spectrum of fuel response modes has been observed, ranging from very brittle to very ductile behavior.[29] The ductile mode is associated with the development of substantial intergranular porosity, while the brittle mode is characterized by rapid grain-boundary separation (or microcracking). Extensive grain-boundary separation or microcracking has been observed in irradiated LWR fuel subjected to thermal transients by means of a direct electrical heating (DEH) technique.[28] Such separation has also been observed in fuel tested in the PBF reactor in Idaho and in commercial fuel that had undergone a power excursion. Assuming a failure to scram, the geometry of fuel that exhibited a "ductile" response could remain intact well into the transient, leading to large-scale fission-gas swelling as temperatures approach melting, and possibly frothing as melting proceeds (due to the availability of fission gas on the boundaries). The "microcracking" mode could lead to quicker transient release of fission gas from the grain faces to the edges and from the edges to the fuel exterior, and could result in particulate dispersal of the fuel.

In this section, attention is directed towards the development and growth of round (r-type) voids on the grain boundary by grain-boundary diffusion. The microcracking model is used to predict the gas release and radial profiles of grain-boundary separation for several DEH tests.

a. Grain-Boundary Cavitation Models

Gas bubbles on a grain boundary acted upon by normal stresses can grow by a variety of mechanisms: vacancy diffusion, plastic deformation (or creep), or brittle cracking along the boundaries. Baluffi and Seigle[30] showed that vacancies could be produced at the grain boundary at a sufficient rate to allow cavity growth. Subsequently, in 1959, Hull and Rimmer[31] published their classic paper on cavity growth by grain-boundary diffusion driven by stress gradients normal to the boundary. The model has also been modified in various ways to account for boundary conditions[32,33] and for nonequilibrium shapes of growing cavities.[34,35]

The assumption that cavities retain their equilibrium shape may not always be valid. It has been observed in cavitation experiments that cavity heights grow in the initial part of the experiment, but stay constant in the latter part, with the cavities assuming flat, disklike "penny-shaped" configurations. This suggests a possible transition from a quasi-equilibrium lenticular growth mode to a nonequilibrium crack-like mode where the void elongates in the plane of the grain boundary under conditions such that surface diffusion cannot keep up with grain-boundary diffusion in retaining an equilibrium lens-shape.

Chuang and Rice treated the problem of a long, crack-like cavity growing at a fixed rate in a grain boundary.[34] Chuang et al. extended these results for nonequilibrium cavity shapes,[35] explicitly including the effects of stresses normal to the boundary.

The classical assumption for vacancy creation in the grain boundaries is one of uniform creation over the entire boundary. Conversely, the atoms leaving the cavity tip are assumed to plate out uniformly over the boundary, leading to a rigid-body translation of the grains. In many practical situations, however, the body undergoing creep cavitation deforms plastically, and the strain created by the plating out of atoms on the boundary near the tip can be accommodated by dislocation creep of the matrix farther away from the tip. Chen and Argon have proposed an analytical closed-form model[36] which not only combines diffusional and plastic flow effects, but also accounts for the nonequilibrium crack-like, elongated shapes of cavities. Their model, which couples the Beere-Speight diffusion-controlled equilibrium model[37] with the nonequilibrium cavity shape results of Chuang-Rice in a unique way, has been adopted as the basis for modeling the microstructural behavior in the present work.

b. Calibration and Verification

Initially, the DiMelfi-Deitrich model[29] was used in FASTGRASS to model grain-boundary separation.[38] In an attempt to improve this modeling capability, the Chen-Argon grain-boundary cavitation model was coupled to the FASTGRASS[39] and DEHTTD[28] codes; DEHTTD calculates the transient temperature history for irradiated LWR fuel subjected to simulated thermal transients by the DEH method. The coupled codes were then calibrated using the results of Test 33.[28]

Calibration consisted of adjusting four factors. The first factor accounts for the fact that a grain boundary may not be a perfect, inexhaustible source of vacancies. The actual growth rate of a void growing on a grain boundary by vacancy diffusion may be less than the rate predicted by a diffusion-controlled model that assumes such a perfect source. The second factor is the fractional value of the pore-solid surface area at which the degradation of thermal conductivity becomes significant. This reflects an idea borrowed from the percolation theory as applied to two-phase solids. The degree of interconnectedness of second-phase particles dispersed in a first phase increases sharply over a very narrow range around a critical concentration of the second-phase material. It was felt that a similar phenomenon could occur in the case of isolated pores on grain faces obstructing radial heat flow. A value in the range 0.25-0.3 seemed to fit the observed data, and a value of 0.25 was chosen. The other two factors are the proportionality constants relating the amount of degradation of thermal conductivity and the local microcracked grain-boundary area per unit volume.

Using this calibrated code, several other tests[28] were simulated. The key variables compared to observed values were the total fission gas released during the transient heating and the posttest radial profile of the pore-solid surface area. Table VII shows the predicted and observed values for some of the DEH tests. Figure 25 shows the radial profiles of separated grain-boundary area per unit volume for various tests. As seen in Fig. 25, the predicted radial profiles of microcracking agree (in magnitude though not in detailed shape) with observed values in the outer regions of the fuel, but are smaller than the values observed in the inner regions. Also, for Test 33 (Fig. 25d), melting occurred to a fractional radius of 0.2, whereas the centerline temperature predicted by the code is substantially below the melting point of 3120 K.

There are two limitations to this verification. First, though the Chen-Argon cavitation model accounts for the effects of the stress state of the matrix on grain-boundary separation, there was no capability of modeling the stress history of the fuel undergoing DEH testing. Hence, the code predictions do not reflect this interaction. Second, the use of a constant multiplier with the predicted cracking rate to arrive at the actual rate assumes that at all temperatures, the vacancy concentration is less than the equilibrium value by a fixed proportion. However, it is reasonable to expect that the efficiency of source/sink action will increase with temperature. The code underpredicts the microcracking in the inner hotter regions of the fuel; this means that the degradation of thermal conductivity in the inner regions due to grain-boundary separation will be underpredicted. Thus, it is expected that the temperatures predicted by the DEHTTD/FASTGRASS/Chen-Argon code will be lower than actual values. In Sec. c, preliminary results based on some new assumptions are outlined.

c. Improvements in the Assumptions

The equilibrium vacancy concentration is an Arrhenius function in temperature. In order to examine the grain-boundary efficiency in a more realistic fashion, the calibration factor relating the model's predicted void growth rate to the actual growth rate has been reformulated as

$$(\text{cracking rate})_{\text{actual}} = (\text{cracking rate})_{\text{model}} * \text{CALCR} * \exp\left(-\frac{E_{vf}}{KT}\right)$$

where CALCR = a calibration constant,

E_{vf} = energy of vacancy formation.

Some preliminary results using this assumption are shown in Fig. 26 for Test 33. The predicted and observed shapes show excellent agreement in shape as well as magnitude. There is no longer any underprediction in the inner fuel regions (compare with Fig. 25d). Also, the assumption of a sudden increase in the degradation of thermal conductivity at a critical value of grain-boundary areal coverage will be relaxed to allow a more gradual transition (i.e., an error function about a critical value).

It should be noted that even with this new assumption, the temperatures predicted by DEHTTD for Test 33 are substantially lower (by ~450 K) than the experimentally observed (centerline melting - 3120 K) temperatures. The reason for this is not understood at this time. However, the timing of model-predicted microcracking is critical to predicting the correct temperatures. If the degradation of thermal conductivity due to microcracking does not occur soon enough in the transient (i. e., the microcracking is underpredicted early in the transient), the predicted temperatures will be too low. Efforts are under way to reexamine the algorithms connecting the degradation of thermal conductivity to microcracking, as well as to improve the modeling of the temperature dependence of vacancy supply on the grain boundaries.

Table VII. Comparison of Observed and Predicted Transient Fission-Gas Release in DEH Tests

	Total Xe Release (%)	
Test No.	Observed	Predicted
22	13.1	8.03
24	12	11.9
27	33	27.8
32	16.1	13.5
33	40	38.5
37	5.9	8.72

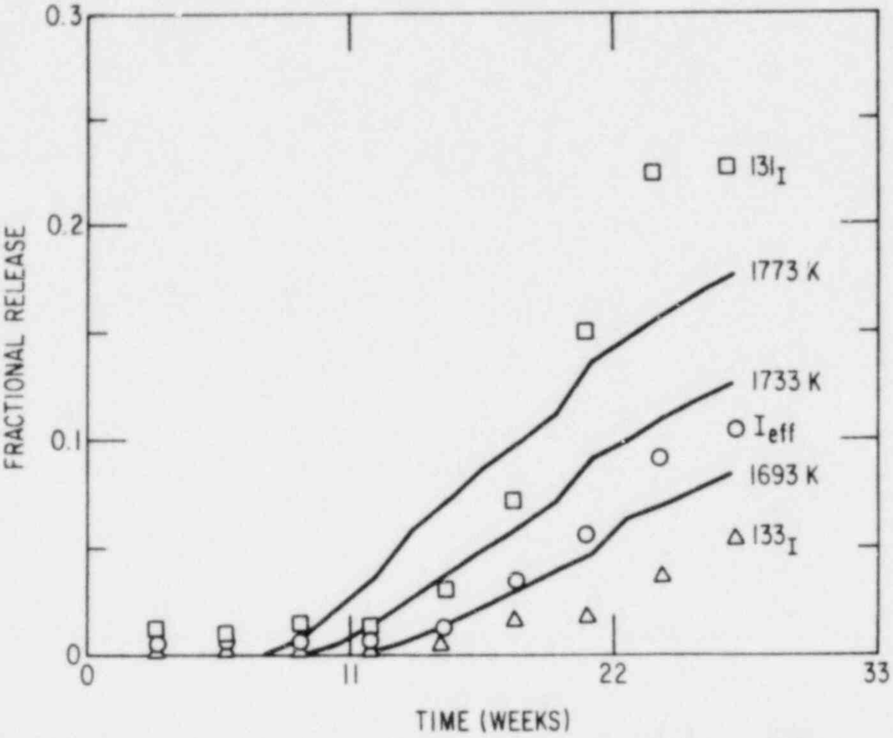

Fig. 21. FASTGRASS-predicted Fractional Release of ^{131}I + ^{133}I at 1733 ±40 K (Solid Curves), Compared with Data of Turnbull and Friskney[24] (Symbols).

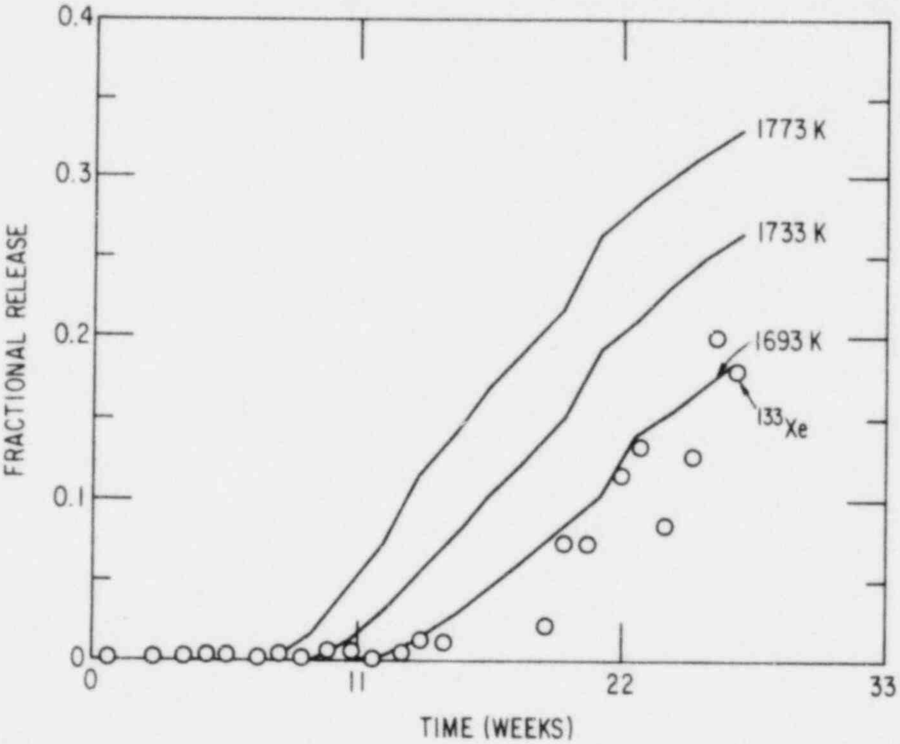

Fig. 22. FASTGRASS-predicted Fractional Release of Total Stable Xenon at 1733 ± 40 K (Solid Curves), Compared with Data of Turnbull and Friskney[24] (Symbols).

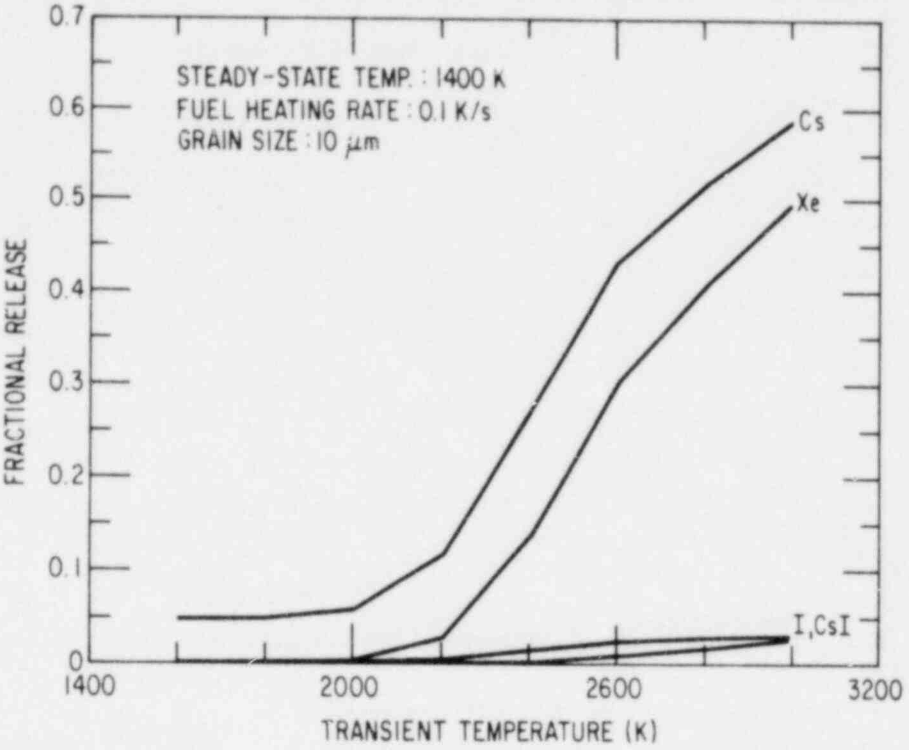

Fig. 23. FASTGRASS-predicted Transient Fission-Product Release at 0.1 atom % Burnup.

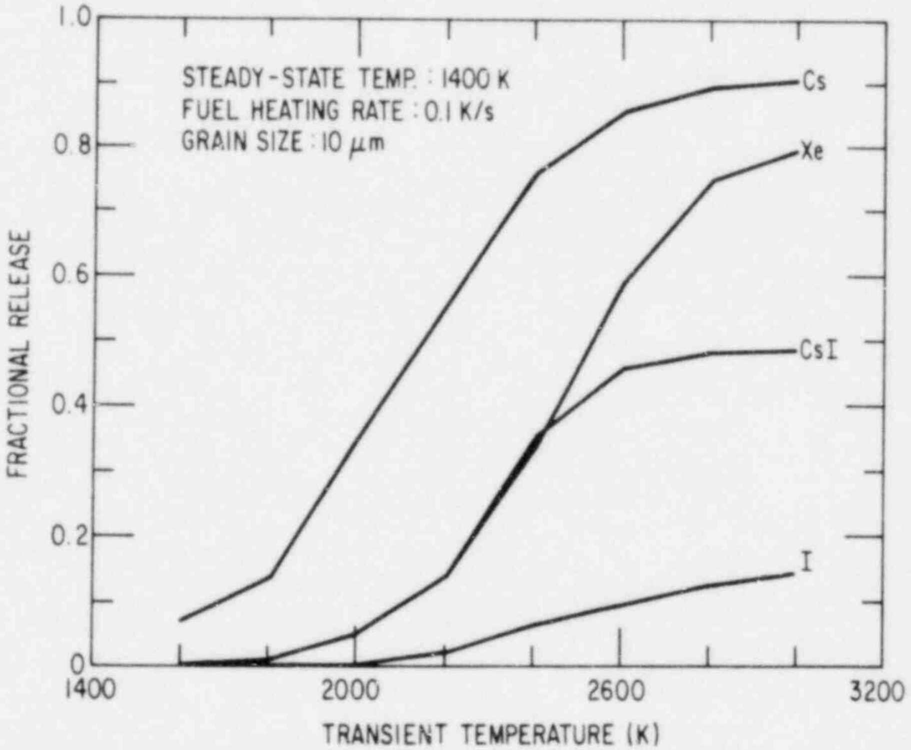

Fig. 24. FASTGRASS-predicted Transient Fission-Product Release at 1.0 atom % Burnup.

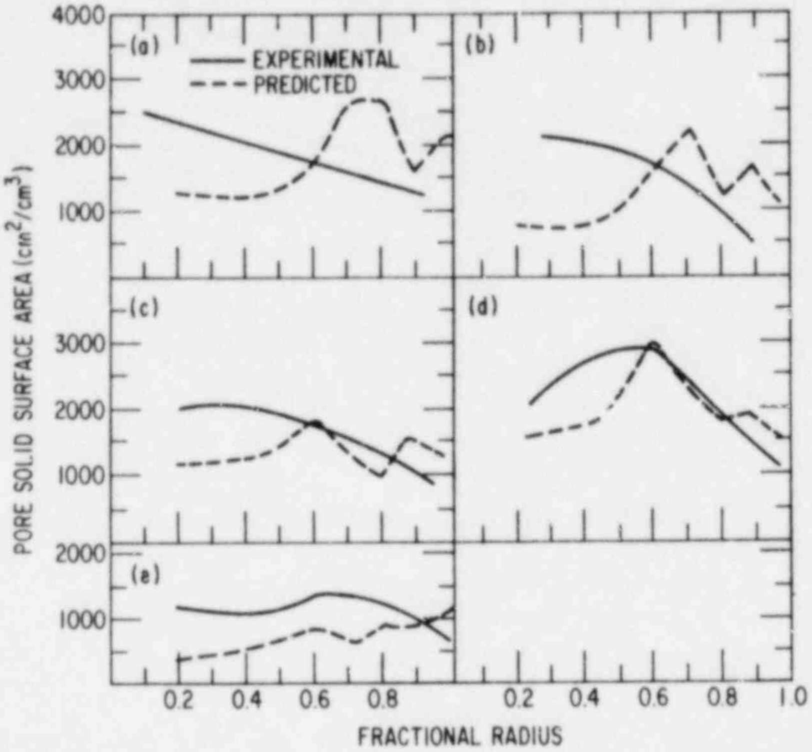

Fig. 25. Pore Solid Surface Area versus Fractional Radius for (a) Test 22, (b) Test 24, (c) Test 32, (d) Test 33, and (e) Test 37.

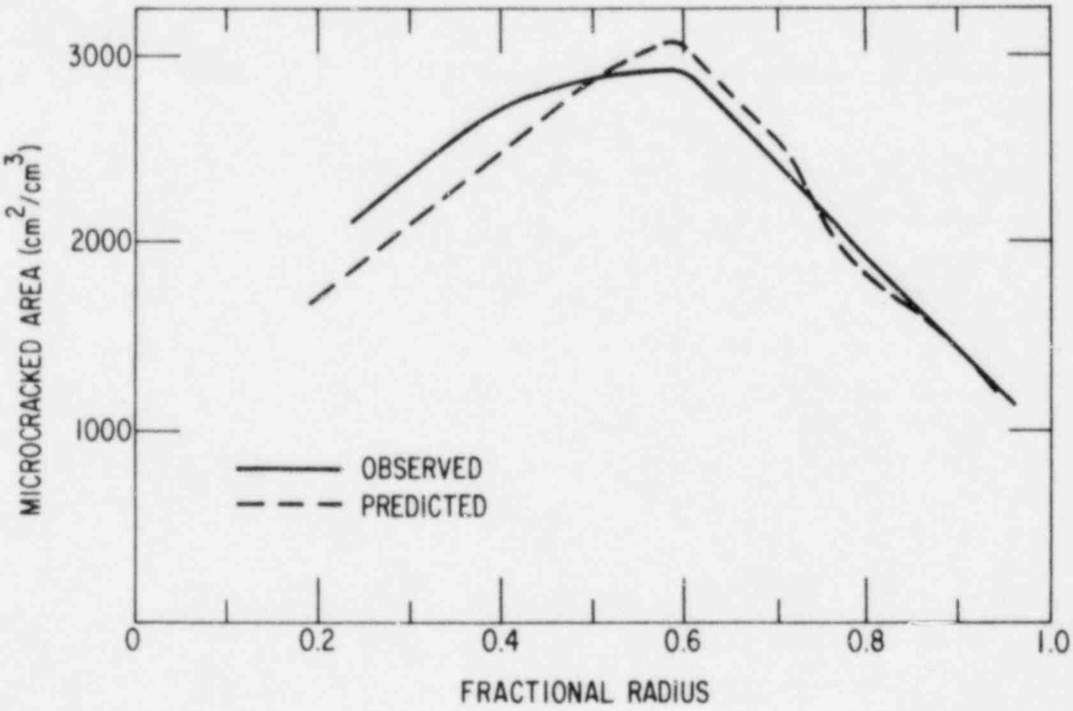

Fig. 26. Observed and Predicted Radial Microcracking Profiles for Test 33, Based on Assumptions in Section C.

III. CLAD PROPERTIES FOR CODE VERIFICATION

Principal Investigators:
H. M. Chung, F. L. Yaggee,
and T. F. Kassner

A. Introduction

The Zircaloy cladding of LWR fuel rods is susceptible to local breach-type failures during power transients after the fuel has achieved sufficient burnup to close the gap between the UO_2 fuel pellets and the cladding. High local stress imposed by differential thermal expansion of the fuel and cladding is the major factor in fuel-rod failure by the pellet-cladding interaction (PCI) mechanism, although volatile fission products (viz., I, Cs) at the inner surface of the fuel cladding may contribute to incipient crack formation via a stress-corrosion process.

In this program, the effect of temperature and strain rate on the deformation characteristics of irradiated Zircaloy fuel cladding is being investigated by means of internal gas-pressurization and mandrel-loading experiments in the absence of simulated fission-product species. The mechanical-property results will be used to develop a failure criterion for the cladding under PCI-type loading conditions. The information will be incorporated into fuel performance codes, which can be used to evaluate the susceptibility of extended-burnup fuel elements in commercial reactors to PCI failures during power transients in later cycles, and to evaluate cladding integrity in new fuel element designs.

B. Failure Characteristics of Big Rock Point Reactor Fuel Cladding after Stress-Rupture Testing (H. M. Chung)

This section reports results of microstructural examinations of the fuel claddings that were irradiated in the Big Rock Point Reactor and stress-rupture tested by internal gas pressurization. The test procedures and structural characteristics of the as-irradiated material have been reported previously.[40] Failure characteristics of specimens 165AE4A and 165AG10 (see Table VIII of Ref. 40), which failed in a ductile and a brittle manner, respectively, are reported in this section. The deformation and fracture characteristics of specimen 165AG10 are of particular interest because this specimen exhibited brittle-type failure in the absence of any fission-product species (e.g., I, Cs, Cd, or Te) in the test environment. Similar behavior has been observed previously for specimens 165AE4B (see Table VIII of Ref. 40) and 96 (see Table 4.4 of Ref. 41), both of which exhibited pinhole-type failures in the absence of iodine or other fission-product species.

In the present investigation, after the failure site was identified in each tube specimen, fracture characteristics were examined by SEM. Then, specimens obtained from near the fracture surface were examined by TEM and optical microscopy. Correlation of the results obtained with these complementary techniques, particularly the SEM and TEM observations, is an essential part of our effort to elucidate the mechanism of PCI-type brittle failure.

In the majority of previous investigations of the PCI phenomenon, optical microscopy and SEM were the primary techniques for microstructural characterization. Recently, Rosenbaum et al.[42] reported results of TEM examinations of Dresden-3 boiling-water reactor fuel claddings that were irradiated in service and subjected to power transients. Many of these claddings exhibited (1) numerous, large hydride stringers and (2) weak planar features attributed to dislocation channeling; both of these observations were related to the in-service deformation. The latter observation in the region of fuel rods affected by the power transients was considered as evidence that the PCI event produced plastic strains on a microscopic scale.[42]

1. Ductile Failure Characteristics

The rupture morphology of tube specimen 165AE4A indicated a ductile failure.[40] The failure region of the specimen was cut according to procedures outlined in Fig. 27, and several specimens for SEM, TEM, and optical microscopy examinations were obtained. The rupture region was split open at room temperature to reveal the fracture surfaces. SEM examination was conducted in an ETEC Corporation Autoscan Model.

a. SEM Evaluation

Figure 28A shows an overview of the outer surface and fracture surfaces of tube specimen 165AE4A. The true fracture surface "at temperature" (i.e., at 325°C) was considerably contaminated during the cooldown period following the rupture. The best high-magnification image that could be obtained is shown in Fig. 28B. Coalescence of microvoids, characteristic of a ductile failure, is evident from Fig. 28B. The fracture surface produced at room temperature during the splitting of the rupture region (Fig. 29) is clean and can be clearly differentiated from the "at-temperature" fracture surface. A comparison of Figs. 28B and 29 indicates that the material is more ductile at 25°C than at 325°C. This observation appears to be consistent with previously reported results[43,44] of uniaxial tensile tests of Zircaloys, in which a ductility minimum (with respect to temperature) was shown at ~400°C.

A higher magnification of the outer surface is shown in Fig. 30. Numerous cracks, generally parallel to the axial direction, are observable. The crud layer visible in Region A of Fig. 30 has spalled off the surface in some areas (e.g., Region B). Those regions reveal a higher density of axial cracks. A dispersive x-ray analysis of the crud layer showed traces of Fe, Cu, Al, Cr, P, Na, and Cl. Axial cracks similar to those in Fig. 30 were also observed at the inner surface, as shown in Fig. 31A. Some regions of the inner surface were relatively free of the cracks. Figure 31B shows circular inner-surface deposits, which have been reported to have a high uranium content.[41]

b. TEM Evaluation

Thin-foil TEM specimens were examined in either the JEOL Model CX-II STEM (100 keV) or the Kratos Model EM7 HVEM (1 MeV). Specimens from 165AE4A were characterized by (1) numerous dislocation tangles and cell structures that could not be observed in the as-irradiated material[40] and (2) a general absence of irradiation-induced defects.

The irradiation-induced defects in Zr alloys are known[45,46] to be annihilated by dislocation motions. As a result of the annihilation, the defects are usually observed in low-deformation regions, but not in dislocation channels or in high-deformation regions with dislocation tangles and cell structures. In light of this, the general absence of the irradiation-induced defects in the present test specimens, even in the low-deformation regions, was surprising. It appears that the deformation temperature (i.e., 325°C) was significantly higher than the in-service irradiation temperature; the consequence may have been the annihilation of a significant proportion of the defects through thermal (annealing) processes.

Typical contrasts from polycrystalline regions are shown in Fig. 32. Some dislocation networks are denoted with arrows. An area of high deformation containing dislocation tangles and cell structures is shown in Fig. 33. The observation of numerous dislocation tangles and cell structures is consistent with the coalescence of microvoids during fracture as indicated in the SEM fractographs, e.g., Fig. 28B.

The parallel contrasts denoted by the arrows in Fig. 33A indicate the operation of preferential slip on one slip system in the irradiated specimen. Preferential slip and associated dislocation structures in three different recrystallized subgrains are shown in Fig. 34. Similar observations have been reported for irradiated Zircaloy-2 and zirconium by Northwood et al.[46] and Kayano et al.,[47] respectively.

The dark parallel features shown in Figs. 34A and B should be differentiated from the parallel contrasts discussed in Ref. 40 (for the undeformed as-irradiated material), and from contrasts due to dislocation channels, as reported for irradiated Zr,[47,50] Zr-Nb alloys,[46,50] Zircaloy-2,[46,48-50] Zircaloy-4,[45] and spent fuel cladding[42] (Dresden-3 Reactor, Zircaloy-2). In the latter specimens, annihilation of irradiation defects by repeated dislocation motion in a localized band resulted in a light planar band free of irradiation-induced defects, seen against a dark background produced by a high concentration of irradiation-induced defects. The parallel contrasts of Figs. 34A and B should also be distinguished from the dark planar contrasts observed by some authors[42,47,49] against a light background of sparse irradiation defects. These dark bands, which appear to be narrower than the above-mentioned light bands, were also attributed to dislocation channels, although it is not clear how a dislocation channel could give rise to a dark contrast. The dark parallel contrasts of Figs. 34A and B are more linear than band-like, and appear to originate from dislocations associated with a preferential slip system.

Coleman et al.[45] reported that few dislocation channels were observed in cold-worked Zircaloy-4 compared to the number observed in annealed recrystallized material. They explained this on the basis of high back stress in the cold-worked material, caused by dislocation substructures that limit both the number of dislocations in motion and the distance they can move. This is consistent with the general absence of dislocation channels in the present specimen, and with the dislocation substructures it contains in the as-irradiated state. As reported previously,[40] the microstructure observed before a deformation test contained dislocation substructures that were not annihilated during the stress-relieving treatment. The apparent absence of dislocation channels is also consistent with the general absence of irradiation-induced defects, which we have suspected to be associated with the high deformation temperature relative to the irradiation temperature.

2. Brittle Failure Characteristics

The tight crack observed on the outer surface of specimen 165AG10 indicated a brittle-type failure. The failure region was cut according to procedures outlined in Fig. 35 for microstructural examinations by SEM, TEM, and optical microscopy. The tight crack was split open at room temperature to reveal the fracture surface "at temperature."

a. SEM Evaluation

Low-magnification scanning electron micrographs of the tight crack on the outer surface of specimen 165AG10 are shown in Fig. 36. The density of crack lines on the outer surface in this specimen was lower than in specimen 165AE4A (compare Figs. 30 and 36). Figure 36B shows a crud layer, ~0.06 mm thick, which has partially spalled off to reveal the cracks in the metallic cladding. The inner-surface crack morphology was similar to that shown in Fig. 31A.

Low-magnification fractographs of the through-wall crack in specimen 165AG10 are shown in Fig. 37. Figure 37B displays three different types of fracture surfaces, designated A, B, and C in the schematic of Fig. 37C. Region A is the true fracture surface produced at 325°C. Region B is an artifact fracture surface produced during the room-temperature splitting of the failure region. The morphology of the surface in this region is similar to that of Fig. 29 and characteristic of a ductile failure. Region C was also produced during the room-temperature splitting, which involved three-point bending of the curved piece of specimen containing the fracture surface (see Fig. 35). Near the end of the splitting, the two mating surfaces were forced to compress each other near the contact point of the knife edge. Therefore, Region C is not relevant to the fracture process operating at the test temperature.

The crack was apparently initiated at the outer surface and propagated in the direction shown by the arrow in Fig. 37B. The true fracture surface near the outer surface could be found near the step shown in Fig. 37A. The true surface shown in Fig. 38, obtained from the circled region in Fig. 37A, was protected from compression during the room-temperature split. The surface was somewhat corroded. Uncontaminated fracture surfaces, obtained from areas 2 and 3 of Fig. 37B, are shown in Figs. 39 and 40, respectively. In summary, fracture surfaces characteristic of crack nucleation, propagation, and termination are seen in Figs. 38-40, respectively.

The fractographs of Fig. 39 are characterized by pseudocleavage with limited areas of ductile fluting. This type of fracture surface, characteristic of the brittle-type failure of Zircaloy cladding, is usually referred to as a "cleavage plus fluting" or "flaky" fracture surface. From Fig. 39A, we can observe that the ridges associated with the fluting are approximately parallel to the direction of crack propagation, which is nearly parallel to the prism planes. No clear evidence of intergranular separation could be found from this fractographic examination.

The fracture surface morphology of Fig. 39 is strikingly similar to those reported for in-reactor PCI failures.[52-54] PCI fracture surface morphologies have been known to be influenced by the mechanical and thermal treatments of the cladding material, i.e., cold working, stress relieving, and annealing heat treatments. Most present-day commercial reactors utilize stress-relieved materials rather than recrystallized ones. In stress-relieved cladding, PCI fracture surfaces are dominated by transgranular pseudocleavages. Intergranular separation associated with PCI failures has been reported only in recrystallized materials containing grains of significant size.[55-57] The intergranular fracture in such cases is usually followed by transgranular cleavage plus fluting as the incipient crack propagates through the wall thickness. Fractographs of the transgranular part of the recrystallized material are somewhat different from those of Fig. 39 because of the equiaxed shapes of the grains.

b. TEM Evaluation

Several thin-foil specimens obtained from near the failure region (see Fig. 35) were extensively examined. TEM specimens of 165AG10 were characterized by (1) insignificant signs of dislocation activity, (2) a significantly smaller amount of residual irradiation-induced damage after the test than in the as-irradiated state,[40] and (3) a large quantity of unidentified precipitates.

At least two types of precipitates were observed in 165AG10. The precipitate morphologies and distributions were examined in conjunction with a selected area diffraction (SAD) technique. In contrast to the relatively large and very scarce precipitates observed in other TEM specimens (i.e., archive, as-irradiated, and 165AE4A), the precipitates found in 165AG10 specimens were extremely small and, in many cases, difficult to detect from bright-field reflections only. Diffraction patterns provided a better indication of the presence of precipitates.

Diffraction patterns of specimens other than 165AG10 were in most cases free of extra spots that indicate the presence of precipitates, and all the spots could be easily indexed based on Zr reciprocal lattices that were constructed on the basis of Table VIII. Such "clean" diffraction patterns were rare for 165AG10. Many regions revealed characteristic patterns that could not be indexed on the basis of α-Zr structure. The "clean" diffraction pattern from a single-phase matrix (e.g., alpha-phase Zircaloy) can be altered by the presence of second-phase precipitates in several ways: (1) appearance of extra pattern from the second phase itself, (2) modification of matrix spots because of the influence of the second-phase precipitates, (3) appearance of double-diffraction spots, (4) appearance of superlattice reflections associated with an ordered precipitate structure, and (5) modification of second-phase spots associated with finite crystallite size of very small precipitates.

A recrystallized subgrain from TEM specimen T2 of Fig. 35 is shown in the bright-field pictures of Figs. 41A and B. In Fig. 41B, one type of precipitate of roughly elliptical geometry can be observed. The precipitate particles are approximately 300-500 Å long and 20-60 Å thick. Mottled contrasts are observed within the precipitate itself (see Fig. 42A). These precipitates were designated Type A and are shown by A arrows. A second type of precipitate, designated Type B and shown by B arrows, can also be observed. Type B precipitates are characterized by diffuse, interconnecting, wave-like lines. Unlike Type A, the geometric shape of Type B cannot be defined clearly.

The SAD pattern corresponding to Fig. 41B is shown in Fig. 41C. The pattern consists of diffraction spots from at least three different phases, i.e., Zr and Type A and B precipitates. The Zr pattern could be indexed without difficulty. However, the patterns from the precipitates cannot be indexed at this time. A schematic diagram of Fig. 41C that illustrates the diffraction patterns produced by Zr and Type A and B precipitates is shown in Fig. 41D.

Numerous local regions of TEM specimens from 165AG10 showed dark contrasts that appeared to be an agglomeration of Type B precipitates. An example of such a region is shown in Fig. 42A. Type A precipitates are also visible in the figure, primarily at the lower left corner. Short dislocations, which were presumably immobilized by the Type B precipitates, can also be observed. The SAD pattern derived from Fig. 42A, illustrated in Fig. 42B, showed a predominant pattern of Type B precipitate and weak spots corresponding to the Type A precipitate. Figure 42C shows a dark-field image from the reflection marked by the arrow in Fig. 42B. Another region similar to that of Fig. 42 that contains an agglomeration of Type B precipitates is shown in Fig. 43. In this case, Type A precipitates are absent, and consequently, the SAD pattern is composed of spots corresponding to Type B precipitates only (Fig. 43C). The pattern is similar to the Zr $(10\bar{1}0)$ zone in appearance, with (0001) double-diffraction spots. However, systematic differences of ~2.2% between the interplanar spacings of the Zr pattern and those of the observed pattern could not be resolved. Because of the strong basal-pole texture of the commercial Zircaloy fuel cladding, the $(10\bar{1}0)$ zone (i.e., prism planes) is rarely observed in a TEM specimen in which the foil plane is nearly perpendicular to the radial direction. On the basis of numerous observations of precipitates in several thin-foil specimens of 165AG10, as exemplified by Figs. 41-43, it appears that the brittle-type failure is associated either with the precipitates themselves or with the process responsible for the precipitation.

3. Summary

Zircaloy cladding specimens, obtained from Big Rock Point Reactor spent fuel assemblies and deformed to fracture at 325°C under internal pressurization, were examined via SEM and TEM to establish the fracture characteristics. Numerous dislocation tangles, cell structures, and areas of preferential slip were observed by TEM in cladding specimens that failed in a ductile manner. This observation was consistent with SEM fractographs that indicated a moderate extent of microvoid coalescence. SEM fractographs obtained from specimens that failed in a brittle manner in the absence of fission-product species in the test environment were characterized by transgranular pseudocleavage plus fluting, and are surprisingly similar to those reported for in-reactor PCI-type failures. An evaluation of TEM specimens from cladding that failed in a brittle manner revealed numerous regions containing dispersed unidentified precipitates or agglomerations of extremely fine precipitates, primarily in the cell-wall regions of the stress-relieved material. The brittle failure appears to be strongly associated with the precipitates, which cannot be identified at this time.

Table VIII. Interplanar Spacings and Reciprocal Lattice Vectors of Zr[a] Used to Index Zircaloy Diffraction Patterns[b]

h k ℓ	$h^2 + hk + k^2$	ℓ^2	$d_{hk\ell}$(Å)$^{(c)}$	$H_{hk\ell}$(Å^{-1})$^{(d)}$	$H_{hk\ell}/H_{100}$
1 0 0 1 $\bar{1}$ 0	1	0	2.795	0.358	1.000
0 0 2	0	4	2.570	0.389	1.088
1 0 1 1 $\bar{1}$ 1	1	1	2.461	0.406	1.135
1 $\bar{1}$ 2 0 1 2	1	4	1.896	0.527	1.472
1 1 0 1 $\bar{2}$ 0	3	0	1.617	0.619	1.731
1 0 3 1 $\bar{1}$ 3	1	9	1.464	0.683	1.910
1 1 2	3	4	1.369	0.731	2.042
2 0 1 2 $\bar{2}$ 1	4	1	1.351	0.740	2.068
1 0 4	1	16	1.171	0.854	2.386
2 0 3	4	9	1.085	0.922	2.576
2 1 0 3 $\bar{2}$ 0	7	0	1.056	0.947	2.649
2 1 1 3 $\bar{2}$ 1	7	1	1.037	0.965	2.698
1 1 4	3	16	1.007	0.993	2.776
2 1 2 3 $\bar{2}$ 2	7	4	0.979	1.021	2.852

[a] Based on lattice constants $A_o = 3.227$ Å and $C_o = 5.157$ Å.

[b] Reflections with zero structure factor but possible under a double-diffraction condition were excluded. Structure factor is zero if ℓ is odd and $h + 2k = 3n$ $(n = 0, 1, 2 \ldots)$.

[c] Interplanar spacing of (h k ℓ) plane.

[d] Length of the reciprocal lattice point of (h k ℓ) plane.

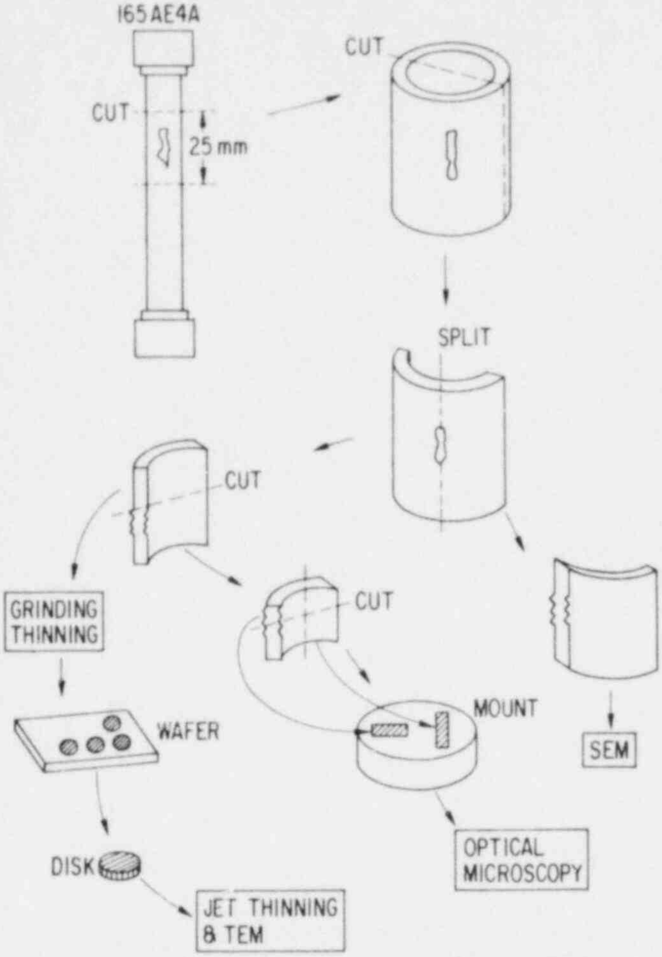

Fig. 27.

Schematic of Procedures Used to Obtain SEM, TEM, and Optical Microscopy Specimens from Big Rock Point Reactor Spent Fuel Cladding Tube 165AE4A, Which Failed in a Ductile Manner after Internal Gas Pressurization at 325°C.

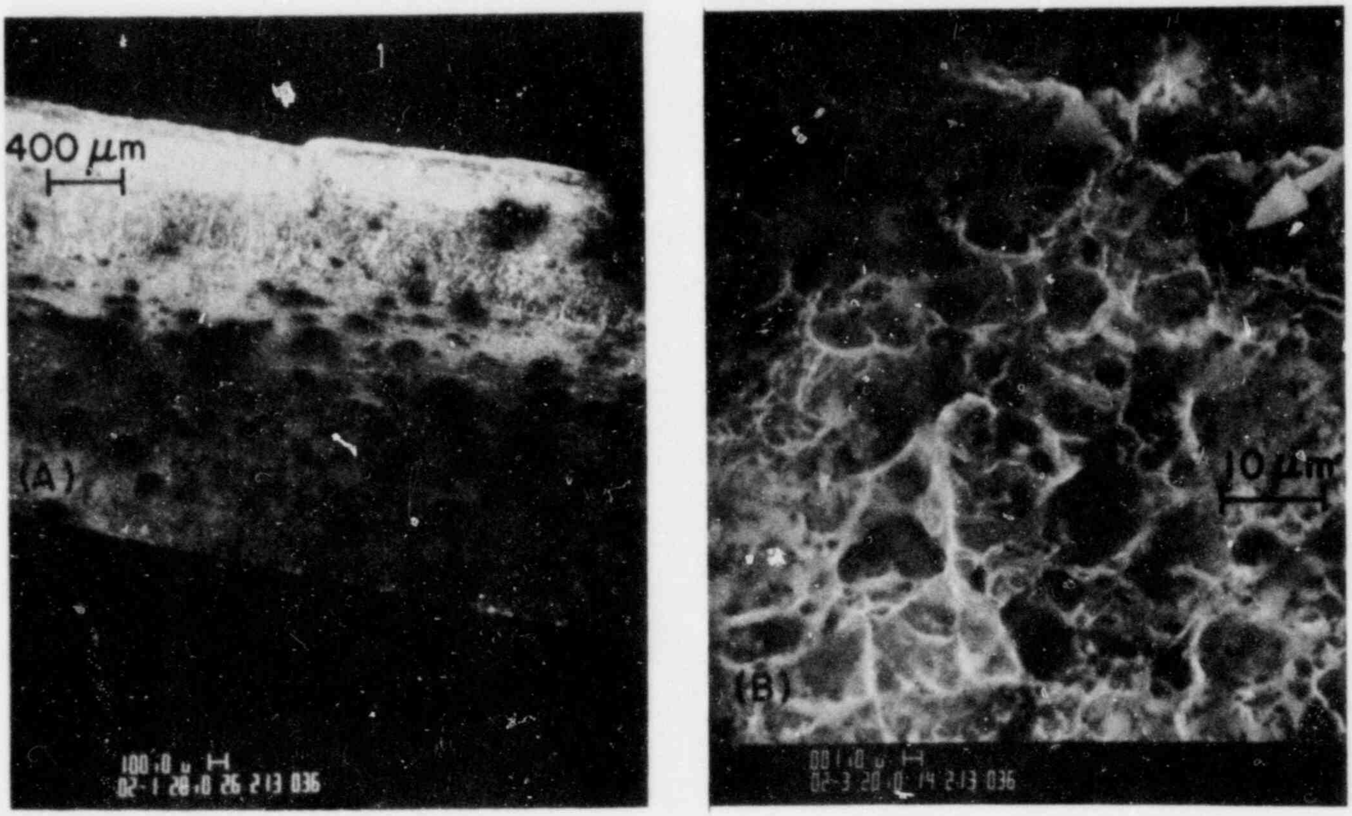

Fig. 28. Scanning Electron Micrographs of Big Rock Point Reactor Spent Fuel Cladding Tube 165AE4A, Which Failed in a Ductile Manner. (A) Overview of outer surface and fracture surface; (B) detail of fracture surface morphology.

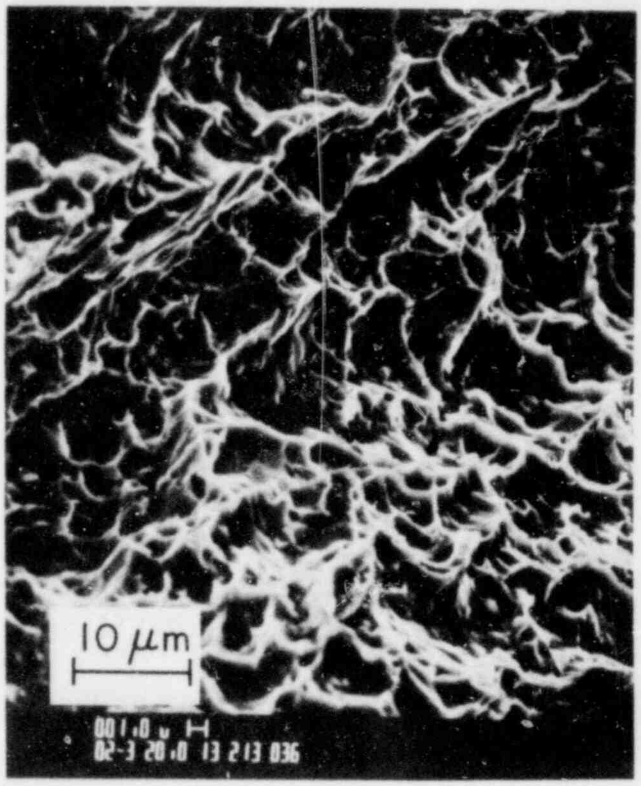

Fig. 29.

Scanning Electron Micrograph of Room-Temperature Fracture Surface of Spent Fuel Cladding Tube 165AE4A. This surface shows more ductile characteristics than the fracture surface produced at 325°C (Fig. 28B).

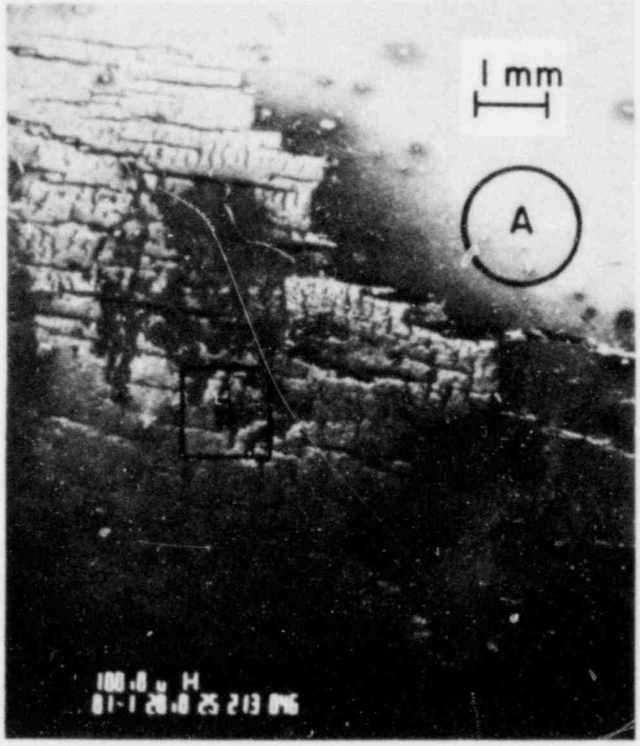

Fig. 30.

Scanning Electron Micrograph Showing Crack Morphology on Outer Surface of Spent Fuel Cladding Tube 165AE4A. Cracks are generally parallel to the tube axial direction. Crud layer has spalled in Region B, but is intact in Region A.

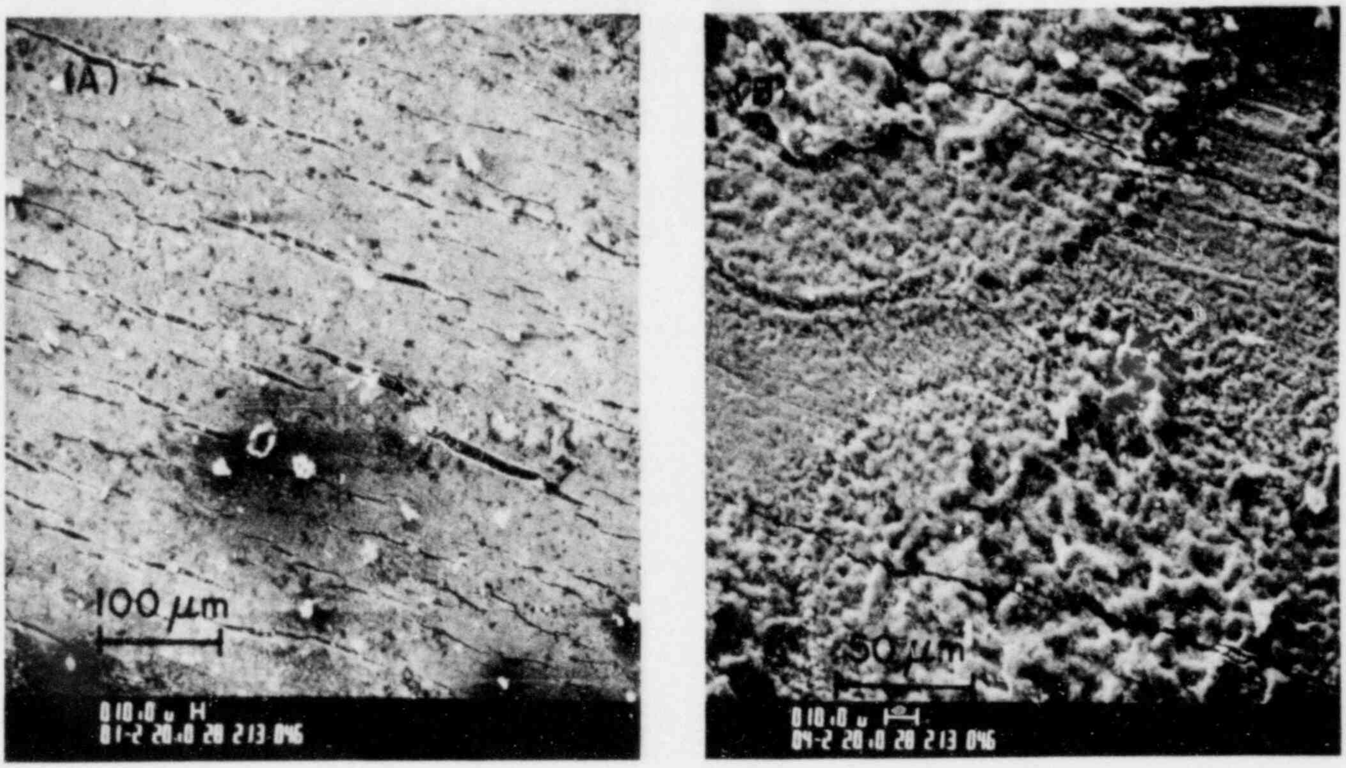

Fig. 31. Scanning Electron Micrographs of Inner Surface of Spent Fuel Cladding Tube 165AE4A, Showing (A) Crack Morphology and (B) Circular Uranium-rich Deposits.

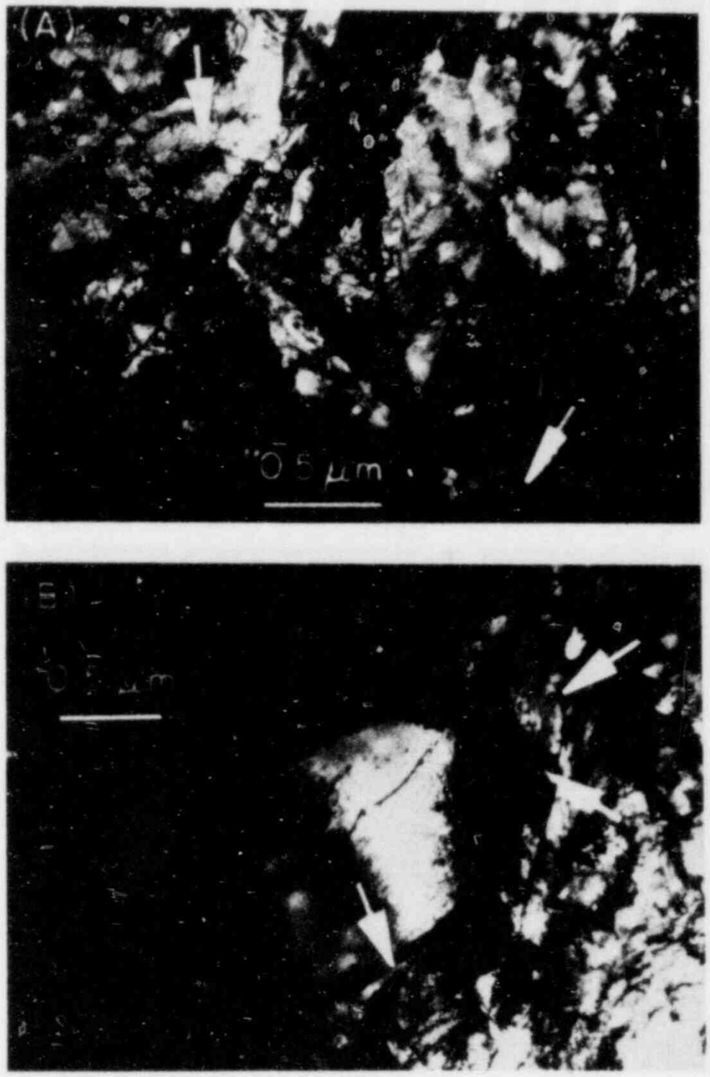

Fig. 32. Transmission Electron Micrographs of Spent Fuel Cladding Tube 165AE4A, Showing Dislocation Networks (Arrows) in (A) the Unrecrystallized Region and (B) the Region Surrounding a Recrystallized Subgrain.

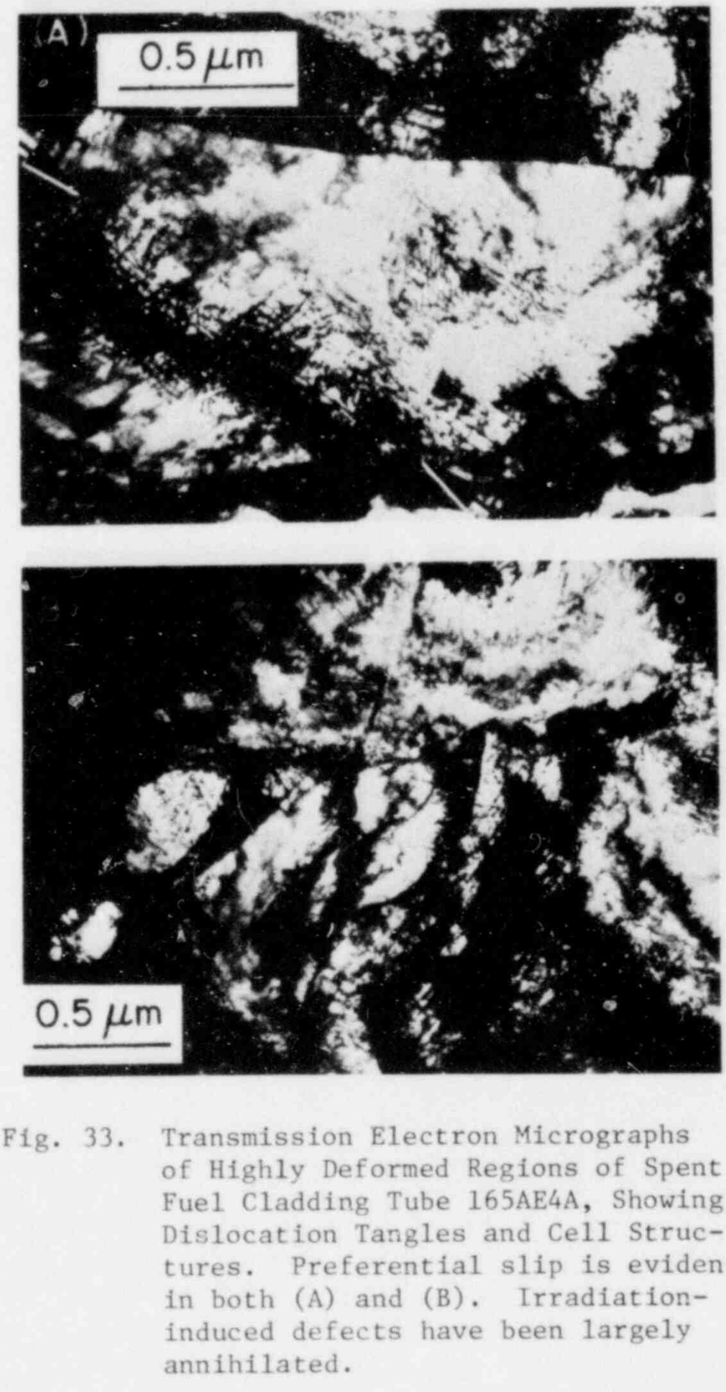

Fig. 33. Transmission Electron Micrographs of Highly Deformed Regions of Spent Fuel Cladding Tube 165AE4A, Showing Dislocation Tangles and Cell Structures. Preferential slip is evident in both (A) and (B). Irradiation-induced defects have been largely annihilated.

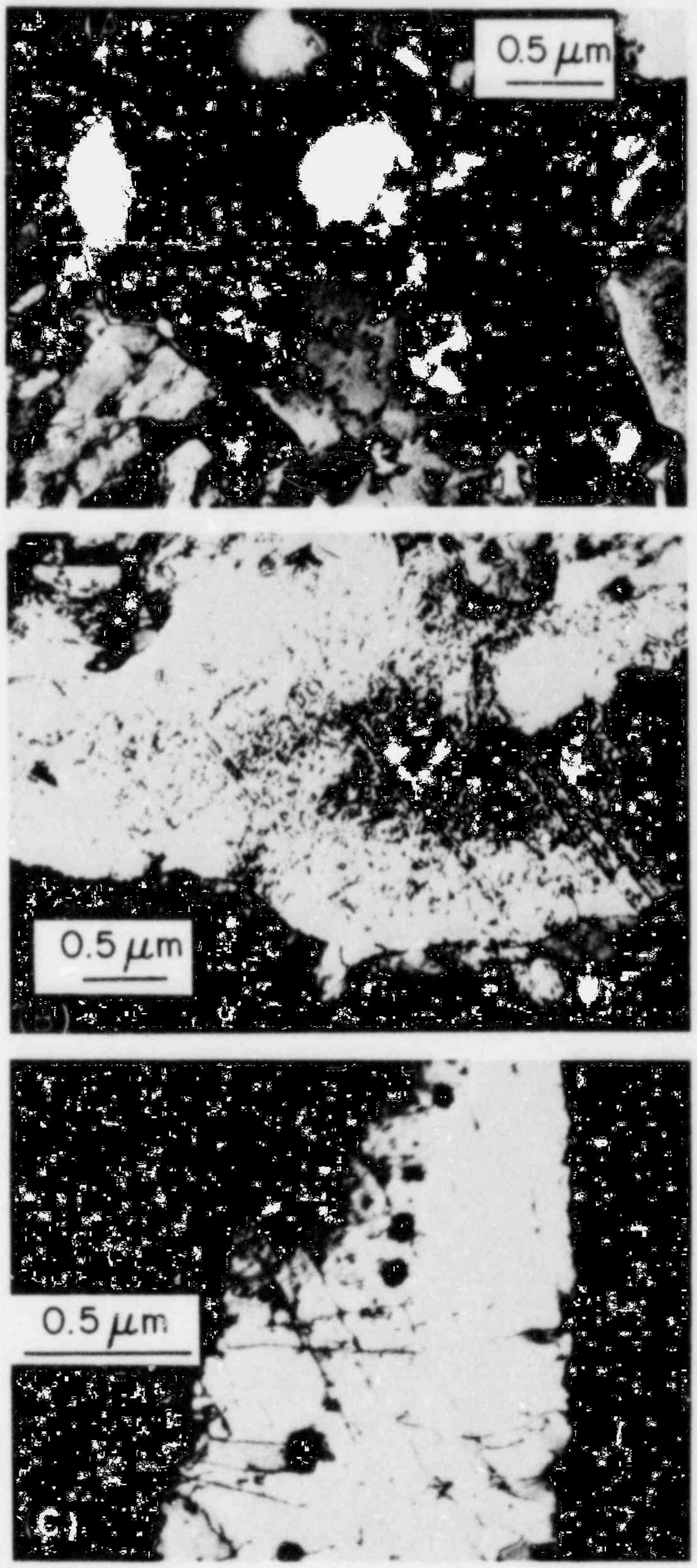

Fig. 34. Preferential Slip and Associated Dislocation Structures Observed in Three Different Recrystallized Subgrains of Spent Fuel Cladding Tube 165AE4A.

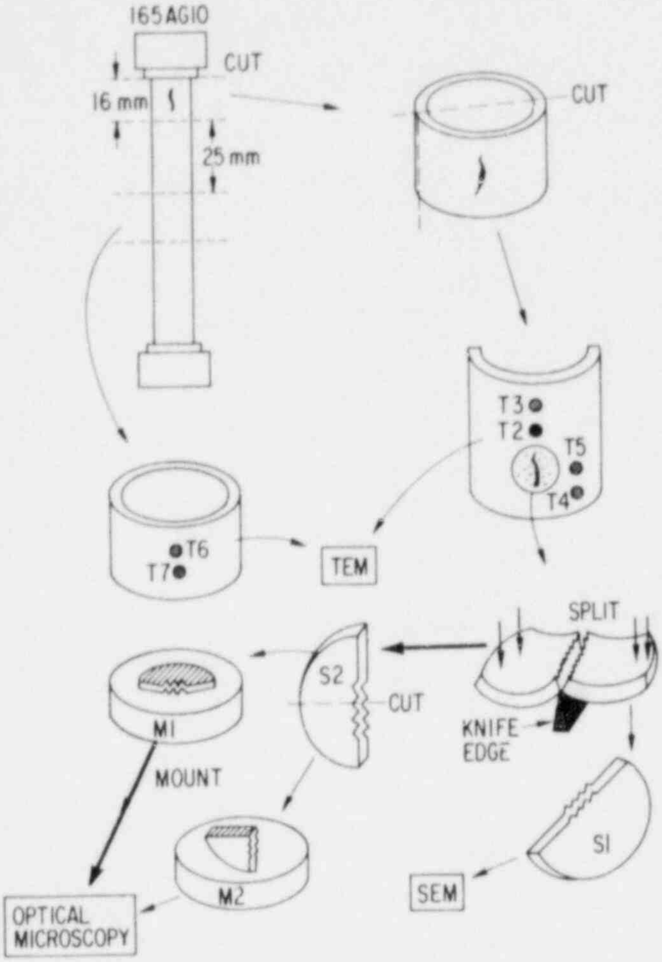

Fig. 35.

Schematic of Procedures Used to Obtain SEM, TEM, and Optical Microscopy Specimens from Big Rock Point Reactor Spent Fuel Cladding Tube 165AG10, Which Failed in a Brittle Manner after Internal Gas Pressurization at 325°C.

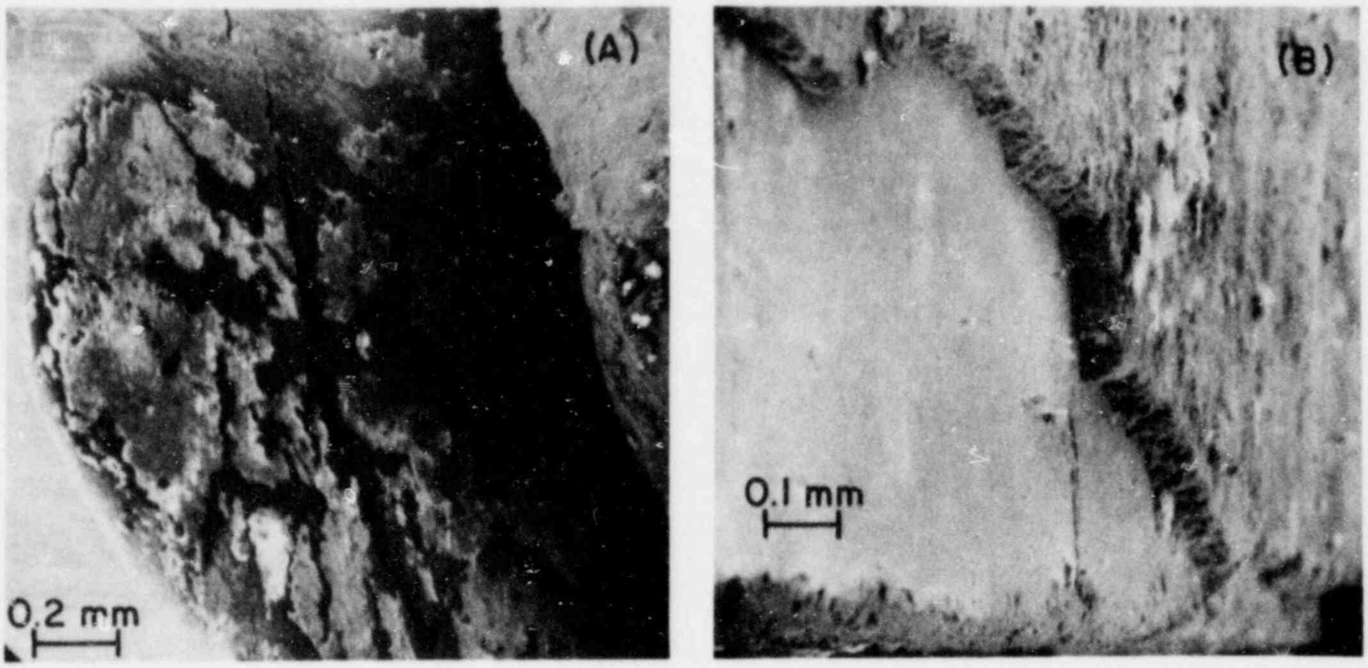

Fig. 36. Scanning Electron Micrographs of the Outer Surface of Spent Fuel Cladding Tube 165AG10 (Specimen S1 of Fig. 35), Which Failed in a Brittle Manner at 325°C. (A) Axial crack next to through-wall fracture surface; (B) crack revealed underneath crud layer.

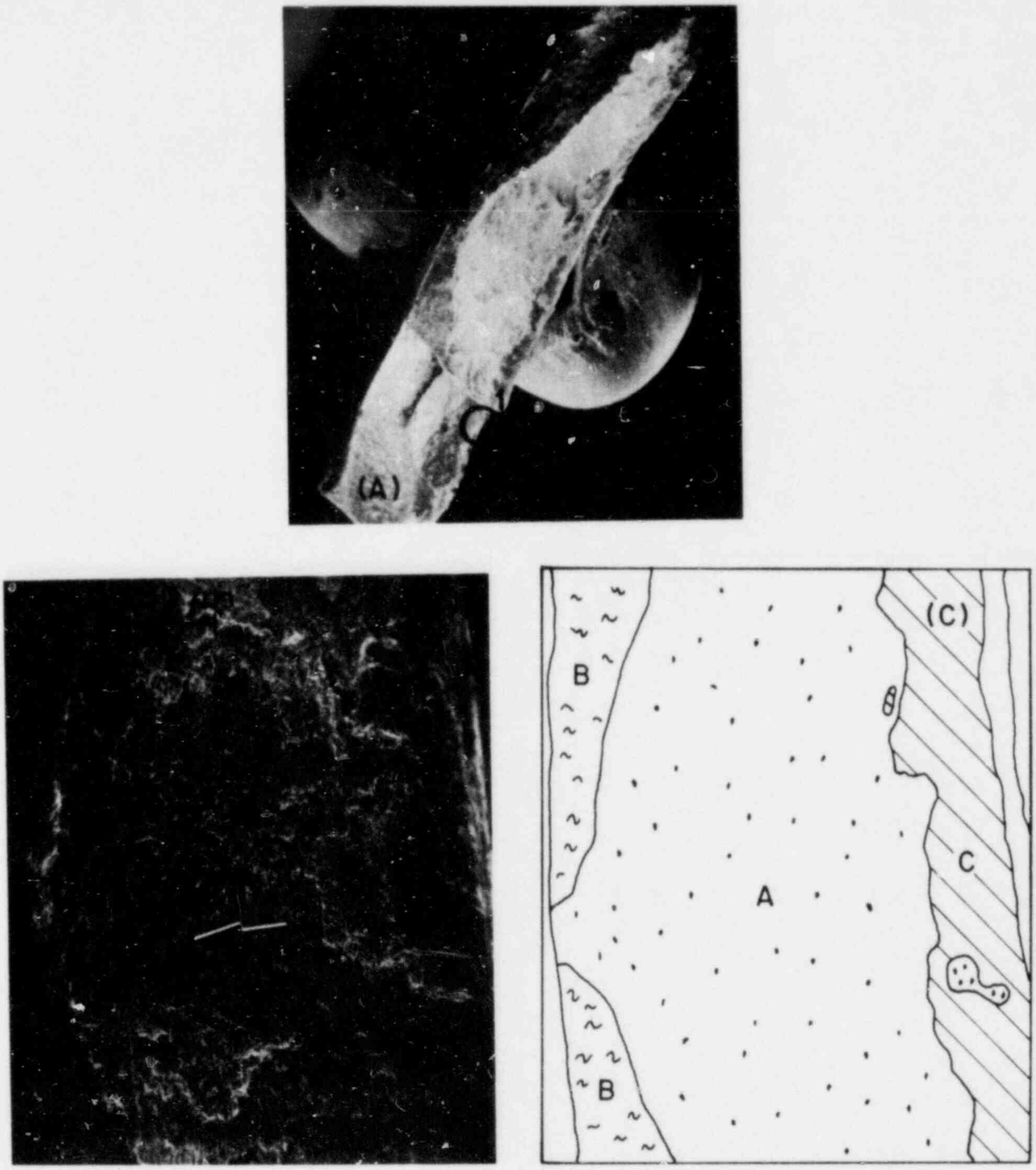

Fig. 37. Low-Magnification Fractographs of Through-Wall Crack in Spent Fuel Cladding Tube 165AG10 (Specimen S1 of Fig. 35). (A) Overview of fracture surface; (B) enlarged view of the middle section of (A); (C) schematic of (B), showing the three different fracture-surface types observed (see text); (D) enlarged view of (B) obtained from composite photos of the fracture surface. Arrow in (B) denotes approximate direction of crack propagation, i.e., from outer to inner surface. The fracture surface types identified from left to right in (C) appear in the same sequence in (D).

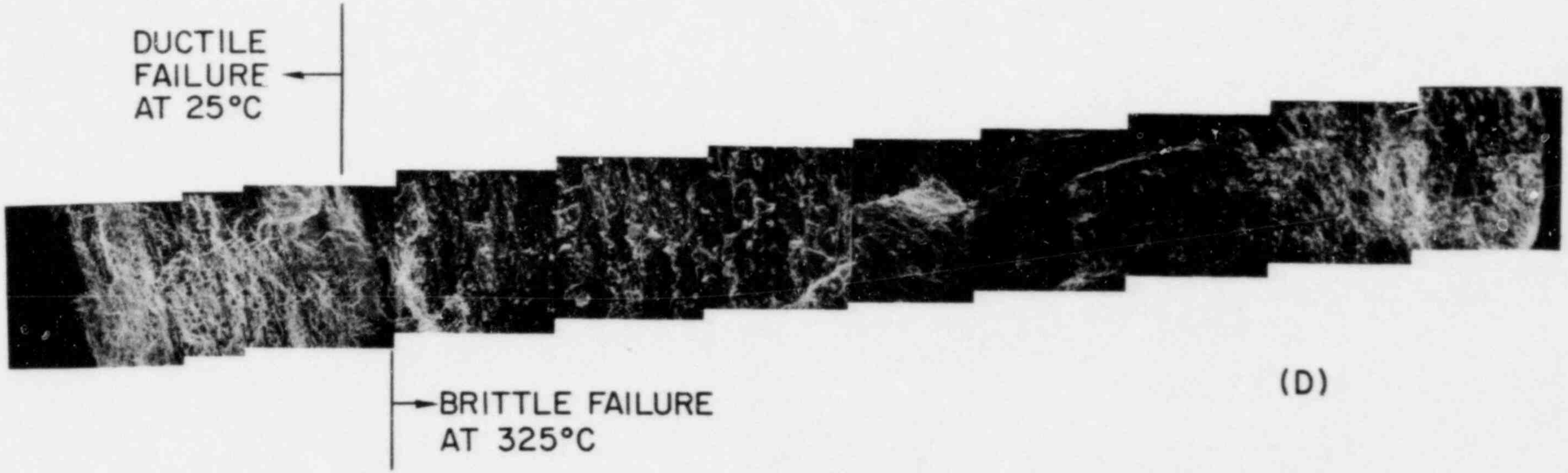

Fig. 37. (Contd.)

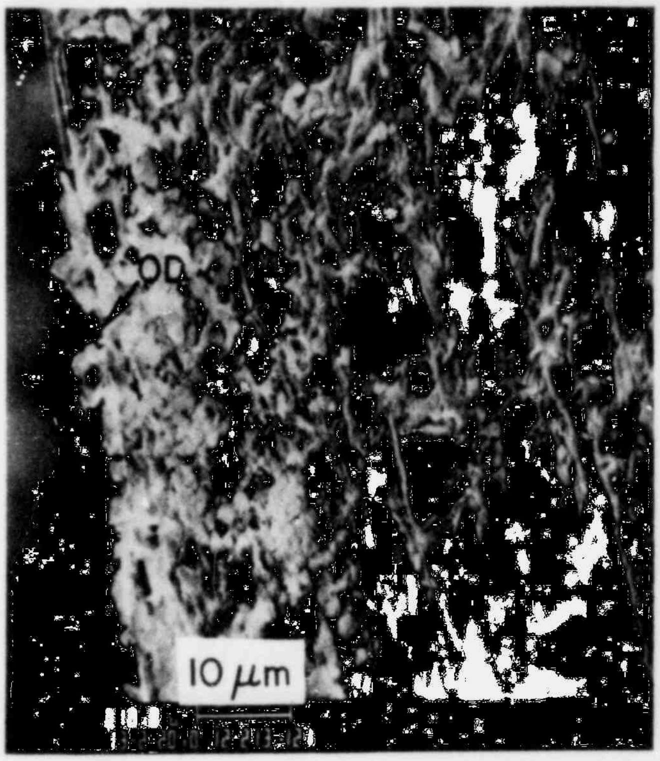

Fig. 38. Fracture Surface Morphology at the Initiation Location of the Through-Wall Crack in Spent Fuel Cladding Tube 165AG10, Which Failed in a Brittle Manner at 325°C. The fractograph was obtained from Region 1 of Fig. 37A.

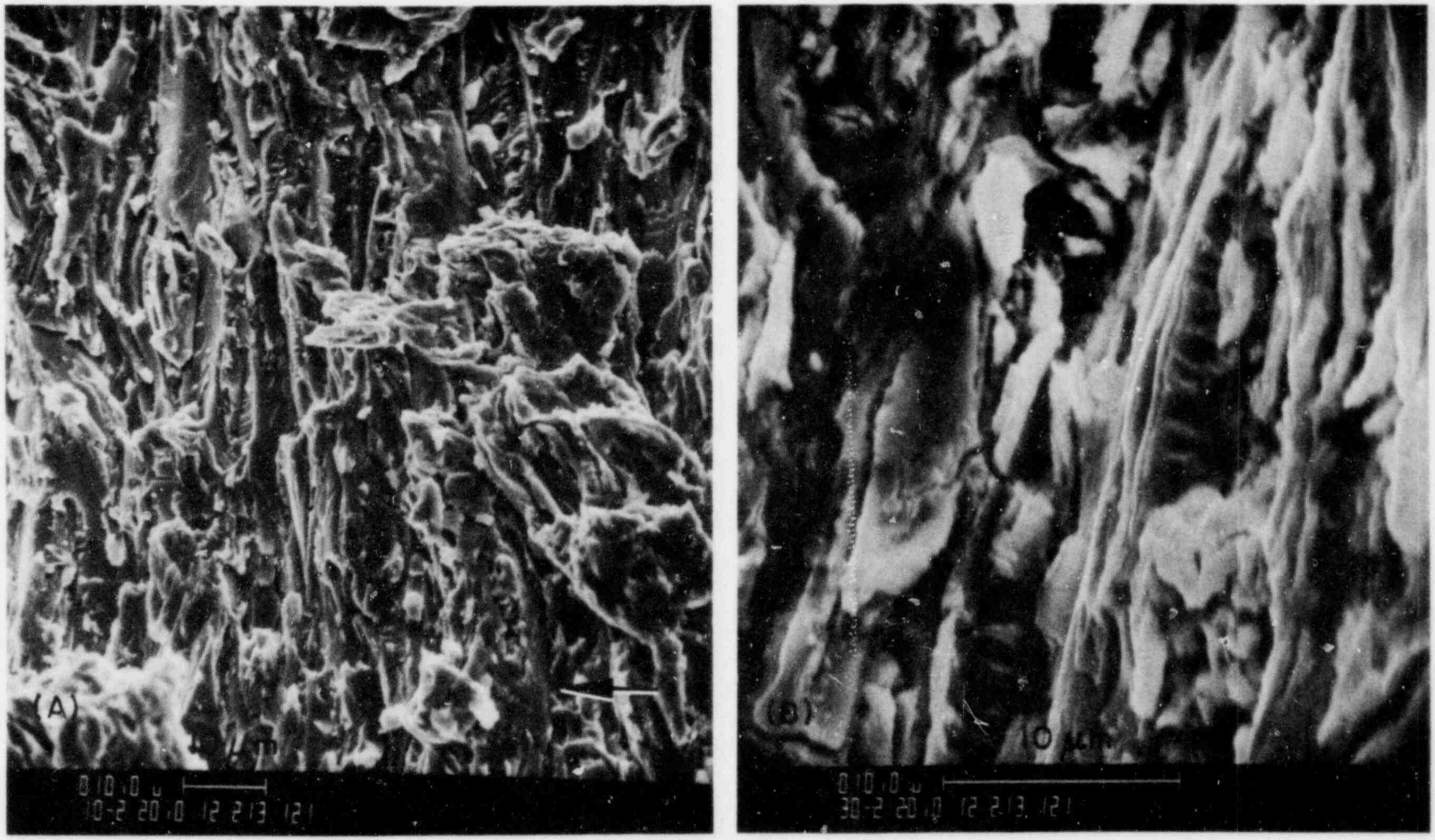

Fig. 39. Brittle-Type Fracture Surface Morphologies of the Through-Wall Crack in Spent Fuel Cladding Tube 165AG10. (A) was obtained from Region 2 of Fig. 37B; (B) is a higher magnification of a similar region. Arrow in (A) denotes approximate direction of crack propagation. Typical PCI-type fracture characteristics (transgranular pseudocleavage and fluting) are seen in both (A) and (B).

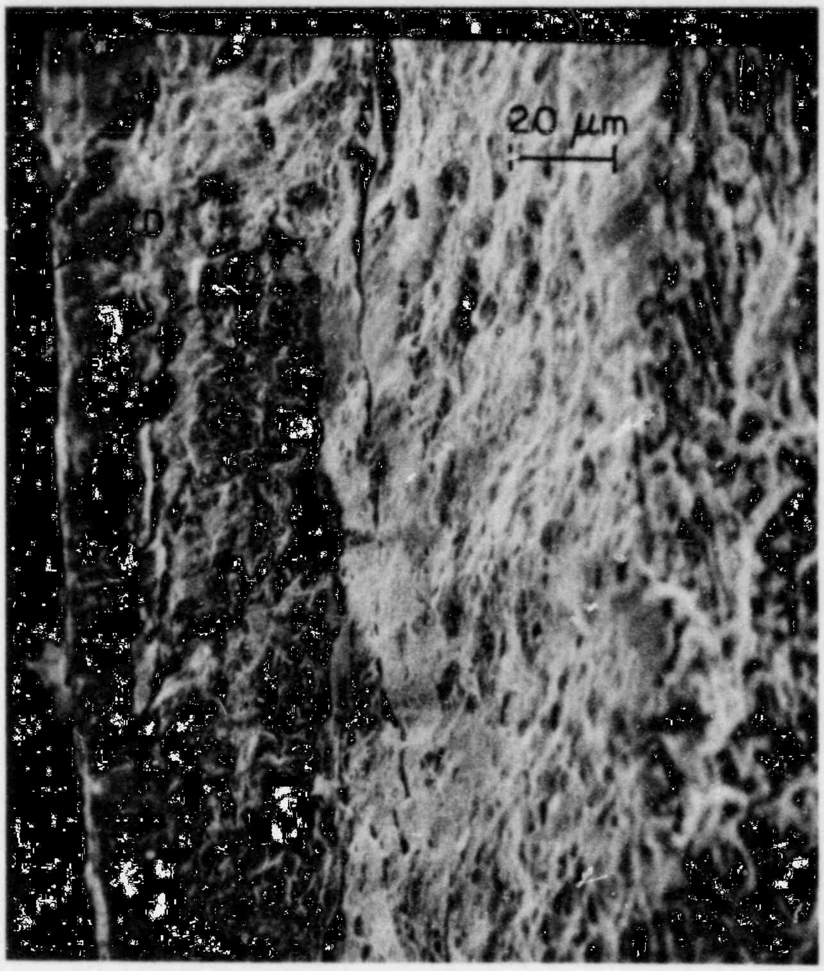

Fig. 40. Fracture Surface Morphology Near the Crack Termination Point of the Through-Wall Crack in Spent Fuel Cladding Tube 165AG10. The fractograph was obtained from Region 3 of Fig. 37B.

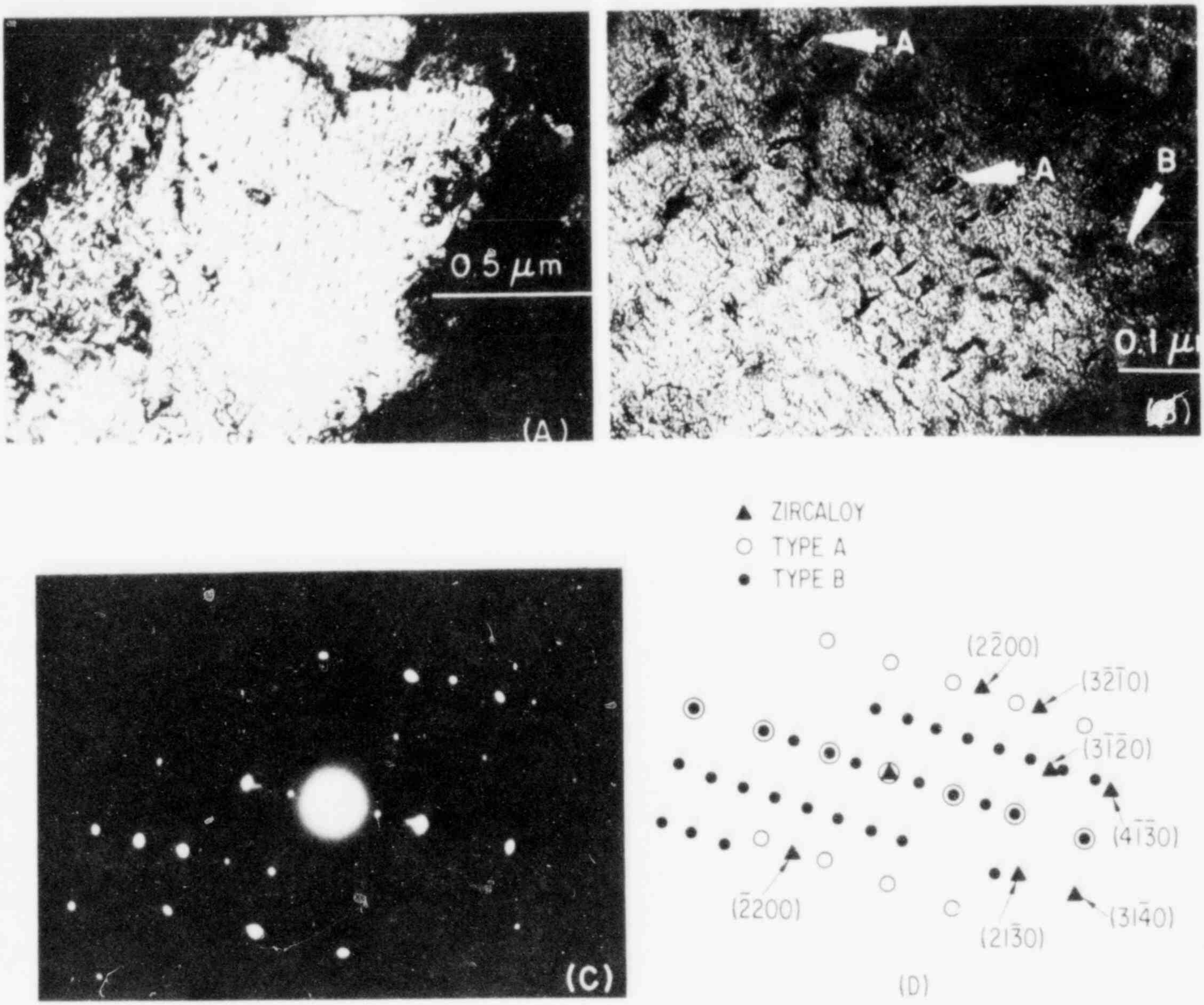

Fig. 41. Transmission Electron Micrographs of a Recrystallized Subgrain from Spent Fuel Cladding Tube 165AG10 (Specimen T2 of Fig. 35) That Contains Unidentified Precipitates. (A) Overview of the subgrain; (B) high magnification of (A), with two types of precipitates denoted by arrows A and B (see text for explanation); (C) selected area diffraction pattern of (B); (D) schematic of diffraction spots from (C), with Zircaloy spots indexed.

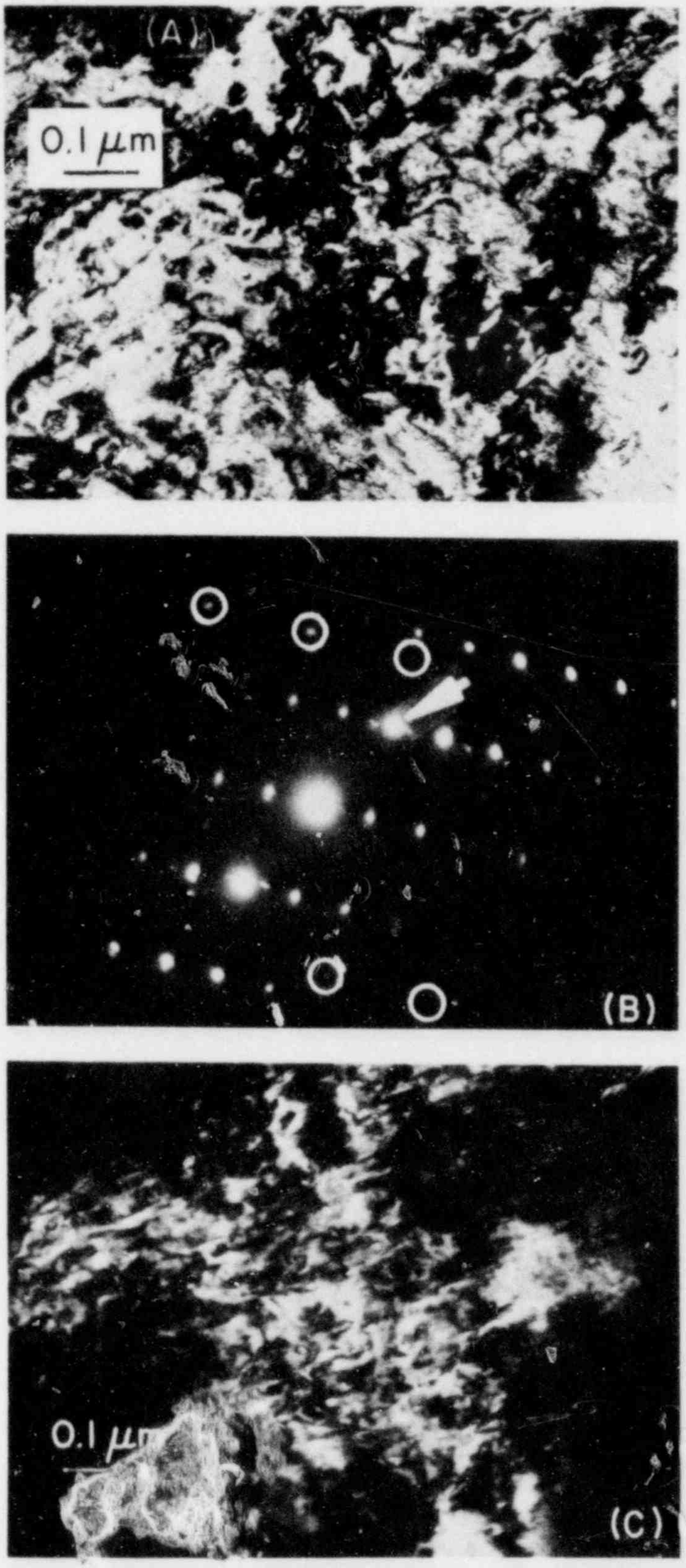

Fig. 42. Transmission Electron Micrographs Obtained from Near the Fracture Region of Spent Fuel Cladding Tube 165AG10 (Specimen T2 of Fig. 35). (A) Bright-field images of the two types of precipitates described in Fig. 41; (B) selected area diffraction pattern of (A); (C) dark-field image corresponding to the spot denoted by arrow in (B).

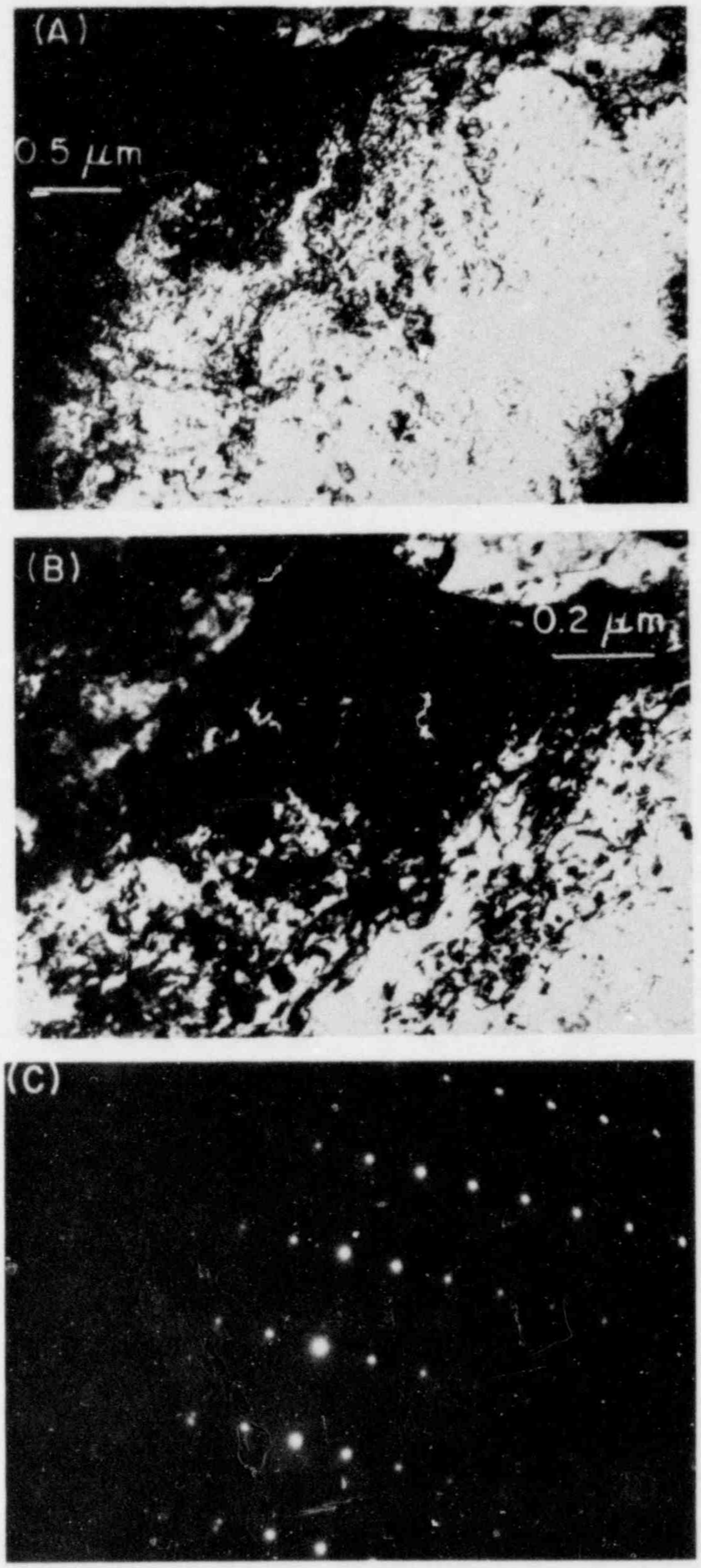

Fig. 43. Transmission Electron Micrographs of a Recrystallized Subgrain from Near the Fracture Region of Spent Fuel Cladding Tube 165AG10 (Specimen T2 of Fig. 35). (A) Agglomeration of dark precipitates; (B) high magnification of (A); (C) selected area diffraction pattern of (B).

C. Internal Mandrel Loading Experiments on Irradiated Zircaloy Fuel Cladding
(F. L. Yaggee)

Current progress on the mandrel (mechanical) loading of irradiated Zircaloy fuel cladding includes an initial calibration of eight mandrels and results of five preliminary tests on unirradiated Zircaloy cladding using mandrel loading. The preliminary tests were conducted at ambient temperature (~25°C) on Zircaloy tubes that were oxidized at high temperature to produce low-ductility material.

The components of each mandrel consist of a tapered pin (arbor) and an expandable sleeve with an internal taper that matches the taper of the arbor. Both components are made of hardened (tool) steel and have smoothly ground surfaces to minimize sliding friction. The strength and hardness of the steel, coupled with close dimensional tolerances in the mandrel, produce an unyielding mechanical loading system which maximizes diametral displacement accuracy and reproducibility. The highest accuracy in the diametral displacement of the expandable sleeve is achieved at small diametral displacements; typically $\leq$0.38 mm. For this reason, separate mandrels were made for testing irradiated H. B. Robinson (HBR) and Maine Yankee (MY) cladding, which have nominal inside diameter measurements of 9.32 and 9.85 mm, respectively. Four mandrels were made for each cladding type. Three of these were used with split ceramic cylinders, as described in a previous report;[40] the fourth mandrel was used with split metal rings, which were substituted for the more costly split ceramic cylinders in preliminary room-temperature calibration tests.

The present mandrel loading system was designed to produce a crack-type failure in irradiated LWR cladding at diametral strains of between 1 and 3% at the inside cladding surface for material with a rupture strength of ~830 MPa and a rupture ductility of $\leq$1% (measured as an increase in outside diameter) at 325°C. Therefore, failure of the irradiated cladding is expected to occur at diametral (sleeve) expansions of ~0.28 and 0.29 mm for the HBR and MY cladding, respectively. The taper angle will provide a linear ratio of ~16:1 between the axial displacement of the arbor and the diametral expansion of the sleeve. This choice of taper angle minimizes the sliding friction between the mandrel components (especially when treated with a high-temperature, low-vapor pressure, solid lubricant) and provides reasonable control of diametral expansion at the inside diameter of the cladding specimen. When used in conjunction with constant (Instron) crosshead displacement rates of 8.3×10^{-5} to 8.3×10^{-2} mm/s, the selected taper angle will produce cladding strain rates in the range $\sim 5 \times 10^{-7}$ to 6×10^{-4} s^{-1}. The magnitude of the diametral strain (elastic and plastic) at the inside surface of the cladding (δD_i) can be ascertained from the measured axial displacement (δL) of the arbor by invoking the assumption of an unyielding mandrel.

1. Mandrel Calibration

The eight mandrels were calibrated in the instrumented fixture shown in Fig. 44, using a constant crosshead displacement rate of 8.3×10^{-3} mm/s. Displacement transducers (LVDTs), which had been calibrated with precision gauge blocks, were used to monitor the axial displacement of the arbor and the resulting diametral expansion of the sleeve. The transducer (mV) outputs were plotted on an X-Y recorder (Hewlett Packard Model 7047A) using a 0.5-mV/cm scale range on both axes. The calibration procedure achieved a radial displacement resolution of ~2 μm.

The radial expansion was measured on a surface ligament at the middle of the sleeve as shown in Fig. 44. This is the location of the simulated pellet-pellet interface and, consequently, the region of maximum hoop stress at the inside cladding surface. The relationship between the expanding sleeve, the 1-mm-wide region containing the pellet-pellet interface (simulated by two split metal rings), and the cladding specimen is shown in Fig. 45, as viewed through a vertical slot in the specimen.

The calibration data for the individual mandrels were correlated with a linear-regression analysis for a polynomial of the type

$$\Delta D = m\Delta L + b \tag{8}$$

where ΔD is the diametral displacement of the sleeve (mm), ΔL is the axial displacement of the arbor (mm), and m and b are the slope and intercept, respectively. For displacements of interest in the mandrel experiments, the magnitude of b is negligible relative to mΔL (Table IX). Therefore, the sleeve expansion and, consequently, the expansion at the inside surface of the specimen (ΔD_i) can be calculated directly from the measured arbor displacement (ΔL) by the simple expression

$$\Delta D_i = m\ \Delta L, \tag{9}$$

where $1/m$ is the displacement ratio $\Delta L/\Delta D_i$. This calculated value of ΔD_i represents the total displacement (elastic plus plastic) at the inside surface of the test specimen. Furthermore, the relative stress states at the inside and outside surfaces of the test specimen can be inferred from a comparison of the values of ΔD_i with corresponding measured values of ΔD_o obtained by the method shown in Fig. 45.

Preliminary calibration data for the eight mandrels are given in Table IX. The linearity of the sleeve expansion as a function of the arbor displacement is indicated by the correlation coefficient r^2.

2. Mandrel Loading Tests

Five preliminary mandrel tests were conducted at 25°C on unirradiated Zircaloy specimens that were oxidized in steam at high temperature for different time periods to produce low-ductility material. The deformation tests were performed in an Instron (Model 1122) testing machine at a crosshead displacement rate of 8.3×10^{-3} mm/s. The purpose of these experiments was to evaluate and improve handling procedures that will be adopted for remote testing of irradiated cladding, and to determine the operating characteristics of the mandrel system. Parameters of interest include the accuracy and linearity of mandrel loading, optimum specimen length, reproducibility of mandrel test results, and the magnitude of the arbor force required to produce an axial through-wall crack in the high-strength, low-ductility material, which simulates the properties of irradiated cladding. The test results are shown in Figs. 46 and 47 and are listed in Table X.

Figure 46A shows an axial crack produced in high-ductility unirradiated Zircaloy cladding at a rupture strength of ~703 MPa at 25°C. In this first test, the original specimen length was 44.4 mm and the specimen was mechanically loaded with HBR mandrel 4 (see Table IX), using split-metal rings to simulate the high-stress region at the pellet-pellet interface. The 3.76-mm-long axial crack occurred in the region of the simulated pellet-pellet interface, approximately 120 degrees from the split in the metal rings which simulates an axial crack in the fuel. The failure strain obtained by measurement of the specimen outer diameter with the mandrel in place was 7.8%. This value is 25% smaller than the strain at the inner surface calculated by Eq. (9). Both values represent total (elastic and plastic) diametral strain. The plastic diametral strain at the outer surface, obtained by measurement after removal of the mandrel, was 6.1%. If the elastic modulus of Zircaloy[58] is taken as 1.0×10^5 MPa and the total diametral strain value of 7.8% is corrected for elastic strain, the resulting calculated plastic strain of 6.2% is in good agreement with the posttest value of 6.1% obtained after removal of the mandrel. The 1943-kg force on the arbor is excessively large, and is the result of the full-length contact between the expanding sleeve and the specimen due to the large specimen ductility. Removal of the mandrel was achieved by machining the cladding. The results of this test clearly indicate that the mandrel design is not particularly suited to the remote testing of high-ductility cladding, and that the optimum specimen length may be less than 44.4 mm.

Figures 46B and C show fine axial cracks produced by mandrel loading of oxidized, low-ductility Zircaloy cladding in tests 2 and 3. The specimen material was selected to simulate the high-strength (~827 MPa), low-ductility (<1%) characteristics of irradiated LWR cladding. Because the microstructure of this material is considerably more complicated than that of irradiated material, no inference is drawn from the crack length observed in the test specimen. These test specimens were loaded with MY mandrel 8 (see Table IX) using split-metal rings to simulate the pellet-pellet interface. An initial specimen length of ~19 mm was used in these tests to conserve material. Test results indicate that the two specimens failed at very low plastic strains (0.02 and 0.11%, respectively), as determined from unloaded measurement of the outside cladding diameter. The cracks in both specimens occurred at low mandrel loads (69.5 and 70.9 kg, respectively), and the calculated values for the total diametral strain at the inside and outside surface of both specimens were <1%. However, the failure in the specimen shown in Fig. 46B initiated at a location 90 degrees from the simulated pellet crack (split in metal rings), whereas the failure in the specimen shown in Fig. 46C initiated at the site of the simulated pellet crack.

Figures 47A and B show fine axial cracks after mandrel loading of another piece of oxidized Zircaloy cladding in tests 4 and 5. The oxygen content of this material was less than that of the cladding used in tests 2 and 3. Consequently, the rupture strength of this cladding was expected to be slightly less than that of material used in tests 2 and 3, and the ductility slightly higher. These specimens were loaded with MY mandrel 6 (see Table IX), using split-ceramic cylinders to simulate the pellet-pellet interface. The results in Table X indicate that the specimens shown in Figs. 47A and B failed at similar plastic strains (0.34 and 0.32%, respectively, from measurements of the outside cladding diameter), and similar mandrel loads (57.3 and 55.0 kg, respectively). The differences in the calculated total strain values at the inside and outside specimen surface are greater for these specimens than for the material with higher oxygen content in tests 2 and 3. The results obtained from tests 4 and 5 are consistent with the anticipated changes in material strength and ductility with oxygen content. Finally, the cracks in these specimens initiated at the simulated pellet crack and generally followed the cracks in the underlying ceramic cylinder. This is illustrated in Fig. 47B.

The results of the preliminary mandrel tests support the following conclusions:

a. The optimum specimen length will be between 19 and 44 mm.
b. The mandrel design is suitable for simulating PCI loading in irradiated cladding.
c. The assumption of an unyielding mandrel can be used to obtain reasonable (calculated) values for the strain states at the inside and outside surface of irradiated cladding.

d. The experimental procedure will yield reproducible deformation results.

3. Future Progress

Future progress will include the following steps in preparation for in-cell testing of irradiated cladding:

a. Check the reproducibility of calibration data for all eight mandrels.

b. Resolve the hoop stress into components in the axial, circumferential and 30° texture directions for archive HBR (7FD11) and MY cladding. This will be accomplished using strain-gage instrumented, mandrel-loaded specimens.

c. Check fixture alignment and establish optimum assembly procedures for in-cell testing.

Specimens of irradiated HBR cladding are being cut to length, cleaned to remove loose contamination, and dimensioned for the initial in-cell tests under mandrel loading conditions at 325°C.

Table IX. Preliminary Mandrel Calibration Data

Mandrel No.	Cladding Type	m (10^{-2})	b $(10^{-5}$ mm)	$r^{2(a)}$	$\frac{\Delta L}{\Delta D_i}$
1^b	HBR	5.979	0.446	0.9998	16.72
2^b	HBR	5.692	16.1	0.9982	17.57
3^b	HBR	5.716	25.4	0.9988	17.49
4^c	HBR	5.719	4.11	0.9994	17.48
5^b	MY	6.513	-31.9	0.9989	15.35
6^b	MY	6.407	91.6	0.9974	15.61
7^b	MY	6.695	50.2	0.9976	14.94
8^c	MY	5.892	-4.56	0.9993	16.97

[a] Correlation coefficient for a polynomial fit at an arbor displacement of 5.8 mm.

[b] Mandrels to be used with split-ceramic cylinders.

[c] Mandrels to be used with split-metal rings.

Table X. Preliminary Results of Room-Temperature Tests on Zircaloy-4 Cladding Using Mechanical Mandrel Loading (Mandrel Arbor Displacement Rate = 0.5 mm/min)

Test No.	Specimen Material	Calculated Diametral Failure Strain (%)		Measured Diametral Failure Strain[a] (%)	Max. Load (kg)	Remarks
		Inside Dia.	Outside Dia.	Outside Dia.		
1[b]	Unirrad.	9.8	7.8	6.1	1943	Axially oriented crack, ~3.76 mm long, initiated 120° from simulated pellet crack.
2[b]	Oxidized	0.89	0.94	0.02	69.5	Axially oriented crack, full length of specimen (19.1 mm), initiated 90° from simulated pellet crack.
3[b]	Oxidized	0.93	0.75	0.11	70.9	Axially oriented crack, full length of specimen (19.1 mm), initiated at simulated pellet crack.
4[c]	Oxidized	1.4	0.27	0.34	57.3	Axially oriented crack, ~15.8 mm long, initiated at simulated pellet crack.
5[c]	Oxidized	0.96	0.31	0.32	55.0	Axially oriented crack, full length of specimen (~19.1 mm), initiated at simulated pellet crack.

[a] After unloading the specimen.

[b] Mandrels used with split-metal rings.

[c] Mandrels used with split-ceramic cylinders.

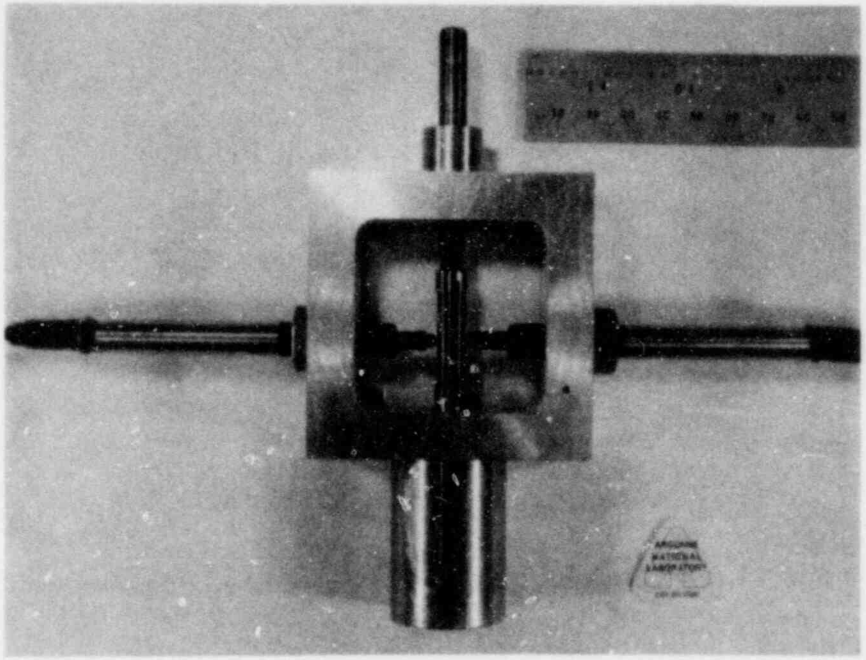

Fig. 44. Instrumented Fixture Used in the Calibration of Expanding Mandrels.

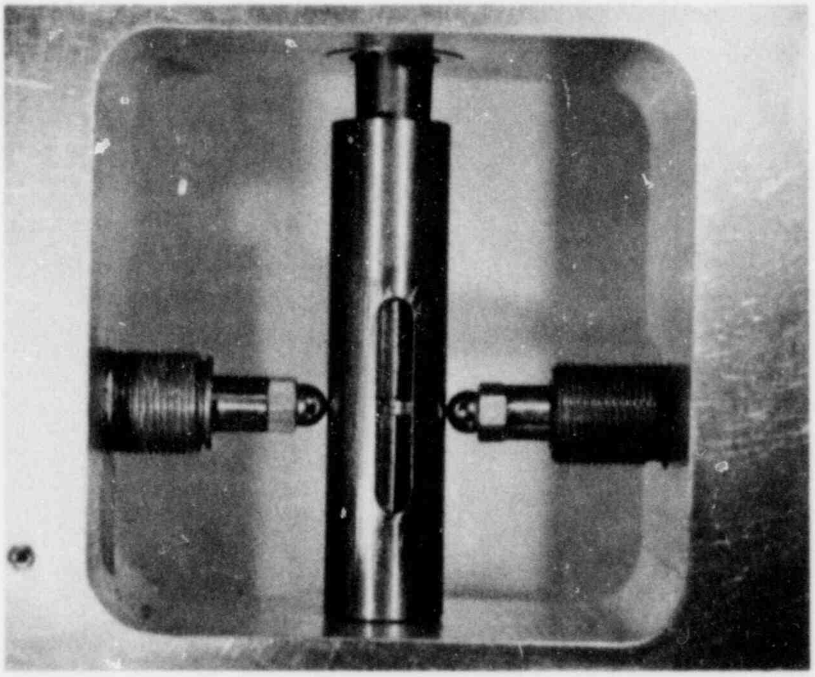

Fig. 45. Relationship Between the Cladding Specimen and the Components of the Expanding Mandrel.

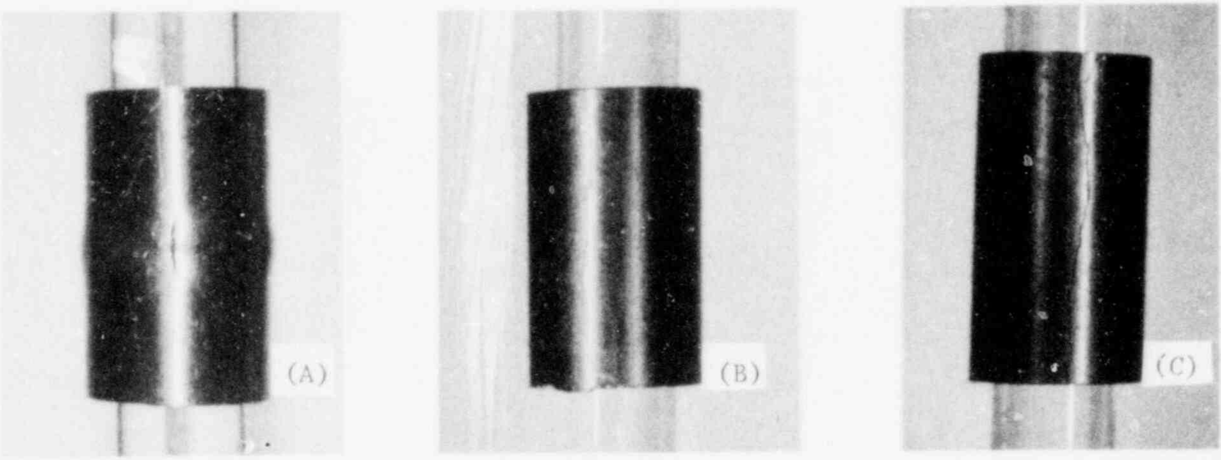

Fig. 46. Axial Cracks in (A) Stress-relieved High-Ductility and (B) and (C) Oxidized, Low-Ductility Zircaloy Cladding Specimens, after Mandrel Loading with an Internal Split-Metal Ring to Simulate the Pellet-Pellet Interface.

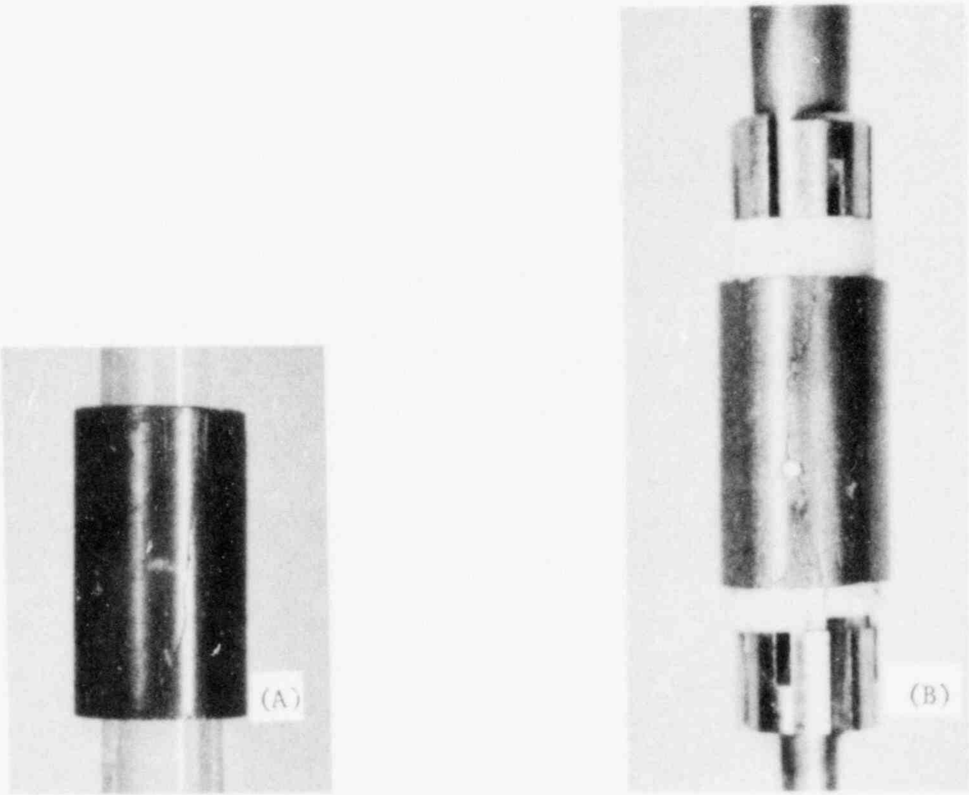

Fig. 47. Axial Cracks in Oxidized, Low-Ductility Zircaloy Cladding after Mandrel Loading with Split-Ceramic Cylinders to Simulate the Pellet-Pellet Interface. (A) Test 4; (B) Test 5.

REFERENCES

1. D. S. Kupperman and T. Claytor, in Light-Water-Reactor Safety Research Program: Quarterly Progress Report, July-September 1981, NUREG/CR-2437 Vol. III, ANL-81-77 Vol. III (February 1982).

2. J. V. Rattayya and M. C. Junger, Flow Excitation of Cylindrical Shells and Associated Coincidence Effects, J. Acoust. Soc. Am. 36, 878 (1964).

3. I. Mirsky and G. Herrmann, Non-axially Symmetric Motion of Cylindrical Shells, J. Acoust. Soc. Am. 29, 1116 (1957).

4. C. Stawström and M. Hillert, An Improved Depletion-Zone Theory of Intergranular Corrosion of 18-8 Stainless Steel, J. Iron Steel Inst. 207, 77 (1969).

5. M. J. Povich, Low Temperature Sensitization of Type 304 Stainless Steel, Corrosion 34, 60 (1978).

6. R. L. Fullman, "Predictability of Low Temperature Sensitization in Stainless Steels," in Proceedings: Seminar on Countermeasures for Pipe Cracking in BWRs, Electric Power Research Institute Report WS-79-174 (May 1980), Vol. 2, Paper No. 26.

7. R. L. Cowan II and C. S. Tedmon, Jr., Intergranular Corrosion of Iron-Nickel-Chromium Alloys, Advances in Corrosion Science and Technology 3, 297-400 (1973).

8. Standard Recommended Practices for Detecting Susceptibility to Intergranular Attack in Stainless Steels, ASTM Standard G815-1970, Designation: A262-70.

9. J. Y. Park, in Light-Water Reactor Safety Research Program: Quarterly Progress Report, April-June 1981, NUREG/CR-2437 Vol. II, ANL-81-77 Vol. II (November 1981).

10. D. T. Raske, H. Yamada, and W. J. Shack, in Light-Water-Reactor Safety Research Program: Quarterly Progress Report, April-June 1981, NUREG/CR-2437, Vol. II, ANL-81-77, Vol. II (November 1981).

11. Edward W. Hart and Harvey D. Solomon, Load Relaxation Studies of Polycrystalline High Purity Aluminum, Acta Met. 21, 295 (1973).

12. P. S. Maiya and W. J. Shack, in Ref. 1.

13. E. F. Rybicki et al., Effect of Weld Parameters on Residual Stresses in BWR Piping Systems, Final Report to Electric Power Research Institute, RP-1174, Battelle Columbus Laboratories (1980).

14. N. Fujita, M. Akiyama, and T. Tamura, Stress Corrosion Cracking of Sensitized Type 304 Stainless Steel in High Temperature Water Under Gamma Ray Irradiation, Corrosion 37(6), 335-341 (1981).

15. C. Tyzack, A Theory of Stress Corrosion, UKAEA Report ND-R-383(R) (August 1979).

16. F. A. Nichols and T. F. Kassner, in Refs. 1 and 9.

17. J. W. Oldfield and W. H. Sutton, Crevice Corrosion of Stainless Steels, I. A Mathematical Model and II. Experimental Studies, Br. Corros. J. 13(1), 13-22 (1978) and 13(3), 104-111 (1978), respectively.

18. D. F. Taylor and M. Silverman, Some Effects of Electrolyte Composition and Heat Treatment on the Aqueous Crevice Corrosion of Alloy 600 and Type 304 Stainless Steel at 288°C, Corrosion 36(9), 447-458 (1980).

19. A. D. Appelhans and J. A. Turnbull, Measured Release of Radioactive Xenon, Krypton, and Iodine from UO_2 at Typical Light Water Reactor Conditions, and Comparison with Release Models, NUREG/CR-2298 (1981).

20. J. Rest, The Prediction of Transient Fission-gas Release and Fuel Microcracking under Severe Core-Accident Conditions, Nucl. Technol. (in press).

21. J. Rest and C. E. Johnson, A Prediction of TMI-2 Core Temperatures from the Fission Product Release History, NSAC-12 (1980).

22. S. W. Tam and C. E. Johnson, to be published.

23. N. Oi and J. Takagi, Diffusion of Non-gaseous Fission Products in UO_2 Single Crystals, Z. Naturforsch. 19A, 1331-1332 (1964).

24. J. A. Turnbull and C. A. Friskney, The Release of Fission Products from Nuclear Fuel during Irradiation by Both Lattice and Grain Boundary Diffusion, J. Nucl. Mater. 58, 31-38 (1975).

25. G. Bandyopadhyay, Response of Oxide Fuel to Simulated Thermal Transients, Nucl. Technol. 41, 349-358 (December 1978).

26. O. D. Slagle, C. A. Hinman, and E. T. Weber, Experiments on Melting and Gas Release Behavior of Irradiated Fuel, HEDL-TME 74-17 (September 1974).

27. C. A. Hinman and O. D. Slagle, Behavior of Oxide Fuel During Thermal Transients, HEDL-TME 75-72 (March 1976), p. 85.

28. S. M. Gehl, The Release of Fission Gas During Transient Heating of LWR Fuel, ANL-80-108 (in press).

29. R. J. DiMelfi and L. W. Deitrich, The Effect of Grain-Boundary Fission Gas on Transient Fuel Behavior, Nucl. Technol. 43, 328-337 (1979), and ANL/RAS-78-32 (1978).

30. R. W. Baluffi and L. L. Seigle, Effect of Grain Boundaries on Pore Formation and Dimensional Changes During Diffusion, Acta. Met. 3, 170-177 (1955).

31. D. Hull and D. E. Rimmer, The Growth of Grain Boundary Voids Under Stress, Phil. Mag. 4, 673-687 (1959).

32. J. Weertman, Hull-Rimmer Grain-Boundary Void Growth Theory - A Correction, Scripta Met. 7, 1129 (1973).

33. M. V. Speight and J. E. Harris, The Kinetics of Stress-Induced Growth of Grain-Boundary Voids, Met. Sci. J. 1, 83 (1967).

34. T-J. Chuang and J. R. Rice, The Shape of Intergranular Creep Cracks Growing by Surface Diffusion, Acta. Met. 21, 1625 (1973).

35. T-J. Chuang, K. I. Kagawa, J. R. Rice, and L. B. Sills, Nonequilibrium Models for Diffusive Cavitation of Grain Interfaces, Acta. Met. 27, 265 (1979).

36. I-W. Chen and A. S. Argon, Diffusive Growth of Grain-Boundary Cavities, submitted to Acta. Met. in 1981.

37. W. Beere, Theoretical Treatment of Creep Cavity Growth with Application to Embrittlement by Inert Gas, Res Mechanica 2, 189 (1981).

38. J. Rest, The Prediction of Transient Fission-gas Release and Fuel Microcracking Under Severe Core-Accident Conditions, Nucl. Technol. 56 (3), 553 (March 1982).

39. J. Rest and S. Zawadzki, "Modeling of Fuel/Fission-Product Behavior," in Light-Water-Reactor Safety Research Program: Quarterly Progress Report, July-September 1980, NUREG/CR-1987, ANL-81-15 (February 1981).

40. F. L. Yaggee and H. M. Chung, "Biaxial Stress-Rupture Properties of Irradiated Zircaloy Fuel Cladding," "Characterization of Big Rock Point Reactor Fuel Cladding," and "Internal Mandrel Loading Experiments on Irradiated Zircaloy Fuel Cladding," in Ref. 1, pp. 51-69.

41. F. L. Yaggee, R. F. Mattas, and L. A. Neimark, Characterization of Irradiated Zircaloys: Susceptibility to Stress-Corrosion Cracking, Interim Report, EPRI NP-1155 (September 1979).

42. H. S. Rosenbaum, U. E. Wolff, and W. L. Bell, "Dresden-3 Fuel Rod Studies," in Determination and Microscopic Study of Incipient Defects in Irradiated Power Reactor Fuel Rods, EPRI NP-812 (July 1978), pp. 3-63 to 3-193 and pp. 4-13 to 4-19.

43. D. Lee and W. A. Backofen, Superplasticity in Some Titanium and Zirconium Alloys, Trans. AIME 239, 1034 (1967).

44. A. M. Garde, H. M. Chung, and T. F. Kassner, Uniaxial Tensile Properties of Zircaloy Containing Oxygen: Summary Report, ANL-77-30 (1977).

45. C. E. Coleman, D. Mills, and J. van der Kuur, Deformation Parameters of Neutron Irradiated Zircaloy-4 at 300°C, Can. Metall. Q. 11, 91 (1972).

46. D. O. Northwood, R. W. Gilbert, and C. E. Coleman, "Effect of Stress on Radiation Damage in Neutron Irradiated Zirconium Alloys," in Zirconium in the Nuclear Industry, Ed. A. L. Lowe, Jr. and G. W. Parry, ASTM STP 633, American Society for Testing and Materials (1977), pp. 418-436.

47. H. Kayano, Y. Higashiguchi, and S. Yajima, Yield Point Phenomenon in Neutron Irradiated Zirconium, J. Nucl. Sci. Technol. 15, 868 (1978).

48. C. D. Williams and R. W. Gilbert, "Fast-Neutron Damage in Zirconium-based Structural Alloys," in Radiation Damage in Reactor Materials, Proc. IAEA Symp., Vienna, 1, 235-247 (1977).

49. W. L. Bell, "Discussion on Operable Deformation Systems and Mechanical Behavior of Textured Zircaloy Tubing," in *Zirconium in Nuclear Applications*, ASTM STP 551, American Society for Testing and Materials (1974), pp. 199-200.

50. B. A. Cheadle, C. E. Ells, and J. van der Kuur, "Plastic Instability in Irradiated Zr-Sn and Zr-Nb Alloys," *ibid.*, pp. 370-384.

51. D. Lee and R. B. Adamson, "Modeling of Localized Deformation in Neutron Irradiated Zircaloy-2," in Ref. 46, pp. 385-401.

52. S. Aas, K. D. Olshausen, and K. Videm, "Fuel Failures Caused by Overpower Ramps," in Proc. Intl. Conf. on *Nuclear Fuel Performance*, October 15-19, 1973, London, England, pp. 55.1 to 55.6 and s4.1 to s4.5.

53. N. Fuhrman, V. Pasupatti, and L. V. Corsetti, "PCI Observation in a Combustion Engineering PWR," in Proc. ANS Topical Meeting on *Water Reactor Fuel Performance*, May 9-11, 1977, St. Charles, Illinois, pp. 262-272.

54. A. S. Bain, J. C. Wood, and C. E. Coleman, "Fuel Designs to Eliminate Defects on Power Increases," in Ref. 52, pp. 56.1 to 56.5.

55. J. H. Davies, H. S. Rosenbaum, J. S. Armijo, R. A. Proebstle, T. C. Rowland, J. R. Thompson, E. L. Esch, G. Romeo, and D. R. Rutkin, "Irradiation Tests to Characterize the PCI Failure Mechanism," in Ref. 53, pp. 230-242.

56. K. Videm and L. Lunde, "Stress-corrosion Cracking of Zircaloy Fuel Cladding Under Power Ramps and In-laboratory Test," *ibid.*, pp. 274-281.

57. K. O. Vilpponen, N. Førdestrømmen, K. Svanholm, and Y. Minagawa, "Fuel Performance Under Power Ramp Conditions in the HBWR," presented at IAEA Specialists' Meeting on *Pellet-Cladding Interaction in Water Reactors*, September 22-26, 1980, Risø, Denmark.

58. *MATPRO-Version 11 (Revision) - A Handbook of Materials Properties for Use in the Analysis of Light-Water Reactor Fuel Rod Behavior*, NUREG/CR-0497, TREE-1280, Rev. 2 (August 1981), p. 257.

Distribution for NUREG/CR-2437 Vol. IV (ANL-81-77 Vol. IV)

Internal:

R. P. Anderson
R. Avery
E. S. Beckjord
M. Blander
F. A. Cafasso
Y. S. Cha
H. M. Chung
T. N. Claytor
L. W. Deitrich
C. E. Dickerman
D. R. Diercks
B. R. T. Frost
S. M. Gehl
E. E. Gruber
M. Ishii
W. D. Jackson
T. F. Kassner (12)
A. B. Krisciunas
D. S. Kupperman
J. C. Leung
Y. Y. Liu
P. A. Lottes
P. S. Maiya
L. McUmber
K. Natesan
L. A. Neimark
F. A. Nichols
F. S. Onesto
R. G. Palm
J. Y. Park
D. R. Pepalis
M. Piasecka
R. B. Poeppel
J. J. Puro
S. R. Rajan
D. T. Raske
K. J. Reimann
J. Rest (30)
W. E. Ruther
W. J. Shack (3)
E. M. Stefanski (2)
R. P. Stein
C. E. Till
H. C. Tsai
R. A. Valentin
W. Wang
R. W. Weeks
F. L. Yaggee
R. S. Zeno
ANL Patent Dept.
ANL Contract File
ANL Libraries (3)
TIS Files (6)

External:

NRC, for distribution per R3 and R5 (420)
DOE-TIC (2)
Manager, Chicago Operations Office, DOE
R. Tom, DOE-CH
President, Argonne Universities Association
Materials Science Division Review Committee:
  G. S. Ansell, Rensselaer Polytechnic Inst.
  A. Arrott, Simon Fraser U.
  R. W. Balluffi, Massachusetts Inst. Technology
  A. L. Bement, TRW, Inc., Cleveland
  G. J. Fonken, U. Texas at Austin
  C. Laird, U. Pennsylvania
  M. E. Shank, Pratt & Whitney, East Hartford, Conn.
  P. G. Shewmon, Ohio State U.
  A. R. C. Westwood, Martin Marietta Labs.
R. B. Adamson, General Electric Co., Vallecitos Nuclear Center, P. O. Box 460, Pleasanton, Calif. 94566
W. Berry, Battelle-Columbus Labs., 505 King Ave., Columbus, O. 43201
J. Boulton, Whiteshell Nuclear Research Establishment, AECL, Pinawa, Manitoba, ROE 1L0, Canada
D. L. Burman, Westinghouse PWR Systems Div., P. O. Box 355, Pittsburgh, Pa. 15230
M. Charyulu, EG&G Idaho, Inc., P. O. Box 1625, Idaho Falls, Idaho 83401
R. A. Clark, Battelle Pacific Northwest Lab., P. O. Box 999, Richland, Wash. 99352
F. D. Coffman, Div. of Safety Technology, USNRC, Washington
W. J. Collins, Div. of Resident & Regional Reactor Inspection, USNRC, Washington
H. F. Conrad, Div. of Engineering, USNRC, Washington
R. Dalmas, Commissariat a l'Energie Atomique, Centre de 'Etudes Nucleaires de Grenoble, Ave. des Martyrs 38, Grenoble, France

J. C. Danko, Electric Power Research Inst., P. O. Box 10412, Palo Alto, Calif. 94304
J. Dearien, EG&G/INEL, 1520 Sawtelle Dr., Idaho Falls, Idaho 83401
B. J. Elliott, Div. of Engineering, USNRC, Washington
M. Fox, Electric Power Research Inst., P. O. Box 10412, Palo Alto, Calif. 94304
Y. S. Garud, S. Levy, Inc., 1901 S. Bascom Ave., Campbell, Calif. 95008
J. H. Gittus, Springfields Nuclear Power Development Labs., U. K. Atomic Energy Authority, Springfields, Salwick, Preston, PR4 ORR, England
D. O. Harris, S.A.I., 99 Almaden Blvd., San Francisco, Calif. 95113
W. S. Hazelton, Div. of Engineering, USNRC, Washington
R. R. Hobbins, EG&G/INEL, 1520 Sawtelle Dr., Idaho Falls, Idaho 83401
T. M. Howe, EG&G/INEL, 1520 Sawtelle Dr., Idaho Falls, Idaho 83401
R. E. Johnson, Generic Issues Branch, USNRC, Washington
W. V. Johnston, Div. of Engineering, USNRC, Washington
R. L. Jones, Electric Power Research Inst., P. O. Box 10412, Palo Alto, Calif. 94304
K. R. Jordan, Nuclear Fuel Div., Monroeville Nuclear Center, Westinghouse Electric Corp., Monroeville, Pa. 15146
D. D. Lanning, Battelle Pacific Northwest Lab., P. O. Box 999, Richland, Wash. 99352
P. MacDonald, EG&G/INEL, 1520 Sawtelle Dr., Idaho Falls, Idaho 83401
G. P. Marino, Div. of Accident Technology, USNRC, Washington
S. McDonald, Westinghouse Electric Corp. R&D Center, Beulah Rd., Pittsburgh, Pa. 15235
K. R. Merckx, Exxon Nuclear, Inc., 2955 George Washington Way, Richland, Wash. 99352
R. B. Mulgrew, Div. of Document Control, USNRC, Washington (3)
J. Muscara, Div. of Engineering Technology, USNRC, Washington
D. M. Norris, Electric Power Research Inst., P. O. Box 10412, Palo Alto, Calif. 94304
D. R. O'Boyle, Commonwealth Edison Co., P. O. Box 767, Chicago, Ill. 60690
H. Ocken, Electric Power Research Inst., P. O. Box 10412, Palo Alto, Calif. 94304
R. N. Oehlberg, Electric Power Research Inst., P. O. Box 10412, Palo Alto, Calif. 94304
T. P. Papazoglou, Lynchburg Research Center, Babcock & Wilcox Co., P. O. Box 1260, Lynchburg, Va. 24505
D. A. Powers, Div. of Systems Integration, USNRC, Washington
W. J. Quapp, EG&G/INEL, 1520 Sawtelle Dr., Idaho Falls, Idaho 83401
J. T. A. Roberts, Electric Power Research Inst., P. O. Box 10412, Palo Alto, Calif. 94304
C. Ronchi, Euratom - T. V., Postfach 2266, 75 Karlsruhe, West Germany
R. A. Sallach, Sandia National Labs., Albuquerque, N. Mex. 87185
H. H. Scott, Div. of Accident Technology, USNRC, Washington
C. Z. Serpan, Div. of Engineering Technology, USNRC, Washington
R. R. Sherry, Div. of Accident Technology, USNRC, Washington
M. Silberberg, Div. of Accident Technology, USNRC, Washington
R. D. Silver, Div. of Safety Technology, USNRC, Washington
P. Smerd, Combustion Engineering, Inc., P. O. Box 500, Windsor, Conn. 06095
V. W. Storhok, Battelle Columbus Labs., 505 King Ave., Columbus, O. 43201
R. Van Houten, Div. of Accident Technology, USNRC, Washington
R. A. Watson, Carolina Power and Light Co., P. O. Box 1551, Raleigh, N. C. 27602
J. Weeks, Brookhaven National Lab., Upton, N. Y. 11973
K. R. Wichman, Div. of Licensing, USNRC, Washington

120555078877 1 R3R5
US NRC
ADM DIV OF TIDC
POLICY & PUBLICATIONS MGT BR
PDR NUREG COPY
LA 212
WASHINGTON DC 20555